Discrete Roughness Effects on High–Speed Boundary Layers

A DISSERTATION
SUBMITTED TO THE FACULTY OF THE GRADUATE SCHOOL
OF THE UNIVERSITY OF MINNESOTA
BY

Prahladh Satyanarayanan Iyer

IN PARTIAL FULFILLMENT OF THE REQUIREMENTS
FOR THE DEGREE OF
DOCTOR OF PHILOSOPHY

Krishnan Mahesh, Adviser

January, 2015

Acknowledgements

I am grateful for having had the opportunity to work with Prof. Krishnan Mahesh as my adviser. His constant support, motivation and encouragement was instrumental in making my doctoral studies exciting and pleasurable. His in-depth knowledge, physical insight, eagerness to discuss research progress and not to mention, good sense of humor always led to fruitful and interesting interactions. I would like to thank Prof. Mahesh for his advise and suggestions on professional and other matters, and for giving me the opportunity to work on a range of topics during my doctoral studies.

I am thankful to my committee members, Prof. Ellen Longmire, Prof. Thomas Schwartzentruber, Prof. Pagos Stinis and Prof. Bernardo Cockburn for their comments and suggestions.

I am grateful to Dr. Suman Muppidi for mentoring me during my early years in the group and getting me set up with MPCUGLES and transition literature. I'm also thankful to Mr. Aswin Gnanaskandan and Dr. Aman Verma for clearing innumerable technical doubts of mine. I have benefited greatly from discussions with various members of Prof. Mahesh's group, some of whom include, Dr. Xiaochaun Chai, Mr. Zane Nitzkorski, Mr. Rajapandiyan Asaithambi, Dr. Michael Mattson, Ms. Erin Mussoni, Mr. Praveen Kumar, Dr. Hyunchul Jang, Mr. Karim Alame and Mr. Marc Regan. Social interactions with the group during APS conferences and otherwise were always memorable.

I am deeply indebted to my parents Dr. A. Satya Narayanan and Mrs. G. R. Sukanya for their constant encouragement and support without which this dissertation would not be possible. I would like to thank all my friends at UMN for making my stay memorable - Ranga, Aswin, Savio, Coma, Thavil, Raja, Janani, Vivek, Rishab, Maddy, Fufa, Baba, Venkat, Rohini and Howitzers cricket club among others. Lunch and coffee

sessions with Savio, Ranga, Aswin and Raja were most memorable and fun.I am also grateful to my fiancee, Sushmita for her support during the final stages of my studies. I thank Menet and MSI staff for their technical support at various stages.

Lastly, I would like to thank Dr. Danehy and his group for providing experimental data used in this dissertation and acknowledge financial support from NASA under the Hypersonics NRA program Grant No. NNX08AB33A. Computer time provided by the Minnesota Supercomputing Institute (MSI) and the Texas Advanced Computing Center (TACC) through TeraGrid Allocations is gratefully acknowledged.

To my parents

Abstract

This dissertation studies the effects of a discrete roughness element on a high–speed boundary layer using Direct Numerical Simulations (DNS) on unstructured grids. Flow past a cylindrical roughness element placed perpendicular to the flow and a hemispherical bump is studied. A compressible linear stability theory (LST) solver for parallel flows is developed based on the algorithm by Malik[33] and validated for a range of Mach numbers ranging from incompressible to Mach 10. The evolution of the perturbations from DNS is validated with the linear stability solver making the DNS algorithm suitable to study transition problems.

Flow past a cylindrical roughness element at Mach 8.12 is simulated using DNS and the velocity profiles in the symmetry and wall–parallel planes are compared to the experiments of Bathel *et al.*[7]. The flow remains steady and laminar, and does not transition. Overall, good agreement is observed between DNS and experiments, thus validating our algorithm to study effect of roughness on high–speed flows. However, differences are observed in the separation region upstream and recirculation region downstream of the roughness. The DNS results are used to quantify possible uncertainties in the measurement technique as suggested by Danehy[20]. The effect of upstream injection (5% of the free–stream velocity) is also simulated to quantify its effects on the velocity profiles to mimic the injection of NO into air in the experiment.

Flow past a hemispherical bump at Mach 3.37, 5.26 and 8.23 are simulated using DNS with the flow conditions matching the experiments of Danehy *et al.*[19] to understand the different flow features associated with the flow and the physical mechanism that causes the flow to transition to turbulence. It is observed that the Mach 3.37 and 5.26 flows transition to turbulence while the Mach 8.23 flow remains laminar downstream of the roughness element. The roughness element used in this study is large

since the boundary layer thickness of the laminar boundary layer at the location of the roughness is smaller than the roughness height The Mach 3.37 flow undergoes transition closer to the bump when compared to Mach 5.26, in agreement with experimental observations. Transition is accompanied by an increase in C_f and C_h (Stanton number). Even for the case that did not undergo transition (Mach 8.23), streamwise vortices induced by the roughness cause a significant rise in C_f until 20D downstream. Mean Van-Driest transformed velocity and Reynolds stress for Mach 3.37 and 5.26 shows good agreement with available data. The transition process involves the following key elements - Upon interaction with the roughness element, the boundary layer separates to form a series of spanwise vortices upstream of the roughness, and a separation shear layer. The system of spanwise vortices wrap around the roughness element in the form of horseshoe/necklace vortices to yield a system of counter-rotating streamwise vortices downstream of the element. These vortices are located beneath the separation shear layer and perturb it, which results in the formation of trains of hairpin-shaped vortices further downstream of the roughness for the cases that undergo transition. These hairpins spread in the span with increasing downstream distance and the flow increasingly resembles a fully developed turbulent boundary layer. A local Reynolds number based on the wall properties is seen to correlate the onset of transition for the cases considered.

To assess the effect of roughness height on transition, a Mach 3.37 flow past a hemispherical bump is studied by varying the boundary layer thickness ($k/\delta = 2.54$, 1.0, 0.25 & 0.125) where k is the roughness height and δ is the laminar boundary layer thickness at the location of the roughness. Transition occurs in all cases, and the essential mechanism of transition appears to be similar. At smaller boundary layer thickness, multiple trains of hairpin vortices are observed immediately downstream of the roughness, while a single train of hairpin vortices is observed at larger δ. This behavior is explained by the influence of the boundary layer thickness on the separation vortices upstream of the roughness element. Also, hairpin vortices that form downstream of the roughness initially scale with the height of the roughness element and further downstream, begin to scale with the boundary layer thickness, thus causing the entire boundary layer to transition. Dynamic Mode Decomposition of the pressure field for $k/\delta = 1$ and 0.125 is used to obtain the frequency of shedding of hairpin vortices.

Contents

List of Tables

List of Figures

Chapter 1

Introduction

1.1 Motivation

The transition of boundary layers from laminar to turbulent flow has been an active field of research for several decades. Transition can occur due to several factors; e.g. free–stream disturbances, adverse pressure gradients and surface roughness. Understanding the physical mechanism of transition is essential to design control techniques to delay transition. For high-speed flows, transition is accompanied by an undesirable increase in skin-friction coefficient and heating rates. Transition is therefore an important consideration for applications such as thermal protection systems for the Space Shuttle which need to be designed for appropriate heat loads. Vehicles that spend a long period of time at hypersonic speeds can be critically affected by uncertainties in the transition prediction, depending on their Reynolds numbers (Schneider [57]). At higher Mach numbers, transition can cause the heating rates to increase four to five fold when compared to a laminar flow.

It is well-known in literature that roughness causes transition to turbulence (Dryden [22], Klebanoff, Cleveland & Tidstrom [30], among others). However, the physical mechanism involved in transition has not been fully understood till date, especially for high-speed flows (Schneider [57], Reshotko [49]). Roughness elements have been classified as discrete or distributed depending on their physical geometry. Discrete roughness occurs in the form of steps, joints, rivets and local machining flaws in practical applications. An example of a discrete roughness is shown in Figure 1.1(a) where protruding

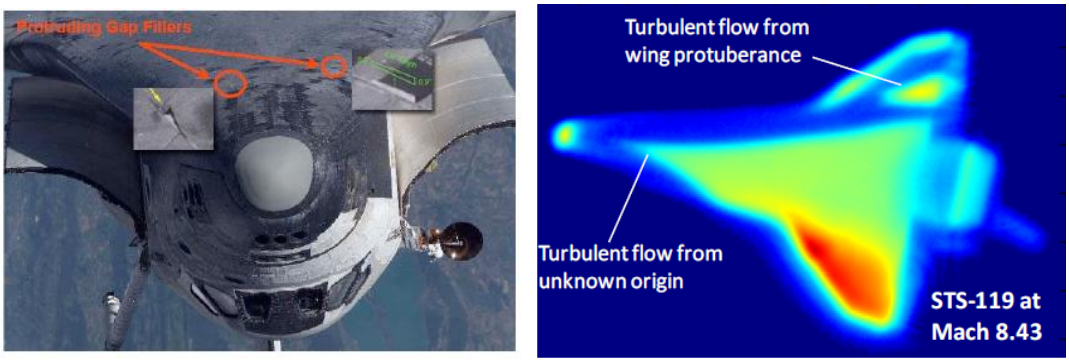

Figure 1.1: Figure showing the protruding gap filler material acting as a discrete roughness element in the Discovery mission from Berry *et al.* [4] (left) and increased heating produced by wing protuberance in the STS-119 mission from Gibson *et al.* [26] (right).

gap filler material acts as a discrete roughness element and can potentially transition the boundary layer that grows over the surface of the shuttle to turbulence under suitable conditions. In Figure 1.1(b), a protuberance was attached to the wing in the STS-119 to study its effect on heating. It was observed that the region around the protuberance had higher heat fluxes indicating its effects (Gibson *et al.* [26]). A spacewalk had to be carried out in the STS-114 mission to remove a piece of material to prevent any transition (Berry *et al.* [4]).

Linear Stability Theory (LST) has been widely used to study transition in compressible boundary layers e.g. Mack [32], Lees & Lin [31], Malik [33]. Typically, a locally parallel assumption is made wherein the mean flow varies in the wall-normal direction only and an integrated e-N method is used to predict the onset of transition. While two-dimensional Tollmein-Schlichting (TS) waves are the most unstable mode at low speeds, oblique and inviscid Mack modes tend to be the most unstable modes at high-speeds depending on M_∞ and wall conditions. Under many circumstances, the linear eigenmode growth is 'bypassed'. [47] lists the various paths to transition to turbulence depending on the amplitude of the disturbance as shown in Figure 1.2 as described by Morkovin [38]. For low amplitude disturbances, linear eigenmode growth takes place, followed by secondary instability, mode interactions and non-linear breakdown. Even when the flow is asymptotically stable to small disturbances, algebraic growth could take place, termed as transient growth [49]. For low amplitude disturbances, Linear

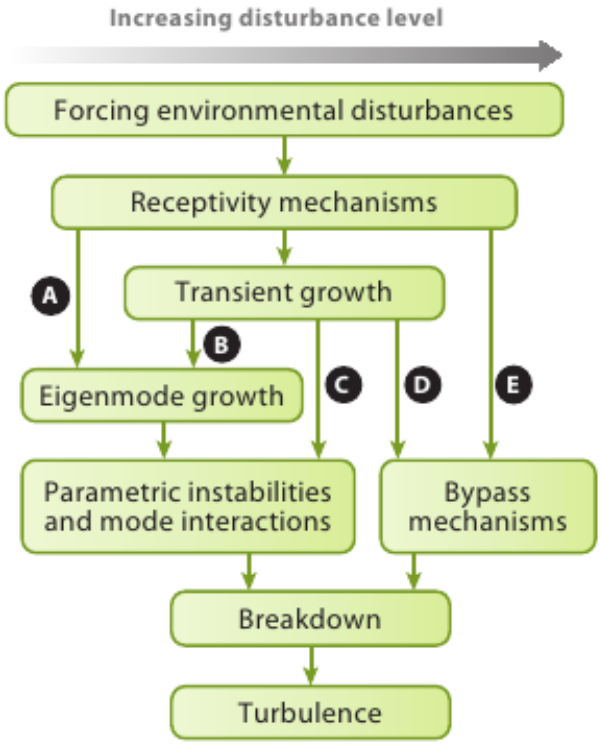

Figure 1.2: Figure showing the various paths to transition to turbulence as suggested by Morkovin [38]. Figure taken from Zhong & Wang [70].

Stability Theory can predict linear eigenmode and algebraic growth. However, for large disturbance levels, non-linear breakdown takes place which cannot be described by the linearized disturbance equations. For high Mach number flows, the noise in the wind tunnel is also an important factor to consider while predicting transition. Noisy wind tunnels cause the flows to transition earlier as compared to quiet tunnels (Schneider [57]).

1.2 Review of past work : Low–speed transition

Transition induced by an isolated roughness element at low-speeds has been studied by Tani *et al.* [61], Klebanoff, Cleveland & Tidstrom [30] and Acarlar & Smith [1] among

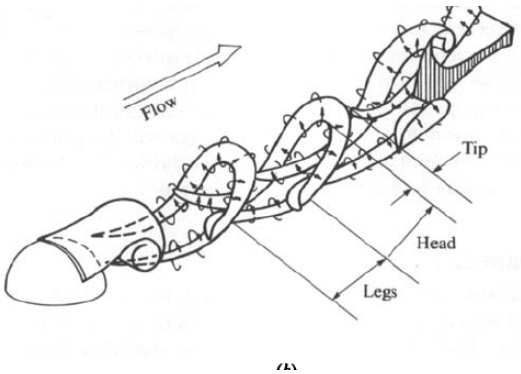

Figure 1.3: Figure showing hairpin shaped vortices shed downstream of a single hemispherical bump at low speeds from Acarlar & Smith [1].

others. Acarlar & Smith [1] observe that a necklace shaped vortex forms upstream of the hemispherical roughness and hairpin shaped vortices are shed downstream of it. Figure 1.3 shows hairpin vortices shed by a single hemisphere placed in a laminar boundary layer flow. They suggest that the concentration of vorticity into the low pressure recirculation region behind the roughness occurs in a manner so as to produce hairpin shaped vortices. Tani *et al.* [61] studied the effect of Re_k (Reynolds number based on free–stream properties and roughness height) and showed that increasing Re_k beyond a critical value moves the transition location closer to the roughness. They suggest that the deformation of the velocity field due to the streamwise vortices (observed even at sub-critical Re_k) shed on the sides of the hemisphere is likely to account for the critical behavior of transition. Tumin & Reshotko [64] studied the receptivity of a boundary layer past a three-dimensional hump and found that counter-rotating streamwise vortices were produced downstream of the roughness. Ergin & White [25] experimentally studied the flow past an array of cylinders placed on a flat plate. They note that the transition process is a result of a competition between the unsteady disturbance growth and the rapid relaxation of the steady flow that tends to stabilize disturbances. Mason & Morton [36] experimentally studied the flow behind wall-mounted obstacles and found that counter-rotating streamwise vortices were formed at the center plane. Depending on the shape of the obstacle, the vortices had an upwash or downwash.

While incompressible transition is sensitive to Reynolds number and the shape and height of the roughness element, transition at high speeds also depends on Mach number,

free-stream temperature and the thermal boundary condition at the wall. Also, the influence of shock waves produced by the roughness on transition location is unclear. Schneider [57] provides a review of the effects of roughness on the transition of hypersonic boundary layers. Some of the suggested mechanisms for hypersonic boundary layer transition include the concave-wall Gortler instability Saric [53], the first- and second–mode streamwise-instability Mack [32], the 3-D crossflow instability Saric, Reed & White [54], and transient growth Reshotko & Tumin [49].

1.3 Review of past work: high–speed transition

The availability of greater computational resources and parallel-computing have enabled the use of Direct Numerical Simulations (DNS) to study transition. A recent review by Zhong & Wang [70] discusses the progress made in the DNS of instability and transition in hypersonic boundary layers. Choudhari *et al.* [12] numerically studied transition induced by large roughness elements using the space-time conservation element, solution element (CESE) methodology. They simulated flow around rectangular and cylindrical elements in boundary layers at Mach numbers of 4.1 and 6.5 and concluded that for these Mach numbers, no self-sustaining vortex generation process was present. They also performed a two–dimensional parametric study and found that at subcritical Reynolds numbers of the boundary layer, absolute instability resulting in vortex shedding downstream was likely to weaken at supersonic free-stream conditions. They therefore conjectured that convective instability might be the dominant instability mechanism for supersonic boundary layers. They also noted the presence of 'mushroom shaped' streamwise velocity contours in the wake which give rise to inflexion points in the flow downstream.

Redford, Sandham & Roberts [46] studied the flow past a smooth shaped roughness element at Mach 3 and 6 with acoustic forcing at the free-stream to ensure transition. They proposed a correlation for predicting transition induced by a three dimensional roughness element at high-speeds for roughness heights smaller than the boundary layer thickness. Subbareddy, Bartkowicz & Candler [5] studied the effect of a cylindrical protuberance on a Mach 6 laminar boundary layer using DNS. They observed that the vortex system formed upstream of the cylinder resembles the set of vortices seen in

incompressible flow by Baker [3] and concluded that for thinner boundary layers, the shock created by the roughness produces a jet of high momentum fluid that recirculates into the vortex system which could cause unsteadiness.

Marxen, Iaccarino & Shaqfeh [34] studied Mach 4.8 flow past a two–dimensional roughness using a body fitted grid and immersed boundary technique. They found that the roughness considerably alters the stability characteristics of the flow, although far downstream the stability characteristics resemble that of a flat plate boundary layer. Groskopf, Kloker & Marxen [27] performed a bi-global stability analysis of the region downstream of a 3D pizza box shaped roughness and noted a pronounced convective instability due to a pair of counter-rotating streamwise vortices. Choudhari *et al.*[15] studied the bi-global stability characteristics behind a diamond shaped roughness and a pair of roughness elements at Mach 3.5. They study the even (symmetric/varicose) and odd (antisymmetric/sinuous) modes of instability produced by the roughness. They note that the fluctuations associated with either modes are concentrated over a narrow spanwise extent of the streaks, which is significantly smaller in comparison to the spanwise wavelength of the dominant first mode instability of the dominant first mode instability of the unperturbed boundary layer flow.

Empirical correlations based on Re_θ/M_e (Reshotko [48]) and Re_{kk} (Reda [45]), Reynolds number based on properties at the height of the roughness are used to predict the onset of transition, with varying amounts of success. Figure 1.4 shows the scatter in the data for a correlation proposed by Reda [45]. It is important to understand the physics behind transition induced by the discrete roughness element to propose a transition prediction criterion.

1.4 Overview

Direct Numerical Simulation (DNS) of the compressible Navier–Stokes equations using a finite volume method is used in this dissertation. A novel algorithm developed by Park & Mahesh [43] to simulate compressible flows on unstructured grids is employed. It employs a modified least–squares approach to reconstruct the fluxes at cell faces (that makes the convective flux computation more accurate), and a scheme to split the viscous stress tensor into the compressible and the incompressible parts (that makes the

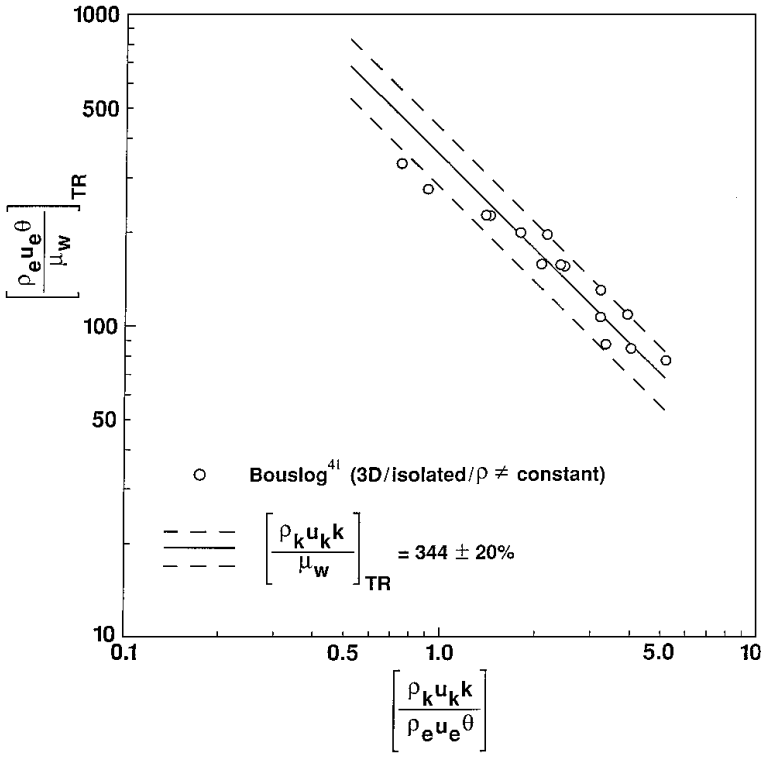

Figure 1.4: Figure showing correlations used to predict transition induced by a discrete roughness element at high–speeds from Reda [45]. Note the scatter in the data.

viscous flux computation accurate). It is known that upwind schemes add numerical dissipation which can affect the eddies formed in the transitional/ turbulent boundary layer (Moin & Mahesh [37]) and hence its important to localize numerical dissipation where required. The algorithm used in this dissertation uses a novel characteristic filter based shock capturing scheme that localizes numerical dissipation to regions of shocks.

This dissertation studies the effect of a discrete roughness on a high–speed boundary layer. All the flow conditions studied are chosen based on experiments performed at the NASA Langeley Mach 10 wind tunnel by Danehy *et al.* [19] and Bathel *et al.* [7]. Firstly, flow past a cylindrical roughness element at Mach 8.12 is studied which match the experiments of Bathel *et al.* [7]. Velocity profiles extracted at the symmetry and wall-normal planes are compared to experiment and good agreement is observed overall, thus validating our algorithm. Effect of upstream injection and quantification of uncertainties associated with the experimental technique are also studied. Next,

flow past a hemispherical bump at free–stream Mach numbers of 3.37, 5.26 and 8.23 are studied whose flow conditions match the experiments of Danehy *et al.* [19]. The roughness elements are 'large' since their height is larger than the laminar boundary layer thickness at its location for all the three Mach numbers. It was seen that while the Mach 3.37 and Mach 5.26 flows undergo transition downstream of the roughness, the Mach 8.23 flow remains laminar. Also, the Mach 3.37 flow undergoes transition closer to the roughness. The qualitative trend of transition is consistent with the observations in the experiment. Qualitative comparisons made with experiment show good agreement. The physical mechanism involved in transition is studied detailing the different flow features that contribute to transition. A Reynolds number based on the wall properties is seen to correlate well with the trend of transition. Lastly, the effect of boundary layer thickness for the Mach 3.37 flow is studied where the boundary layer thickness (δ) is varied such that $\delta/k = 0.4$, 1, 4 and 8 where k is the height of the roughness. For the larger δ flows, it was seen that a single train of hairpin vortices were formed downstream of the roughness as opposed to multiple trains for the lower δ flows. It was also observed that the hairpin vortices initially scaled with the roughness height, but with increasing downstream distance, scaled with the boundary layer thickness.

The principal contributions of this work is as follows:

- Propose a physical mechanism for transition induced by a large roughness element. The roughness element causes the boundary layer to separate upstream giving rise to a system of vortices whose number depends on the flow conditions. These upstream vortices wrap around the roughness elements and form a system of streamwise vortices downstream of the roughness. Counter-rotating streamwise vortex pairs are observed close to the symmetry plane (SP vortices) and off-symmetry plane (OSP) vortices. Counter-rotating vortices with a net upwash become stronger downstream and cause the flow to transition while those with a net downwash are likely to weaken with downstream distance and stabilize the flow.

- Study the effect of boundary layer thickness on discrete roughness induced transition with all other parameters kept constant. For smaller boundary layer thicknesses, multiple trains of hairpin vortices were observed downstream whereas a

single train of hairpin vortices were observed for larger boundary layer thicknesses. It was seen that the hairpin vortices initially scaled with the roughness height, but with increasing downstream distance, scaled with the boundary layer thickness.

- Quantify possible sources of uncertainty in a novel NO-based Molecular Tagging Velocimetry (MTV) technique developed by Dr. Danehy's group at NASA Langeley to measure velocity profiles in hypersonic flows. The effects of upstream injection and uncertainty in laser position are reported in this work.

- Implementation of a Linear Stability Theory (LST) solver to study compressible parallel flow instabilities. This code was used to validate the DNS solver and to demonstrate its suitability for high–speed transition simulations.

- Implementation of a Dynamic Mode Decomposition (DMD) solver to extract dominant spatial features of a flow based on the frequency. The code was validated for the flow past a two dimensional cylinder at low Reynolds numbers and was tested on low and high speed jets in crossflow to demonstrate its applicability for complex flows.

This dissertation is organized as follows:

- Chapter 2 describes the numerical algorithm used for the Direct Numerical Simulation (DNS). It also describes the numerical algorithm used in the Linear Stability Theory (LST) solver and presents validation of the DNS with LST to demonstrate the applicability of our DNS solver to study transition.

- Chapter 3 reports the effect of a cylindrical roughness element on a Mach 8.12 laminar boundary layer. Quantitative comparisons are made with the experiments of Bathel *et al.* [7] to validate our setup and also report the effect of possible uncertainties associated with the experimental technique used.

- Chapter 4 reports the effect of a hemispherical bump on a Mach 3.37, 5.26 and 8.23 boundary layer. The physical mechanism, detailed flow features, temporal spectra and turbulence characteristics of the flow downstream is discussed.

- Chapter 5 reports the effect of boundary layer thickness on the transition induced by a hemispherical bump on a Mach 3.37 laminar boundary layer with all other parameters kept constant.
- Chapter 6 summarizes the findings of this dissertation.
- Appendix A describes the algorithm used for Dynamic Mode Decomposition (DMD). The method was validated for a low Reynolds flow past a cylinder and tested on low and high speed jets in crossflow. 1

Chapter 2

Numerical Details

2.1 Direct Numerical Simulation (DNS) algorithm

The simulations use an algorithm developed by Park & Mahesh [43] for solving the compressible Navier-Stokes equations on unstructured grids. The compressible Navier-Stokes equations in conservative form are as follows:

$$\frac{\partial \rho}{\partial t} = -\frac{\partial}{\partial x_k}\left(\rho u_k\right) \tag{2.1}$$

$$\frac{\partial \rho u_i}{\partial t} = -\frac{\partial}{\partial x_k}\left(\rho u_i u_k + p\delta_{ik} - \sigma_{ik}\right) \tag{2.2}$$

$$\frac{\partial E_T}{\partial t} = -\frac{\partial}{\partial x_k}\left\{\left(E_T + p\right) u_k - \sigma_{ik} u_i - Q_k\right\} \tag{2.3}$$

where ρ, u_i, p and E_T are density, velocity, pressure and total energy, respectively. The viscous stress σ_{ij} and heat flux Q_i are given by

$$\sigma_{ij} = \frac{\mu}{Re}\left(\frac{\partial u_i}{\partial x_j} + \frac{\partial u_j}{\partial x_i} - \frac{2}{3}\frac{\partial u_k}{\partial x_k}\delta_{ij}\right) \tag{2.4}$$

$$Q_i = \frac{\mu}{(\gamma - 1)M_\infty^2 RePr}\frac{\partial T}{\partial x_i} \tag{2.5}$$

where Re, M_∞ and Pr denote the Reynolds number, Mach number and Prandtl number respectively.

2.1.1 Finite Volume Formulation

The governing equations are discretized using a cell–centered finite volume scheme, a schematic of which is shown in Figure 2.1 (a). Upon integration over the control volume, application of the Gauss theorem and some rearrangement, the governing equations may be written as

$$\frac{\partial \rho_{\text{cv}}}{\partial t} = -\frac{1}{V_{\text{cv}}} \sum_{\text{faces}} \rho_f v_N A_f \tag{2.6}$$

$$\frac{\partial \left(\rho u_i\right)_{\text{cv}}}{\partial t} = -\frac{1}{V_{\text{cv}}} \sum_{\text{faces}} \left[\left(\rho u_i\right)_f v_N + p_f n_i - \sigma_{ik,f} n_k \right] A_f \tag{2.7}$$

$$\frac{\partial \left(E_T\right)_{\text{cv}}}{\partial t} = -\frac{1}{V_{\text{cv}}} \sum_{\text{faces}} \left[\left(E_T + p\right)_f v_N - \sigma_{ik,f} u_{i,f} n_k - Q_{k,f} n_k \right] A_f \tag{2.8}$$

where V_{cv} is the volume of CV, A_f is the area of the face, n_i is the outward normal vector at surface, and v_N is the face-normal velocity.

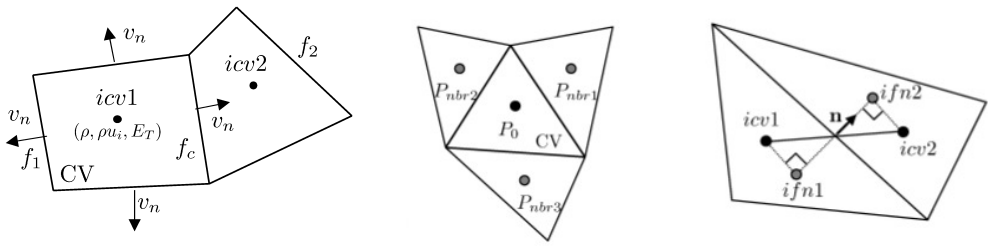

(a) (b) (c)

Figure 2.1: Schematic of the finite volume scheme used with (a) depicting the collocated cell-centered scheme used, (b) depicting the cell center P_0 and its neighboring points used for least-square reconstruction and (c) depicting the projection of the cv center onto the face normal for computing derivatives at the face for viscous terms.

$\mathbf{q}_{\text{cv}} = \left(\int_{\text{cv}} \mathbf{q} dV\right) / V_{\text{cv}}$ is the volume average within the cell, where $\mathbf{q} = (\rho, \rho u_i, E_T)$ are the conservative variables. Here, the subscript f denotes interpolation at each face of the control volume. For any scalar ϕ, the value at the face is computed as follows,

$$\phi_{f_c} = \frac{\phi_{icv1} + \phi_{icv2}}{2} + \frac{1}{2} \left(\nabla\phi|_{icv1} \cdot \Delta\mathbf{x}^{icv1} + \nabla\phi|_{icv2} \cdot \Delta\mathbf{x}^{icv2} \right), \tag{2.9}$$

where $\Delta\mathbf{x}^{icv1} = \mathbf{x}_{f_c} - \mathbf{x}_{icv1}$, and $\nabla\phi|_{icv1}$denotes the gradient defined at $icv1$. The gradient is computed using the 'Least square method' (LSQ) for viscous terms and the 'Modified-least squares method' (MLSQ) for the convective terms.

2.1.2 Second order reconstruction scheme

In the least square method, $\nabla\phi|_{\text{cv}}$ is computed using the Taylor series expansion given by:

$$\phi(\mathbf{x}) \approx \phi(\mathbf{x}_0) + \nabla\phi|_{\text{cv}} \cdot (\mathbf{x} - \mathbf{x}_0), \tag{2.10}$$

where $\mathbf{x}_0$ denotes coordinates of CV cell center, P_0 in Figure 2.1 (b), and $\mathbf{x}$ is any point that belongs to neighboring cells . Let $\nabla\phi|_{\text{cv}} = (\mathcal{A}, \mathcal{B}, C)$, then the best choice of $\nabla\phi|_{\text{cv}}$ is the one that minimizes the functional

$$F(\mathcal{A}, \mathcal{B}, C) = \sum_{\text{nbr}} \left[\phi_{\text{nbr}} - \phi(\mathbf{x}_0) - (\mathcal{A}, \mathcal{B}, C) \cdot (\mathbf{x}_{\text{nbr}} - \mathbf{x}_0)\right]^2 w_{\text{nbr}}, \tag{2.11}$$

where ϕ_{nbr} and $\mathbf{x}_{\text{nbr}}$ denote the values and locations of neighbor cells shown in Figure 2.1 (b). Here w_{nbr} is the weighting function, which is set to be 1 for simplicity and preserving symmetry of scheme. From the condition $\partial F/\partial\mathcal{A} = \partial F/\partial\mathcal{B} = \partial F/\partial\mathcal{C} = 0$, $\nabla\phi|_{\text{cv}}$ is given by the solution of the system

$$\begin{bmatrix} \sum_{\text{nbr}} \Delta x^2 & \sum_{\text{nbr}} \Delta x\Delta y & \sum_{\text{nbr}} \Delta x\Delta z \\ \sum_{\text{nbr}} \Delta x\Delta z & \sum_{\text{nbr}} \Delta y^2 & \sum_{\text{nbr}} \Delta y\Delta z \\ \sum_{\text{nbr}} \Delta x\Delta z & \sum_{\text{nbr}} \Delta y\Delta z & \sum_{\text{nbr}} \Delta z^2 \end{bmatrix} \begin{pmatrix} \mathcal{A} \\ \mathcal{B} \\ \mathcal{C} \end{pmatrix} = \begin{pmatrix} \sum_{\text{nbr}} \Delta\phi_{\text{nbr}}\Delta x \\ \sum_{\text{nbr}} \Delta\phi_{\text{nbr}}\Delta y \\ \sum_{\text{nbr}} \Delta\phi_{\text{nbr}}\Delta z \end{pmatrix}, \tag{2.12}$$

where $\Delta x = x_{\text{nbr}} - x_0$, $\Delta\phi_{\text{nbr}} = \phi_{\text{nbr}} - \phi_0$ and other terms are defined similarly. In the Modified-least square method, the Gauss divergence theorem is invoked to compute $\nabla\phi|_{\text{cv}}$ as follows:

$$\nabla\phi|_{\text{cv}} = \frac{1}{V_{\text{cv}}} \sum_{\text{faces}} \phi^{\star}_{f_c} n_i A_f. \tag{2.13}$$

$\phi^{\star}_{f_c}$ is evaluated as a simple average of the values at the cell centers sharing the face:

$$\phi^{\star}_{f_c} = 0.5(\phi_{icv1} + \phi_{icv2}) \tag{2.14}$$

Note that both the LSQ and MLSQ methods of obtaining the quantities at the face using Eqn. (2.9) are second order accurate. Also, for uniform structured grids, the LSQ

and MLSQ methods reduce to the same formula for evaluating quantities at the face. For a uniform one-dimensional grid with spacing Δx, Eqn. (2.9) using either LSQ or MLSQ reduces to a second order interpolation formula given by

$$\phi_{i+\frac{1}{2}} = \frac{1}{8}\left(-\phi_{i+2} + 5\phi_{i+1} + 5\phi_i - \phi_{i-1}\right), \tag{2.15}$$

where $\phi_{i+1/2}$ is the value at cell face and ϕ_i, ϕ_{i+1}, ... are cell center values. The corresponding finite-difference is

$$\left.\frac{\delta\phi}{\delta x}\right|_i = \frac{-\phi_{i+2} + 6\phi_{i+1} - 6\phi_{i-1} + \phi_{i-2}}{8\Delta x}. \tag{2.16}$$

Park & Mahesh [43] show that the current method of face reconstruction (obtaining derivatives) has better modified wavenumber properties when compared to a non-compact 4th order central difference stencil.

2.1.3 Viscous Flux Computation

The viscous terms involves the computation of σ_{ij} which is given by:

$$\sigma_{ij,f} = \left(\frac{\mu}{Re}\right)_f \left(\left.\frac{\partial u_i}{\partial x_j}\right|_f + \left.\frac{\partial u_j}{\partial x_i}\right|_f - \frac{2}{3}\left.\frac{\partial u_k}{\partial x_k}\right|_f \delta_{ij} \right), \tag{2.17}$$

To compute the viscous stresses, we split the term into two parts. $\sigma_{ij} = \sigma^1_{ij} + \sigma^2_{ij}$ where $\sigma^1_{ij} = \frac{\mu}{Re}\frac{\partial u_i}{\partial x_j}$ and $\sigma^2_{ij} = \frac{\mu}{Re}\left(\frac{\partial u_j}{\partial x_i} - \frac{2}{3}\frac{\partial u_k}{\partial x_k}\delta_{ij}\right)$. σ^2_{ij} can be interpreted as the compressible part, since it vanishes in the incompressible limit. Then, σ^1_{ij}, is computed by

$$\frac{1}{V_{\text{cv}}}\sum_{\text{faces}}\left(\frac{\mu}{Re}\right)_f \left.\frac{\partial u_i}{\partial x_j}\right|_f n_j A_f = \frac{1}{V_{\text{cv}}}\sum_{\text{faces}}\left(\frac{\mu}{Re}\right)_f \left.\frac{\partial u_i}{\partial n}\right|_f A_f. \tag{2.18}$$

Here, the normal gradient at the face is computed by

$$\frac{\partial\phi}{\partial n} = \frac{\phi_{ifn2} - \phi_{ifn1}}{d_f}, \tag{2.19}$$

where $ifn1$ ($ifn2$) is the projection of $icv1$ ($icv2$) onto the extension of normal vector $\mathbf{n}$ as illustrated in Figure 2.1 (c), and d_f is the distance between $ifn1$ and $ifn2$. ϕ_{ifn1} is given by

$$\phi_{ifn1} = \phi_{icv1} + \nabla\phi|_{icv1} \cdot (\mathbf{x}_{ifn1} - \mathbf{x}_{icv1}), \tag{2.20}$$

where a least-square reconstruction method (LSQ) is used to obtain $\nabla\phi$ at $icv1$.

Viscosity at the cell face is given by Eq. (2.9) and LSQ reconstruction. $\sigma^2_{ij,f}$ is constructed by the interpolation of $\sigma^2_{ij}\Big|_{icv1}$ and $\sigma^2_{ij}\Big|_{icv2}$ using Eq. (2.9). Here again, the least-square method is used for all spatial derivatives at cell centers.

2.1.4 Time Advancement

The solution is advanced in time using a second–order explicit Adams–Bashforth scheme in a predictor-corrector fashion wherein shock-capturing is applied in the corrector step as illustrated below:

$$\hat{\mathbf{q}}^{n+1}_{\mathrm{cv}} = \mathbf{q}^{n}_{\mathrm{cv}} + \frac{\Delta t}{2}\left[3\mathbf{rhs}_{\mathrm{cv}}(\mathbf{q}^{n}) - \mathbf{rhs}_{\mathrm{cv}}(\mathbf{q}^{n-1})\right], \tag{2.21}$$

$$\mathbf{q}^{n+1}_{\mathrm{cv}} = \hat{\mathbf{q}}^{n+1}_{\mathrm{cv}} - \frac{\Delta t}{V_{\mathrm{cv}}}\sum_{\mathrm{faces}}\left(\mathbf{F}^{*}_{f}\cdot\mathbf{n}_{f}\right)A_{f}, \tag{2.22}$$

where $\mathbf{rhs}_{\mathrm{cv}}$ represents the right-hand side of Eqns. (2.6–2.8) and $\mathbf{F}^{*}_{f}$ is the filtered numerical flux.

2.1.5 Shock Capturing

The algorithm uses a novel filter–based shock–capturing scheme that localizes numerical dissipation to the vicinity of flow discontinuities. Once the solution is advanced from $\mathbf{q}^{n}_{\mathrm{cv}}$ to $\hat{\mathbf{q}}^{n+1}_{\mathrm{cv}}$, the final solution $\mathbf{q}^{n+1}_{\mathrm{cv}}$ is determined from a corrector-scheme (Eqn. 2.22) similar to Yee, Sandham & Djomehri [67]. The characteristic-based filter proposed by Yee, Sandham & Djomehri [67] to compute $\mathbf{F}^{*}_{f}$ is extended to unstructured grids by Park & Mahesh [43]. The filter numerical flux has the form

$$\mathbf{F}^{*}_{f_c} = \frac{1}{2}\mathbf{R}_{f_c}\mathbf{\Phi}^{*}_{f_c}, \tag{2.23}$$

where $\mathbf{R}$ is the right Eigenvector of $\left[\rho_f v_N,\ (\rho u_i)_f\, v_N + p_f n_i,\ (E_T + p)_f\, v_N\right]^T$ $(i = 1, 2, 3)$. The face value $\mathbf{R}_{f_c} = \mathbf{R}(\mathbf{q}_{icv1}, \mathbf{q}_{icv2})$ is constructed using Roe's average:

$$\mathbf{u}_{f_c,\mathrm{Roe}} \;=\; \frac{\sqrt{\rho_{icv1}}\mathbf{u}_{icv1} + \sqrt{\rho_{icv2}}\mathbf{u}_{icv2}}{\sqrt{\rho_{icv1}} + \sqrt{\rho_{icv2}}},$$

$$
\begin{aligned}
H_{f_c,\mathrm{Roe}} &= \frac{\sqrt{\rho_{icv1}}H_{icv1} + \sqrt{\rho_{icv2}}H_{icv2}}{\sqrt{\rho_{icv1}} + \sqrt{\rho_{icv2}}}, \\
c^2_{f_c,\mathrm{Roe}} &= (\gamma - 1)\left[H_{\mathrm{roe}} - \frac{1}{2}\left(u^2_{f_c,\mathrm{Roe}} + v^2_{f_c,\mathrm{Roe}} + w^2_{f_c,\mathrm{Roe}}\right)\right],
\end{aligned}
\tag{2.24}
$$

where $H = (E_t + p)/\rho$ is the enthalpy and c is the speed of sound. On the other hand, the expression for the ℓ-th component of $\mathbf{\Phi}^*$, $\phi^{*\ell}$ is given by

$$
\phi^{*\ell}_{f_c} = \kappa \theta^{\ell}_{f_c} \phi^{\ell}_{f_c}, \tag{2.25}
$$

where κ is the adjustable parameter and θ_{f_c} is the switch function given by

$$
\begin{aligned}
\theta_{f_c} &= \sqrt{0.5\left(\hat{\theta}^2_{icv1} + \hat{\theta}^2_{icv2}\right)}, \\
\hat{\theta}_{icv1} &= \left|\frac{|\alpha_{f_c}| - |\alpha_{f_1}|}{|\alpha_{f_c}| + |\alpha_{f_1}|}\right|^p, \\
\hat{\theta}_{icv2} &= \left|\frac{|\alpha_{f_2}| - |\alpha_{f_c}|}{|\alpha_{f_2}| + |\alpha_{f_c}|}\right|^p.
\end{aligned}
\tag{2.26}
$$

Here, $\alpha_f = \mathbf{R}_f^{-1}\Delta\mathbf{q} = \mathbf{R}_f^{-1}(\mathbf{q}_{icv2} - \mathbf{q}_{icv1})$ is the difference of the characteristic variable across the face, and $p = 1$ is used. The reader is referred to Park & Mahesh [43] for further details of the algorithm. Note that no explicit filtering is performed in the code.

The numerical method been used to study transition to turbulence induced by distributed roughness in a Mach 2.9 boundary layer in Muppidi & Mahesh [41] and transition to turbulence using blowing and suction at Mach 2.25 in Muppidi & Mahesh [39] where the turbulent statistics showed good agreement with experimental data at similar conditions. The algorithm has also been used to study the interaction of a supersonic jet with a subsonic crossflow and a sonic jet with a supersonic crossflow in Chai & Mahesh [11] where comparison of mean velocity profiles showed good agreement with experiments. Also, DNS of shock–turbulence interaction at Mach 2.9 in a compression corner was studied in Muppidi & Mahesh [40] using the current methodology.

2.2 Linear Stability Theory (LST) algorithm

The compressible Linear Stability equations are solved using a 2nd order finite difference method proposed by Malik[33]. The governing compressible Navier–Stokes equations

written in non–conservative form are as follows:

$$\begin{aligned}
\frac{\partial \rho}{\partial t} + \frac{\partial}{\partial x_k}(\rho u_k) &= 0 \\
\rho(\frac{\partial u_i}{\partial t} + u_j \frac{\partial u_i}{\partial x_j}) &= \frac{\partial}{\partial x_k}(-p\delta_{ik} + \sigma_{ik}) \qquad (2.27) \\
\rho C_p(\frac{\partial T}{\partial t} + u_j \frac{\partial T}{\partial x_j}) &= \frac{\partial}{\partial x_k}(k\frac{\partial T}{\partial x_k}) + \frac{\partial p}{\partial t} + u_j \frac{\partial p}{\partial x_j} + \Phi \qquad (2.28)
\end{aligned}$$

where ρ, u_i, T and p are density, velocity, temperature and pressure respectively. The ideal gas assumption is used and Φ is the viscous dissipation given below:

$$\begin{aligned}
p &= \rho R T \\
\Phi &= \lambda(\frac{\partial u_j}{\partial x_j})^2 + \frac{\mu}{2}(\frac{\partial u_i}{\partial x_j} + \frac{\partial u_j}{\partial x_i})^2 \qquad (2.29)
\end{aligned}$$

2.2.1 Boundary layer similarity solution

A boundary layer similarity solution is used as the base flow for the Linear Stability calculations. The Illingworth–Stewartson transformation (Schlichting [58]) is used in the compressible boundary layer equations. The similarity variables are as follows:

$$\begin{aligned}
d\xi &= \int_0^x \rho_e u_e \mu_e dx \\
d\eta &= \frac{u_e}{\sqrt{2\xi}} \int_0^y \rho dy \qquad (2.30)
\end{aligned}$$

where ρ_e, u_e and μ_e are the density, velocity and viscosity at the edge of the boundary layer. Note that ξ depends only on the streamwise direction x. Substituting the above similarity variables into the boundary layer equations, we get the following similarity equation for a two-dimensional, steady boundary layer:

$$\begin{aligned}
(Cf'')' + ff'' &= 0 \\
(\frac{C}{Pr}g')' + fg' + C\frac{u_e^2}{h_e}(f'')^2 &= 0 \qquad (2.31)
\end{aligned}$$

where $f' = \partial f/\partial \eta = u/u_e$, $g = T/T_e$, $C = \rho\mu/\rho_e\mu_e$ and $Pr = C_p\mu/k$. The boundary conditions used to solve the similarity equations are as follows:

At $\eta = 0$, $f = f' = 0$, $g = g_w$ (isothermal wall) or $g' = 0$ (adiabatic wall).

At $\eta = \eta_{max}$, $f' = 1$, $g = 1$. A shooting method was used to solve the equations (Hou [68]).

2.2.2 Linear Stability Equations

Each of the variables is expressed as a sum of a base flow and perturbation as follows:

$$\begin{aligned} u = \overline{U} + \tilde{u}, \qquad v = \overline{V} + \tilde{v}, \qquad w &= \overline{W} + \tilde{w} \\ p = \overline{P} + \tilde{p}, \qquad T = \overline{T} + \tilde{T}, \qquad \rho &= \overline{\rho} + \tilde{\rho} \\ \mu = \overline{\mu} + \tilde{\mu}, \qquad \lambda = \overline{\lambda} + \tilde{\lambda}, \qquad k &= \overline{k} + \tilde{k} \end{aligned}$$

Neglecting non-linear perturbation terms, the non-dimensional equation of state for the baseflow and perturbations becomes :

$$\gamma M^2 p = \rho T \tag{2.32}$$

$$\tilde{\rho} = \gamma M^2 \frac{\tilde{p}}{T} - \frac{\tilde{T}}{T^2} \tag{2.33}$$

The perturbation quantities for viscosity and thermal conductivity is expressed as:

$$\tilde{\mu} = \frac{d\mu}{dT}\tilde{T}, \qquad \tilde{\lambda} = \frac{d\lambda}{dT}\tilde{T}, \qquad \tilde{k} = \frac{k}{T}\tilde{T} \tag{2.34}$$

Substituting the above equations into the compressible Navier-Stokes equations, subtracting the base flow (which also satisfy the Navier-Stokes equations) and neglecting non-linear perturbation terms, we get:

$$\begin{aligned} \left(\frac{\partial \tilde{u}}{\partial t} + U\frac{\partial \tilde{u}}{\partial x} + \tilde{v}\frac{dU}{dy} + W\frac{\partial \tilde{u}}{\partial z}\right)/T = -\frac{\partial \tilde{p}}{\partial x} + \frac{\mu}{R}\Bigg[& l_2\frac{\partial^2 \tilde{u}}{\partial x^2} + l_1\left(\frac{\partial^2 \tilde{v}}{\partial x \partial y} + \frac{\partial^2 \tilde{w}}{\partial x \partial z}\right) + \\ & \frac{\partial^2 \tilde{u}}{\partial y^2} + \frac{\partial^2 \tilde{u}}{\partial z^2} + \frac{1}{\mu}\frac{d\mu}{dT}\frac{dT}{dy}\left(\frac{\partial \tilde{u}}{\partial y} + \frac{\partial \tilde{v}}{\partial x}\right) + \\ & \frac{1}{\mu}\frac{d\mu}{dT}\left(\frac{d^2U}{dy^2}\tilde{T} + \frac{dU}{dy}\frac{\partial \tilde{T}}{\partial y}\right) + \frac{1}{\mu}\frac{d^2\mu}{dT^2}\frac{dT}{dy}\frac{dU}{dy}\tilde{T}\Bigg] \end{aligned} \tag{2.35}$$

$$\begin{aligned} \left(\frac{\partial \tilde{v}}{\partial t} + U\frac{\partial \tilde{v}}{\partial x} + \tilde{v}\frac{dU}{dy} + W\frac{\partial \tilde{v}}{\partial z}\right)/T = -\frac{\partial \tilde{p}}{\partial y} + \frac{\mu}{R}\Bigg[& \frac{\partial^2 \tilde{v}}{\partial x^2} + l_1\left(\frac{\partial^2 \tilde{u}}{\partial x \partial y} + \frac{\partial^2 \tilde{w}}{\partial y \partial z}\right) + \\ & l_2\frac{\partial^2 \tilde{v}}{\partial y^2} + \frac{\partial^2 \tilde{v}}{\partial z^2} + \frac{1}{\mu}\frac{d\mu}{dT}\left(\frac{\partial \tilde{T}}{\partial x}\frac{dU}{dy} + \frac{\partial \tilde{T}}{\partial z}\frac{dW}{dy}\right) \\ & \frac{1}{\mu}\frac{d\mu}{dT}\frac{dT}{dy}\left\{l_0\left(\frac{\partial \tilde{u}}{\partial x} + \frac{\partial \tilde{w}}{\partial z}\right) + l_2\frac{\partial \tilde{v}}{\partial y}\right\}\Bigg] \end{aligned} \tag{2.36}$$

$$\left(\frac{\partial\tilde{w}}{\partial t}+U\frac{\partial\tilde{w}}{\partial x}+\tilde{v}\frac{dW}{dy}+W\frac{\partial\tilde{w}}{\partial z}\right)/T=-\frac{\partial\tilde{p}}{\partial z}+\frac{\mu}{R}\left[\frac{\partial^2\tilde{w}}{\partial x^2}+l_1\left(\frac{\partial^2\tilde{u}}{\partial x\partial w}+\frac{\partial^2\tilde{v}}{\partial y\partial z}\right)+\right.$$
$$\frac{\partial^2\tilde{w}}{\partial y^2}+l_2\frac{\partial^2\tilde{w}}{\partial z^2}+\frac{1}{\mu}\frac{d\mu}{dT}\frac{dT}{dy}\left(\frac{\partial\tilde{v}}{\partial z}+\frac{\partial\tilde{w}}{\partial y}\right)+$$
$$\left.\frac{1}{\mu}\frac{d\mu}{dT}\left(\frac{d^2W}{dy^2}\tilde{T}+\frac{dW}{dy}\frac{\partial\tilde{T}}{\partial y}\right)+\frac{1}{\mu}\frac{d^2\mu}{dT^2}\frac{dT}{dy}\frac{dW}{dy}\tilde{T}\right] \quad (2.37)$$

$$\frac{\gamma M^2}{T}\frac{\partial\tilde{p}}{\partial t}-\frac{1}{T^2}\frac{\partial\tilde{T}}{\partial t}+\frac{1}{T}\frac{\partial\tilde{u}}{\partial x}+U\left(\frac{\gamma M^2}{T}\frac{\partial\tilde{p}}{\partial x}-\frac{1}{T^2}\frac{\partial\tilde{T}}{\partial x}\right)+$$
$$\frac{1}{T}\frac{\partial\tilde{v}}{\partial y}-\frac{1}{T^2}\frac{dT}{dy}\tilde{v}+\frac{1}{T}\frac{\partial\tilde{w}}{\partial z}+W\left(\frac{\gamma M^2}{T}\frac{\partial\tilde{p}}{\partial z}-\frac{1}{T^2}\frac{\partial\tilde{T}}{\partial z}\right)=0 \quad (2.38)$$

$$\left(\frac{\partial\tilde{T}}{\partial t}+U\frac{\partial\tilde{T}}{\partial x}+\tilde{v}\frac{dT}{dy}+W\frac{\partial\tilde{T}}{\partial z}\right)/T=(\gamma-1)M^2\left[\frac{\partial\tilde{p}}{\partial t}+U\frac{\partial\tilde{p}}{\partial x}+W\frac{\partial\tilde{p}}{\partial z}\right]+$$
$$\frac{\mu}{R\sigma}\left[\frac{\partial^2\tilde{T}}{\partial x^2}+\frac{\partial^2\tilde{T}}{\partial y^2}+\frac{\partial^2\tilde{T}}{\partial z^2}+\frac{2}{k}\frac{dk}{dT}\frac{dT}{dy}\frac{\partial\tilde{T}}{\partial y}+\left(\frac{1}{k}\frac{dk}{dT}\frac{d^2T}{dy^2}+\frac{1}{k}\frac{d^2k}{dT^2}\left(\frac{dT}{dy}\right)^2\right)\tilde{T}\right]+$$
$$(\gamma-1)M^2\frac{\mu}{R}\left[2\frac{dU}{dy}\left(\frac{\partial\tilde{u}}{\partial y}+\frac{\partial\tilde{v}}{\partial x}\right)+2\frac{dW}{dy}\left(\frac{\partial\tilde{v}}{\partial z}+\frac{\partial\tilde{w}}{\partial y}\right)\right]+$$
$$(\gamma-1)M^2\frac{\mu}{R}\left[\frac{1}{\mu}\frac{d\mu}{dT}\left(\left(\frac{dU}{dy}\right)^2+\left(\frac{dW}{dy}\right)^2\right)\right] \quad (2.39)$$

The above equations are the governing linear stability equations. Expanding the variables in normal-mode expansion,

$$\begin{aligned}\phi &= \{u,v,p,T,w\}^{tr}\\ \tilde{\phi} &= \hat{\phi}e^{i(\alpha x+\beta z-\omega t)}\end{aligned} \quad (2.40)$$

where α and β are the streamwise and spanwise wavenumbers respectively and ω is the angular frequency of the waves. Substituting the above into equations 2.35-2.39, we get the following in matrix form:

$$(AD^2+BD+C)\phi=0, D=d/dy \quad (2.41)$$

In the above equations, α and β are real and ω is complex which needs to be solved by the above equation which gives rise to an eigenvalue problem. Real wavenumbers and complex frequency is referred to as temporal stability wherein the temporal evolution of the wave is sought. For the temporal stability problem, where $\omega=\omega_r+i\omega_i$, ω_r

gives the angular frequency of the wave and ω_i determines whether the wave is stable or unstable. If $\omega_i > 0$, the wave is unstable since the perturbation grows in time according to equation 2.40. Else if $\omega_i < 0$, the wave is stable since the perturbation decays in time.

2.2.3 Finite Difference Solver

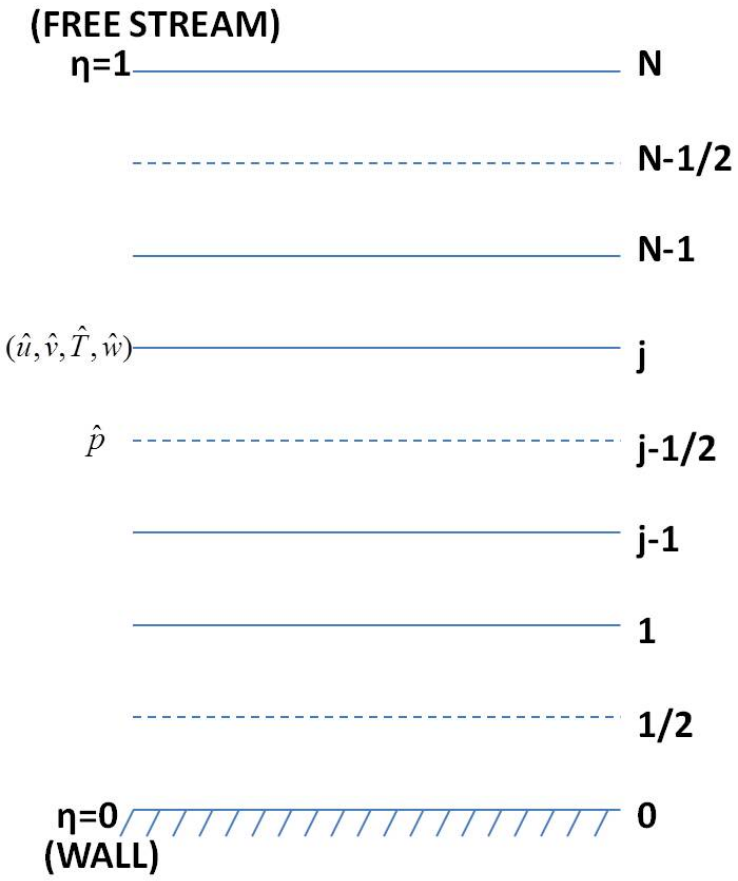

Figure 2.2: Figure showing the staggered grid used for linear stability theory (LST) code calculation. Note that the velocities and temperature are stored at j while the pressure is stored at $j - 1/2$.

The linear stability equations (2.41) is solved using a second–order finite difference method following the method used by Malik [33]. A second order staggered grid is used as shown in Figure 2.2. The velocities and temperature are stored at j while the

pressure is stored at $j+1/2$. The momentum and energy equations are solved at j while the continuity equation is solved at $j+1/2$.

The boundary conditions used are as follows:

$$\begin{aligned} y = 0: \quad & \phi_1 = \phi_2 = \phi_4 = \phi_5 = 0 \\ y = y_{max}: \quad & \phi_1 = \phi_2 = \phi_4 = \phi_5 = 0 \end{aligned} \tag{2.42}$$

A mapping is used to solve the stability equations as follows (Malik [33]):

$$\begin{aligned} y &= \frac{a\eta}{(b-\eta)} \\ b &= 1 + \frac{a}{y_{max}} \\ a &= \frac{y_{max} y_i}{(y_{max} - 2y_i)} \end{aligned} \tag{2.43}$$

The mapping puts half the number of grid points within $y = y_i$, which can be chosen as a suitable boundary layer thickness depending on the nature of the unstable mode to be captured. The stability equations in the η domain is as follows:

$$A_j\Big[\frac{\phi_{j+1} - 2\phi_j + \phi_{j-1}}{\Delta\eta^2}\Big] + d_1\Big[(f_2 A_j + f_3 B_j)(\frac{\phi_{j+1} - \phi_{j-1}}{2\Delta\eta}) + C_j\phi_j\Big]$$

$$+d_2\Big[f_3 B_j(\frac{\phi_{j+1/2} - \phi_{j-1/2}}{\Delta\eta}) + C_j(\frac{\phi_{j+1/2} + \phi_{j-1/2}}{2})\Big] = 0 (j = 1, ...N-1) \tag{2.44}$$

$$f_3 B_{j+1/2}(\frac{\phi j + 1 - \phi_j}{\Delta\eta}) + C_{j+1/2}\phi_{j+1/2} = 0 (j = 0, ..., N-1) \tag{2.45}$$

In the above equations, ϕ_j is the value of ϕ at $\eta = j/N$. Equation 2.44 is used for momentum and energy equations while Equation 2.45 is used for the continuity equation. $d_1 = 0, d_2 = 1$ for $\hat{p}$ while $d_1 = 1, d_2 = 0$ for $\hat{u}, \hat{v}, \hat{T}, \hat{w}$. The above equations along with the boundary conditions in Equation 2.42 gives the following matrix eigenvalue problem for the temporal stability problem :

$$\bar{A}\Phi = \omega\bar{B}\Phi \tag{2.46}$$

M_∞	$R = \frac{Lu_\infty}{\nu_\infty}$	$\frac{T_w}{T_{adb}}$	α	β	ω (Malik [33])	ω (Current)
0.5	2000	1	0.1	0	0.02908+i0.002231	0.02908+i0.002244
10^{-6}	580	1	0.179	0	0.06518+i0.001403	0.06517+i0.001414
2.5	3000	1	0.06	0.1	0.03673+i0.000579	0.03673+i0.000584
10.0	2000	0.1	0.105	0	0.097431+i0.002085	0.09748+i0.002032
10.0	1000	1	0.12	0	0.115847+i0.000141	0.11585+i0.0001357

Table 2.1: Table showing the flow conditions and results for validation of the LST code with results of Malik [33].

The linear stability code is validated for a range of flow conditions with the results of Malik [33]. The flow conditions are listed in Table 2.1. $L = \sqrt{\nu_\infty x/u_\infty}$ is used as the reference length scale. 200 grid points were used for the results reported. The value from Malik [33] was obtained using a Multi-Domain Spectral collocation method. y_i in Equation 2.43 was chosen to be the displacement thickness of the base flow boundary layer. Excellent agreement is observed between the current results and those of Malik [33]. The code is tested over a range of Mach numbers from incompressible ($M_\infty = 10^{-6}$) to hypersonic ($M_\infty = 10$) for both two-dimensional ($\beta = 0$) and three-dimensional disturbances($\beta \neq 0$).

Figure 2.3 shows the comparison of the eigenfunctions ($\hat{\phi}$) of the unstable mode between our code and those of Malik [33]. Excellent agreement is observed. $\hat{u_r}$, $\hat{u_i}$ and $\hat{v_r}$ are shown for $M_\infty = 10^{-6}$ which is the Tollmein-Schlichting (TS) mode which is dominant inside the boundary layer. In contrast, the inviscid second Mack mode is most unstable for $M_\infty = 10$ and $R = 1000$ where the $\hat{T_r}$ and $\hat{T_i}$ are dominant away from the wall and closer to the boundary layer edge.

The effect of resolution on the eigenfunctions of the unstable mode are shown in Figure 2.4. Figures (a) and (b) depict $\hat{T_r}$ and $\hat{w_r}$ respectively for $M_\infty = 2.5$ and Figures (c) and (d) depict $\hat{T_r}$ and $\hat{u_r}$ respectively for $M_\infty = 10$, $R = 1000$. Note that the unstable mode is captured with just 24 grid points. The lower $M_\infty = 2.5$ converges faster as compared to $M_\infty = 10$ case.

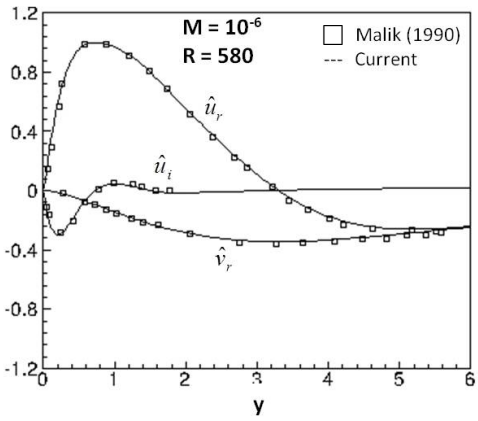

(a) $M_\infty = 10^{-6}$, R =580

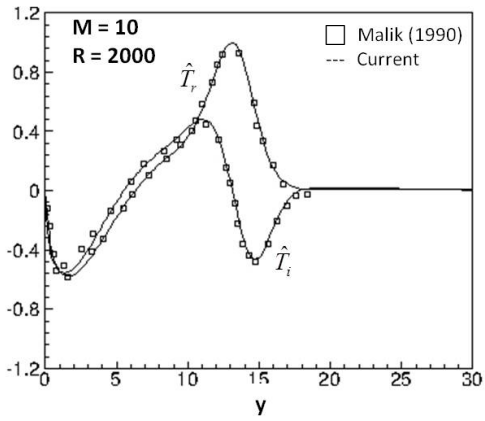

(b) $M_\infty = 10$, $R = 2000$

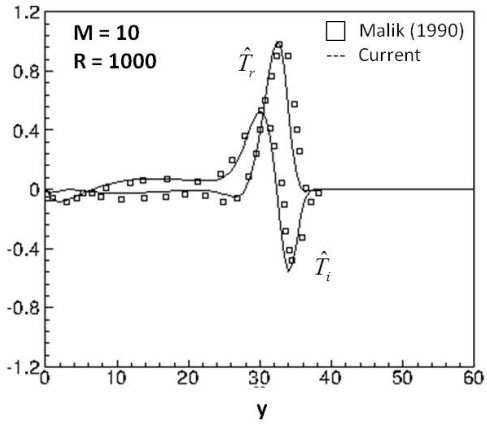

(c) $M_\infty = 10$, $R = 1000$

Figure 2.3: Figure showing comparison of eigenfunctions obtained from LST code (line) with those of Malik [33] for (a) $M_\infty = 10^{-6}$, R =580, (b) $M_\infty = 10$, $R = 2000$ and (c) $M_\infty = 10$, $R = 1000$. Excellent agreement is observed.

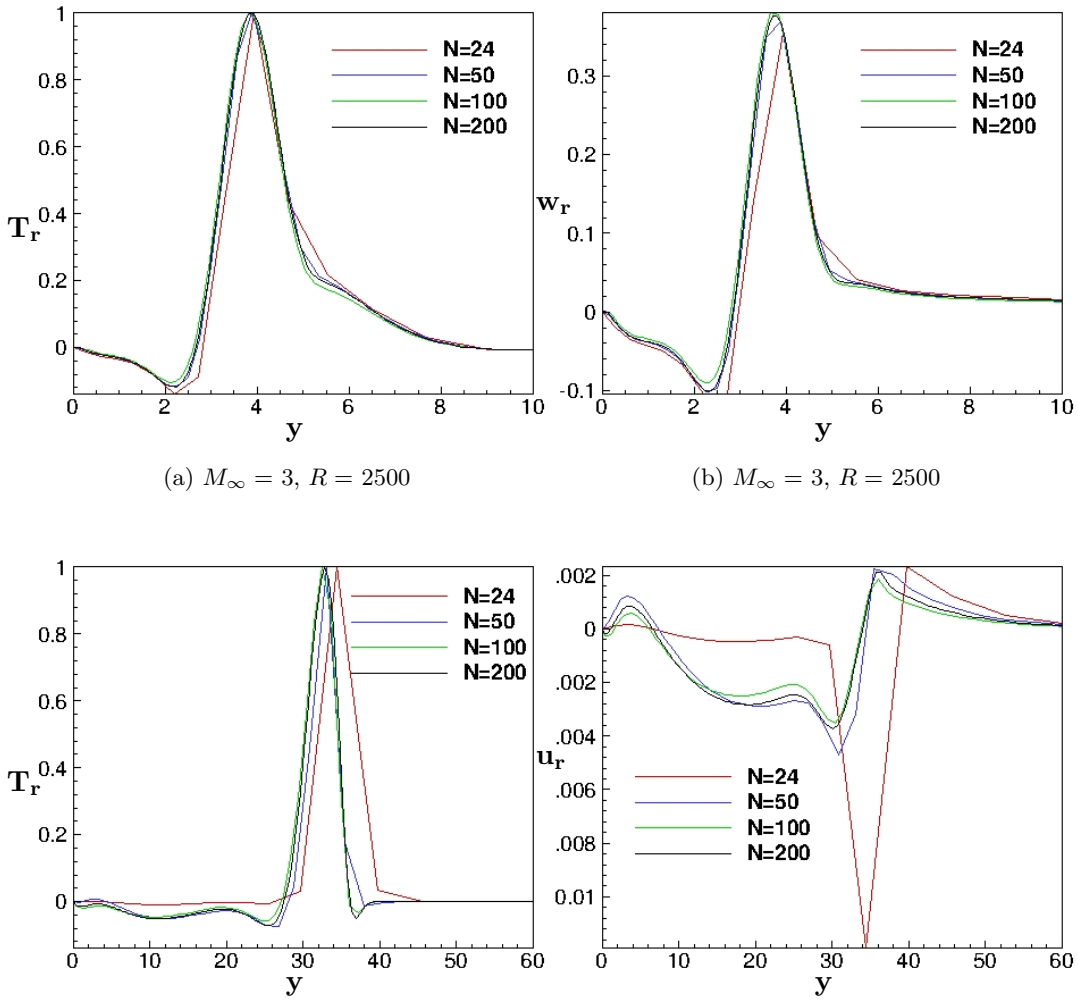

(a) $M_\infty = 3$, $R = 2500$

(b) $M_\infty = 3$, $R = 2500$

(c) $M_\infty = 10$, $R = 1000$

(d) $M_\infty = 10$, $R = 1000$

Figure 2.4: The effect of resolution on the eigenfunction of the most unstable mode is shown for $M_\infty = 3$ and 10. Note that while the mode is captured with just 24 points, 100 points are required to sufficiently resolve the spatial variation of the eigenfunctions.

2.3 Validation with Linear Stability Theory (LST)

The algorithm described in Section 2.1 is validated against Linear Stability Theory (LST) to demonstrate its suitability for transitional simulations. We follow closely the analysis by Zhong [69] and Dong & Zhong [24] and present results for a supersonic Couette flow at M_∞=2.0 and a supersonic boundary layer at M_∞=4.5. The linear stability code uses a 2nd order staggered finite difference scheme (2FD) described in Section 2.2.3.

We use the temporal theory for two-dimensional disturbances where α is real, β=0 and ω is complex for our comparison. The DNS is initialized with the eigenmode obtained from the linear stability code and the non-linear Navier-stokes equations are solved using the finite-volume algorithm described in Section 2.1. The conservative variables, $\mathbf{q} = (\rho, \rho u_i, E_T)$ are initialized as follows: $\mathbf{q} = \bar{\mathbf{q}}(\mathbf{y}) + \epsilon Re(\tilde{\mathbf{q}})$, where $\bar{q}(y)$ is obtained from similarity solution, $\tilde{q}$ is obtained from $\tilde{\phi}$ obtained from the LST code, Re denotes the real part of the variable and $\epsilon = 0.001$ for both the validation cases presented.

2.3.1 Supersonic Couette flow

For the Couette flow problem, $M_\infty = 2$ and $Re_\infty = 1000$ (based on spacing between the walls). The upper wall is an isothermal wall with $T_\infty = 220.667$K while the lower wall is an adiabatic wall. The fluid is assumed to be an ideal gas with $\gamma = 1.4$ and $Pr = 0.72$. Sutherland's law is used to compute viscosity. The DNS is initialized with a stable mode which has a dimensionless wavenumber $\alpha = 3.0$. The eigenvalue obtained from temporal LST is $\omega = 5.524567$ -i0.134598 for stretched grid using 100 points.

Figure 2.5 shows results from DNS compared with LST for validation. The DNS is carried out in a two-dimensional domain covering one wavelength of $\alpha = 3.0$ in the x–direction. Periodic boundary conditions are used in the streamwise direction. The DNS was carried out using a 50X20, 50X50 and 100X100 grids with uniform grid spacing in the streamwise direction.

Figure 2.5 (a) shows the comparison of disturbance velocities obtained from DNS and LST for 100X100 grid at a random location in the domain and we see that the agreement is good. To compare the amplification rate (ω_i) from DNS to LST, we plot

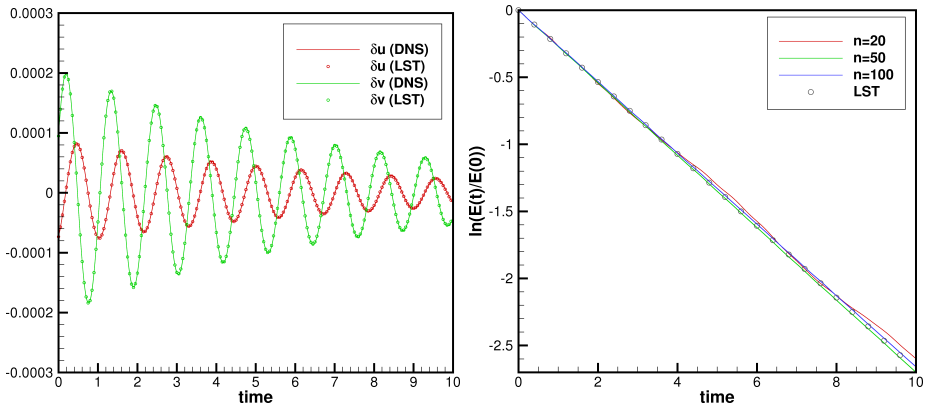

(a) (b)

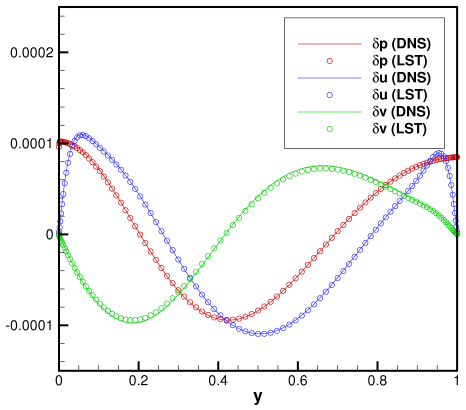

(c)

Figure 2.5: Validation with LST for Couette flow with (a) showing the time variation of perturbation velocities at a point in the domain, (b) showing the variation of perturbation kinetic energy of the domain with time where N indicates the number of points in y and (c) showing the wall-normal variation of perturbation quantities at $x = 0.963$.

the perturbation kinetic energy with time in Figure 2.5 (b). From linear stability theory, the perturbation kinetic energy is given by:

$$E(t) = \int\int \frac{1}{2}(u'^2 + v'^2)dxdy = E_0 e^{2\omega_i t}, \tag{2.47}$$

where E_0 is the initial perturbation energy. We see that the good agreement is observed between the expected ω_i and that obtained from DNS. Figure 2.5 (c) shows the variation of perturbation quantities with y at $x = 0.963$ from DNS and LST after 5 units of time for 100X100 grid and we see that the agreement is good.

2.3.2 Supersonic boundary layer

For the boundary layer flow problem, $M_\infty = 4.5$ and $Re_\infty = 1500$ (based on the boundary layer scaling $l = \sqrt{\nu_\infty x/u_\infty}$). y_{max} is set to 100. $T_\infty = 121$K and the wall is set to be adiabatic. The flow conditions are the same as a test case in Malik [33] with the same grid stretching being used here. The DNS is initialized with an unstable mode which has a dimensionless wavenumber $\alpha = 0.25$. The grid in the y-direction is identical in the DNS and LST computations. The eigenvalue obtained from temporal LST is $\omega = 0.227491 + i0.002296$ for stretched grid using 300 points. Figure 2.6 shows results from DNS compared with LST for validation. The DNS is carried out in a two-dimensional domain covering one wavelength of $\alpha = 0.25$ in the x–direction. Periodic boundary conditions are used in the streamwise direction. The DNS was carried out using a 100X50, 100X100, 100X200 and 100X300 grids with uniform grid spacing in the streamwise direction. The 100X100 grid has approximately 60 points within the boundary layer and is representative of the fine grid used in the the roughness-induced transition study.

Figure 2.6 (a) shows the comparison of disturbance velocities obtained from DNS and LST for 100X100 grid at a random location in the domain and we see that the agreement is good. To compare the amplification rate (ω_i) from DNS to LST, we plot the perturbation kinetic energy with time in Figure 2.6 (b). We see that good agreement is observed between the expected ω_i and that obtained from DNS. Figure 2.6 (c) shows the variation of perturbation quantities with y at the inflow plane after 100 units of time for 100X100 grid from DNS and LST and we see that the agreement is good.

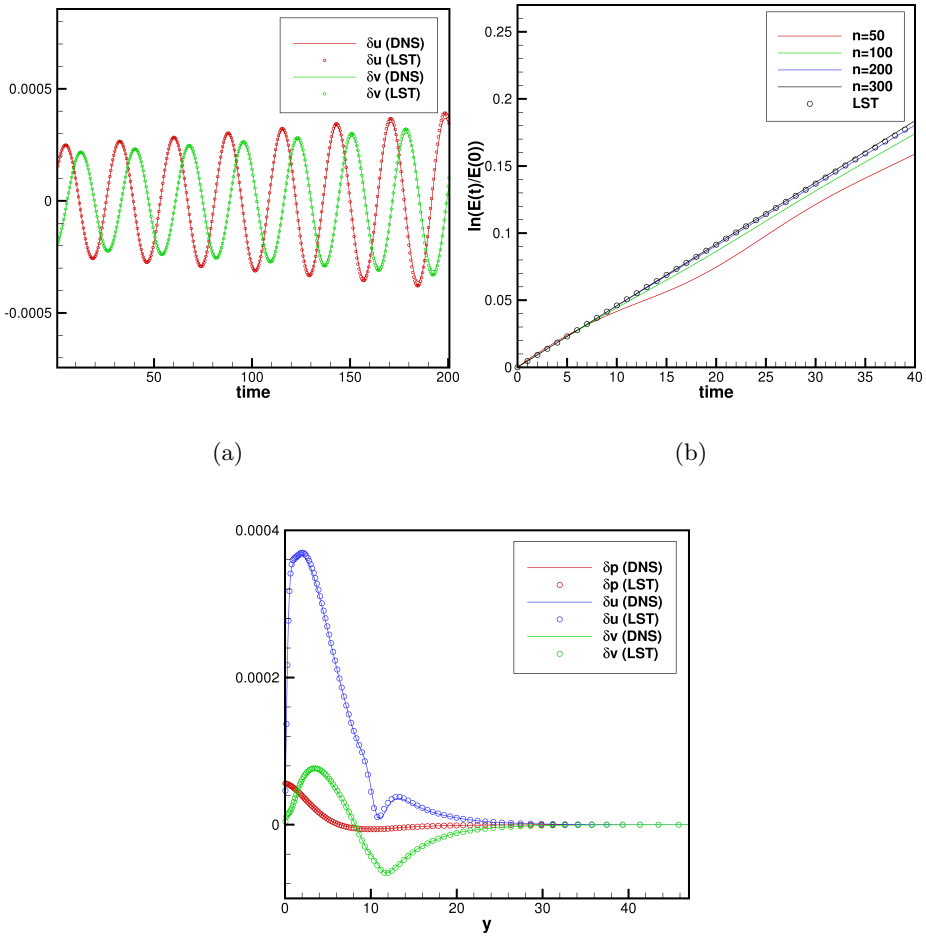

(a) (b)

(c)

Figure 2.6: Validation with LST for boundary layer flow with (a) showing the time variation of perturbation velocities at a point in the domain, (b) showing the variation of perturbation kinetic energy of the domain with time where N indicates the number of points in y and (c) showing the wall-normal variation of perturbation quantities at the inflow plane.

Chapter 3

Flow past a cylindrical roughness element

3.1 Problem Description

Flow past a cylindrical roughness element placed on a flat plate is simulated at conditions that match the experiments of Bathel *et al.* [7]. The oncoming Mach 8.12 boundary layer remains laminar downstream of the roughness. The velocity profiles obtained are compared to those of Bathel *et al.* [7] for validating our algorithm to study roughness effects on high Mach number flows.

The experimental setup shown in Figure 3.1 consists of a wedge placed at 5° to an incoming Mach 10 flow at 51.32K with unit Reynolds number Re =1.7 $million/m$, yielding a free-stream Mach number of 8.12 and an $Re_k = u_\infty k/\nu_\infty = 4740$. The roughness element with a height $k = 2mm$, diameter $D = 4\ mm$ is placed on the top surface of the wedge at a distance of 75.4 mm (18.85D) from the leading edge of the wedge. The top surface of the wedge is 157.2 mm (39.3D) long and 127 mm (31.75D) wide. Pure NO was seeded into the laminar boundary layer from an 11-mm-long, 0.81-mm-wide slot centered on the symmetry plane and 29.4-mm downstream of the leading edge. A shock wave forms at the leading edge of the wedge and post-shock conditions yield the free–stream conditions for the top surface of the wedge (and the roughness element). The wall is maintained at a constant temperature of 300K.

The simulations model the post-shock flow over the top surface of the wedge as

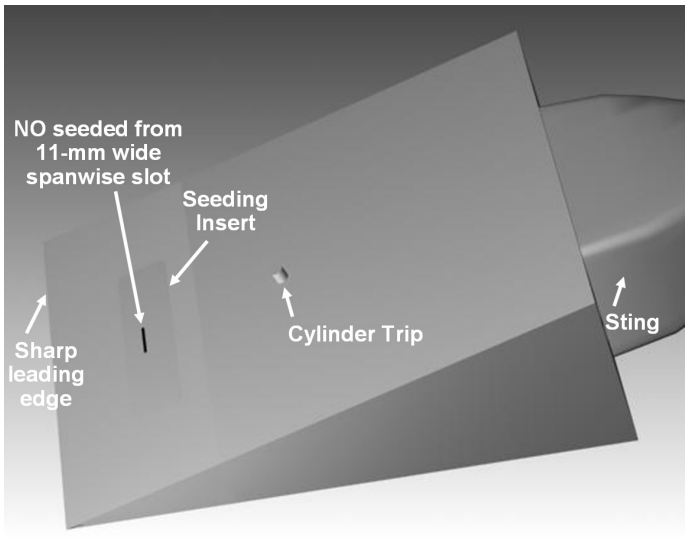

Figure 3.1: Figure showing the experimental setup used by Bathel *et al.* [7]. Figure taken from Danehy *et al.* [21].

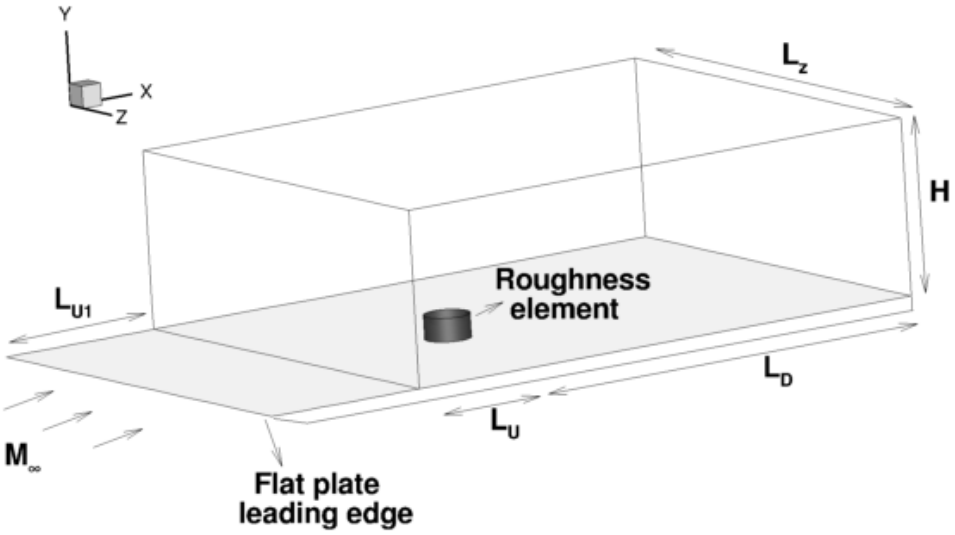

Figure 3.2: Figure showing a schematic of the computational domain represented by a box. A compressible similarity solution is prescribed at the inflow plane.

flow over a flat plate. The post-shock conditions were obtained from the Rankine–Hugoniot equations which were specified as free-stream conditions for the flat plate. The free-stream temperature $T_\infty = 73.12K$ and $k/\delta = 0.64$, where k is the height of the roughness and δ is the laminar boundary layer thickness at the location of the roughness element. The compressible Navier–Stokes equations are solved in non–dimensional form as follows:

$$\rho = \rho^*/\rho^*_\infty \quad u = u^*/u^*_\infty \quad T = T^*/T^*_\infty \quad p = p^*/\rho^*_\infty u^{*2}_\infty \quad x_i = x^*_i/D \quad t = t^* u_\infty/D, \tag{3.1}$$

where the superscript (*) denotes dimensional values.

3.2 Grid parameters

A schematic of the computational domain is shown in Figure 3.2. The inflow of the computational domain is at a distance of L_{U1} from the leading edge of the flat plate. A compressible boundary layer similarity solution is prescribed at the inflow domain to yield the experimental boundary layer thickness at the location of the roughness if it were absent. The distance between the roughness element and the inflow and outflow planes are L_U and L_D respectively. The height of the domain is H and the spanwise domain is of length L_z. The domain extents are listed for the flow with and without injection in Table 3.1.

Simulation	L_{U1}/D	L_U/D	L_D/D	L_z/D	H/D
Without upstream injection	8.85	10.0	22	20	10
With upstream injection	1.35	17.5	22	20	10

Table 3.1: Table listing the dimensions of the computational domain used in the cylindrical roughness study.

A top view of the grid used for the cylindrical roughness case with injection is shown in Figure 3.3. The same grid is used without injection, with the inflow plane of the domain located closer to the roughness element. Note that the grid is fine in the vicinity of the roughness and coarsens in the laminar regions of the flow. There are 480

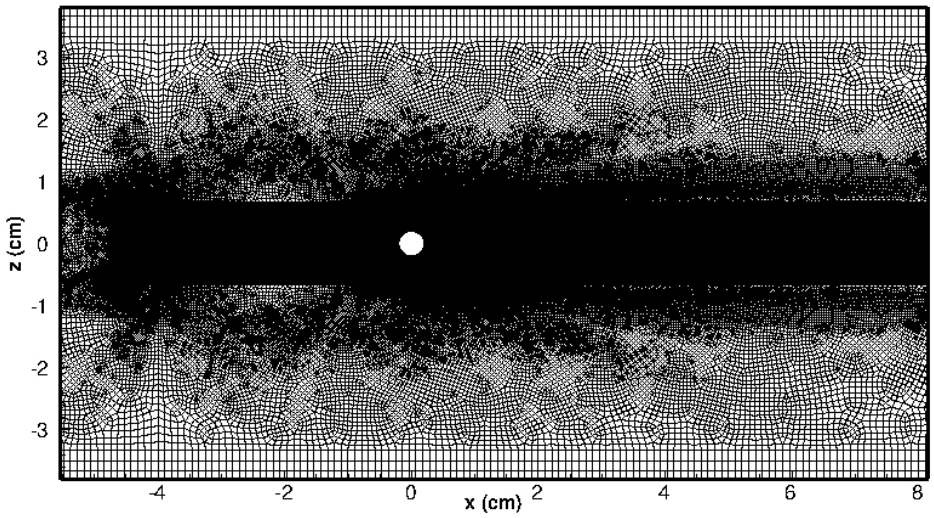

Figure 3.3: Top view of the grid used to study the the effect of upstream injection. Note that the grid is fine around the roughness element and coarser away from it.

grid points in the circumference of the roughness and 30X100 points in the rectangular slot injection region. Downstream of the roughness, $\Delta x = 0.0066\ cm$ and $\Delta z = 0.007\ cm$. There are about 25 points in the wall–normal direction within the height of the roughness with a minimum wall spacing of $0.004\ cm$. The grid is composed of 13 and 16 million hexahedral elements for the flow without and with injection respectively.

3.3 Flow past isolated cylindrical roughness

This Section presents results from the DNS of flow past an isolated cylindrical roughness element without any upstream injection to compare the velocity profiles to those obtained from the experiments of Bathel *et al.* [7]. While the overall comparisons is used to validate our algorithm described in Section 2.1 to study high–speed boundary layer flows, the DNS data is also used in this section to estimate the difference in the velocity profiles that could be caused by uncertainties in the experimental technique.

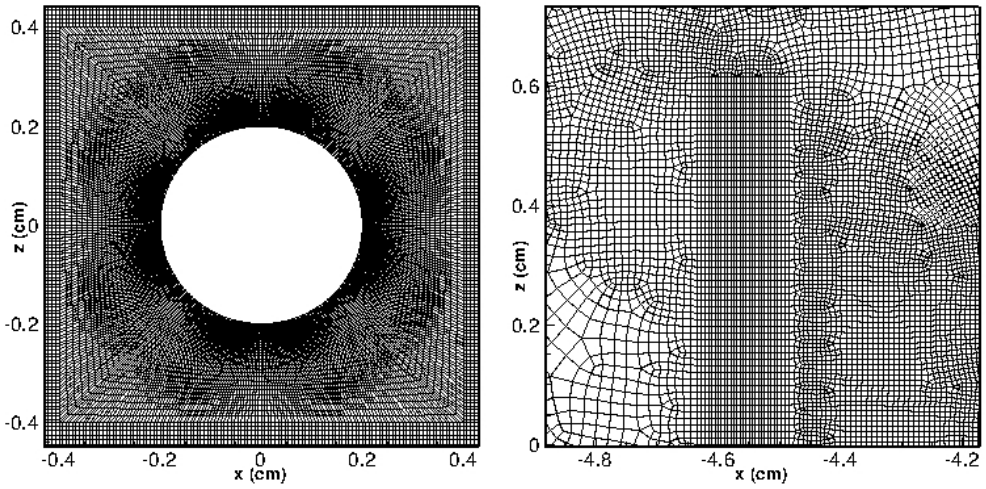

Figure 3.4: Top view of the grid used to study the the effect of upstream injection showing a close up around the cylinder (left) and around the injection slot (right).

3.3.1 Flowfield description

Instantaneous divergence contours in the symmetry plane, temperature contours in streamwise planes $(y-z)$ and streamwise velocity contours in the wall parallel plane are shown in Figure 3.5. Note that the flow does not undergo transition downstream of the roughness. The shock wave produced by the roughness is clearly visible. The roughness element gives rise to coherent streamwise vortices downstream of it which transport momentum to and away from the wall giving rise to high and low–speed streaks in the wall–parallel plane. Note the high–speed streaks in the wall–parallel plane in Figure 3.5. With increasing downstream distance, the strength of the high-speed streak decreases indicating that the flow does not undergo transition. The streamwise vortices give rise to inflection points as can be seen in the streamwise planes which may render the flow unstable to small perturbations depending on the flow conditions.

3.3.2 Velocity profile comparisons

Velocity profiles in the spanwise symmetry plane and a wall–parallel plane 2.1 mm from the wall are compared to the experiments at different streamwise stations as shown in Figure 3.6. The experiment (Bathel *et al.* [7]) uses a Nitric Oxide (NO) molecular

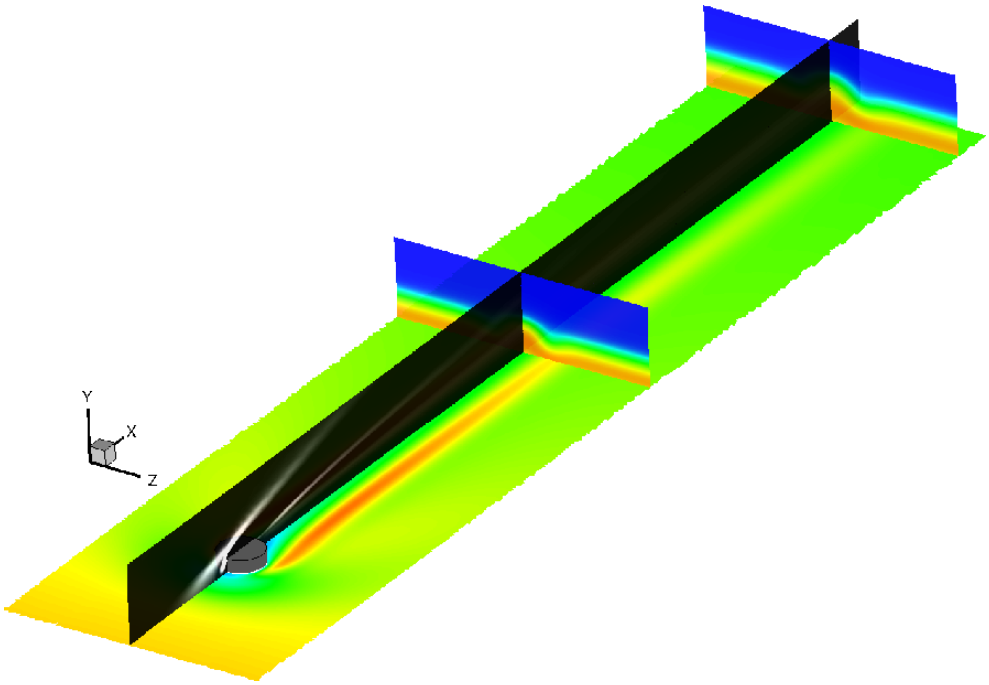

Figure 3.5: Instantaneous snapshot of the flow for cylindrical roughness element. Divergence contour shown in the symmetry plane, Temperature contour in the streamwise planes and streamwise velocity contour in the wall–parallel plane.

tagging velocimetry (MTV) technique to obtain averaged axial velocity. An interline, progressive scan CCD camera was used to obtain separate images of the initial reference and shifted NO molecules that had been tagged by the laser. Note that the center of the roughness is at $x = 7.54\ cm$. The error bars in the figure indicate experimental uncertainty as provided by Danehy [18].

The symmetry plane comparisons of the streamwise velocity profiles are shown in Figure 3.7. Streamwise stations varying from far upstream, close to the roughness and far downstream are shown in Figure 3.7. Except in the region very close to the roughness at $x = 7.22\ cm$ and $x = 7.86\ cm$, good agreement is observed with experiment, thus validating our algorithm. Upstream of the roughness element, at $x = 5.01\ cm$ and $x = 5.93\ cm$, the profiles resemble a 2D laminar boundary layer. At $x = 6.89\ cm$, the flow begins to separate indicated by a decrease in the velocity gradient at the wall. At $x = 7.22\ cm$, the flow has separated and the DNS velocity profile lies outside the range of

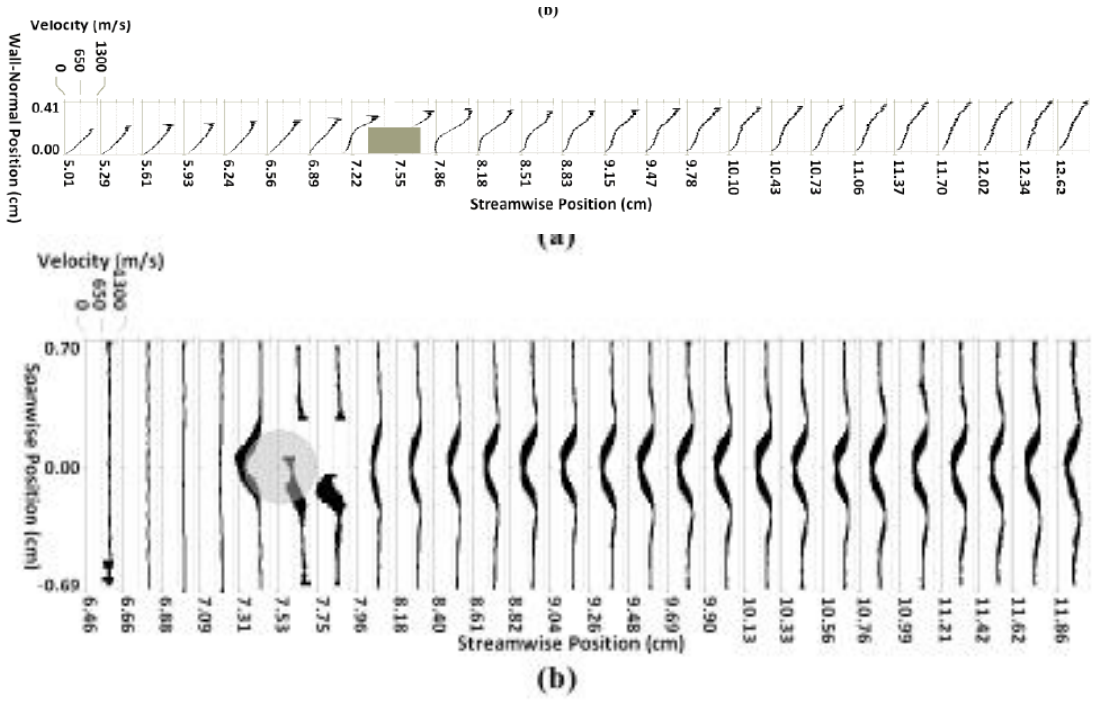

Figure 3.6: Figure showing the locations at which the velocity profiles were compared with the experiments of Bathel *et al.* [7] in the symmetry plane (top) and in a wall–parallel plane 2.1mm from the wall (bottom). Note that the roughness is present at 7.54 cm.

the reported uncertainty in the experiment. Note that the experimental velocity profile does not obey the no–slip condition at the wall at this station. Downstream of the roughness, at $x = 7.86$ cm, the velocity profile resembles a mixing layer, and while the experimental and computational profiles match close to the wall, they do not match beyond the height of the roughness element. Further downstream at $x = 9.15$ cm, 10.10 cm, 11.37 cm and 12.62 cm, good agreement is observed between computation and experiment. Note that the profile relaxes towards a laminar boundary layer profile at $x = 12.62$ cm.

Velocity profiles at a wall–normal plane 2.1 mm from the wall are compared to experiment at different streamwise locations in Figure 3.8. A difference of the order of 100 m/s is observed between the computed and experimental data upstream of the roughness. This difference could be attributed to the 0.5 mm uncertainty in the laser

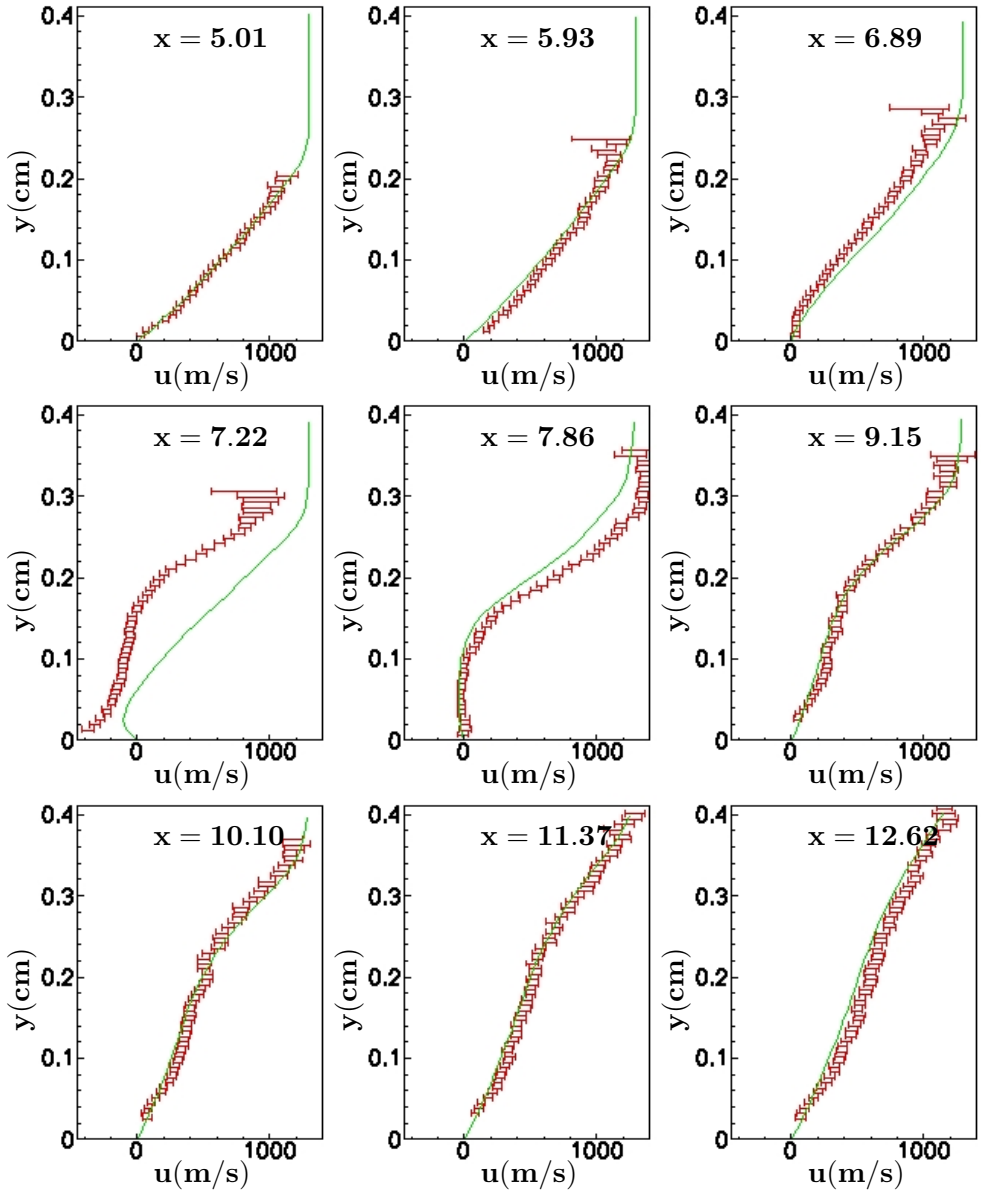

Figure 3.7: Symmetry plane streamwise velocity profile comparisons with experiments of Bathel *et al.* [7]. Solid green line : DNS, Symbols: Experiment.

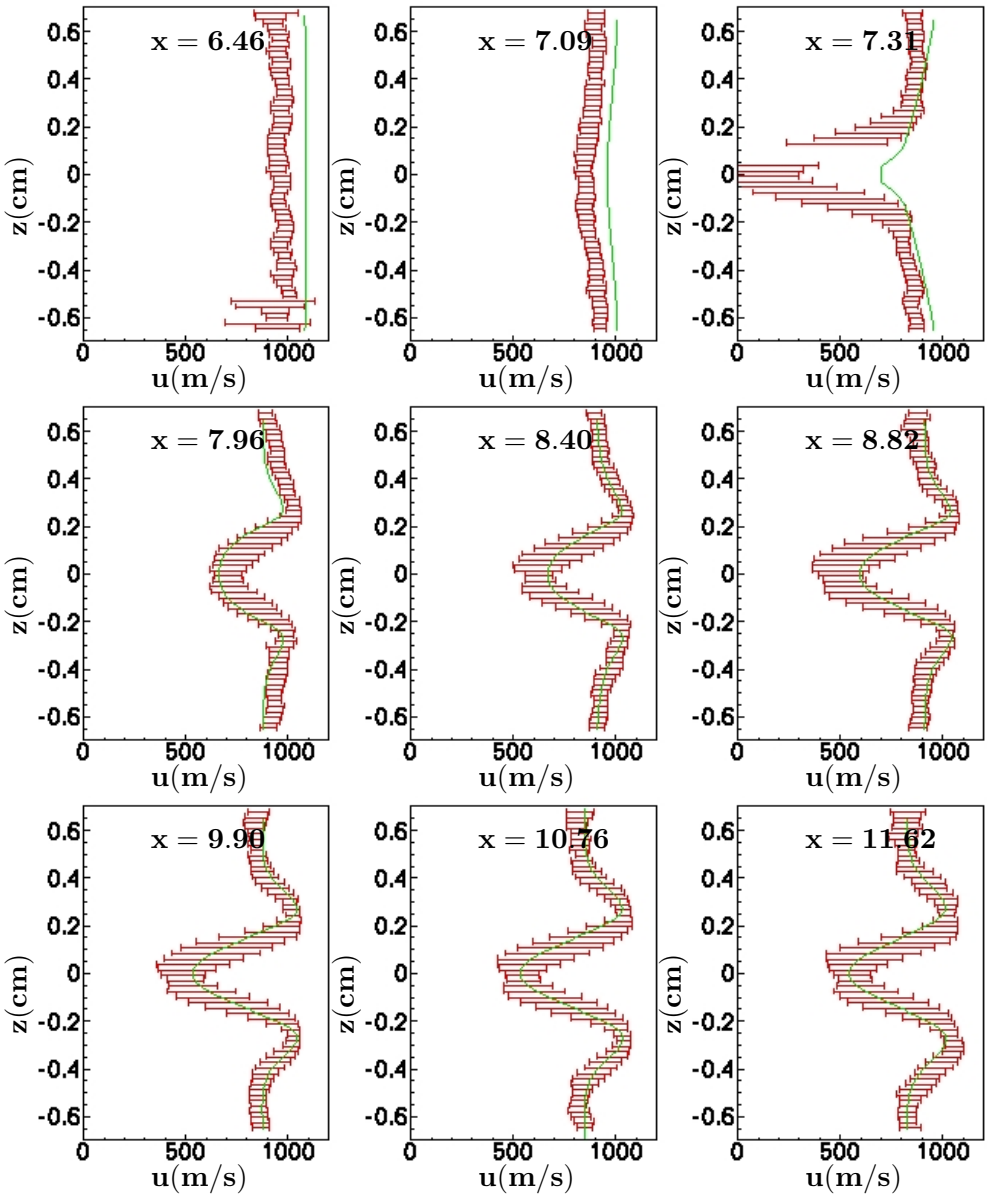

Figure 3.8: Wall-normal plane ($y = 2.1mm$) streamwise velocity profile comparisons with experiments of Bathel *et al.* [7]. Solid green line : DNS, Symbols: Experiment.

sheet position in the experiment (Danehy [18]). In the separation region upstream of the roughness, at $x = 7.31\ cm$, considerable difference is observed between computation and experiment. Downstream of the roughness, reasonable agreement is observed, with the computational profiles lying within the uncertainty bars of the experiment. The profiles downstream of the roughness can be seen to have a wake–type profile close to the symmetry plane with a peak on the either side due to the acceleration of the flow around the roughness.

From Figure 3.7, it was observed that in the symmetry plane comparisons, the agreement was good in locations away from the roughness element but in the separation and recirculation regions upstream and downstream of the roughness respectively, there was a mismatch. The NO-PLIF Molecular Tagging Velocimetry technique used by Bathel *et al.* [7] uses a 0.5 mm thick laser sheet. Once the NO molecules are tagged by the laser, an image is first taken by the camera after which another image is captured. The displacement of the tagged molecules is used to estimate the velocity of the fluid. The delay between the first and second images is 500 ns. The thickness of the laser sheet causes an uncertainty in the exact spanwise location (for symmetry plane profiles) at which the profile is being measured and the time delay could potentially be larger than required in some regions of the flow to accurately measure the velocity of the fluid. We use the data from our computations to estimate these two uncertainties for the flow condition under study.

3.3.3 Effect of time delay

The effect of time delay in measuring the velocity profiles in the symmetry and wall–normal planes is shown in Figure 3.9. A time delay of $\Delta t = 500\ ns$ was used. With the aim of quantifying the maximum possible difference due to the effect of time delay, we compare the experimental velocity profiles (with uncertainty bars) with the DNS results at x, $x + u_\infty \Delta t$ and $x - u_\infty \Delta t$. Although it would be ideal to use the local velocity at each streamwise location, we use u_∞ to report the maximum possible difference in the velocity profiles.

Since the maximum discrepancy between experiment and DNS occurs in the regions immediately upstream and downstream of the roughness element, the effect of time delay is reported at these locations in the symmetry and the $y = 2.1\ mm$ planes. In the

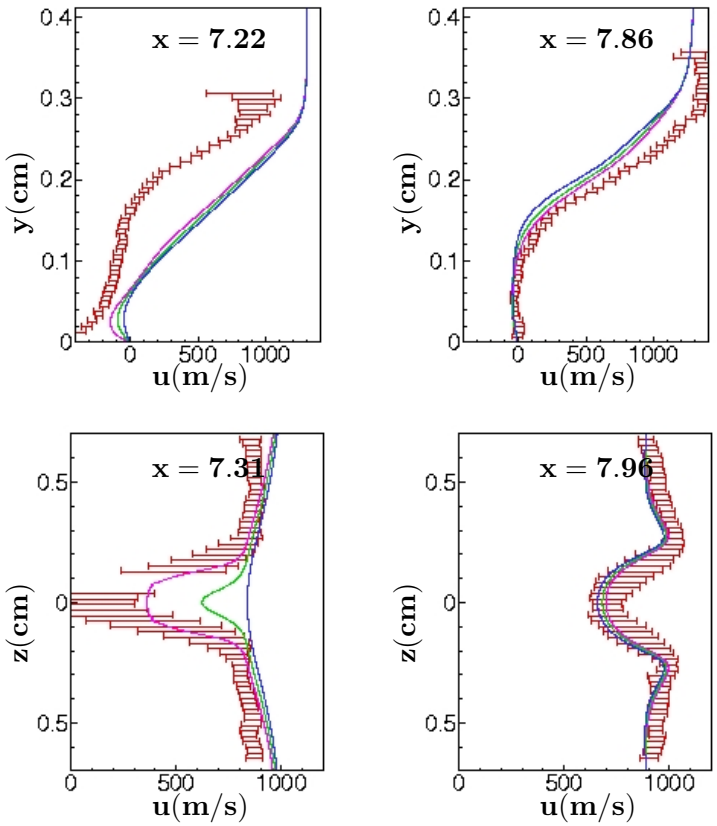

Figure 3.9: Effect of time delay on symmetry plane (top) and wall normal plane ($y = 2.1\ mm$) streamwise velocity profiles. Pink line: $x - u_\infty \Delta t$, Green line: x, Blue line: $x + u_\infty \Delta t$, Symbols: Experiment.

symmetry plane, at both $x = 7.22\ cm$ and $x = 7.86\ cm$ stations, the effect of time delay is negligible compared to difference observed between DNS and experiment. However, at $x = 7.31\ cm$, in the $y = 2.1\ mm$ plane, a significant difference is observed. It is seen that the DNS results at $x - u_\infty \Delta t$ agrees well with experiment indicating that the time delay is more than required to accurately measure the velocity profile at this station. However, downstream of the roughness, at $x = 7.96\ cm$, the difference is again negligible. Thus, the effect of time delay is prominent in the upstream separation region in the wall–parallel plane.

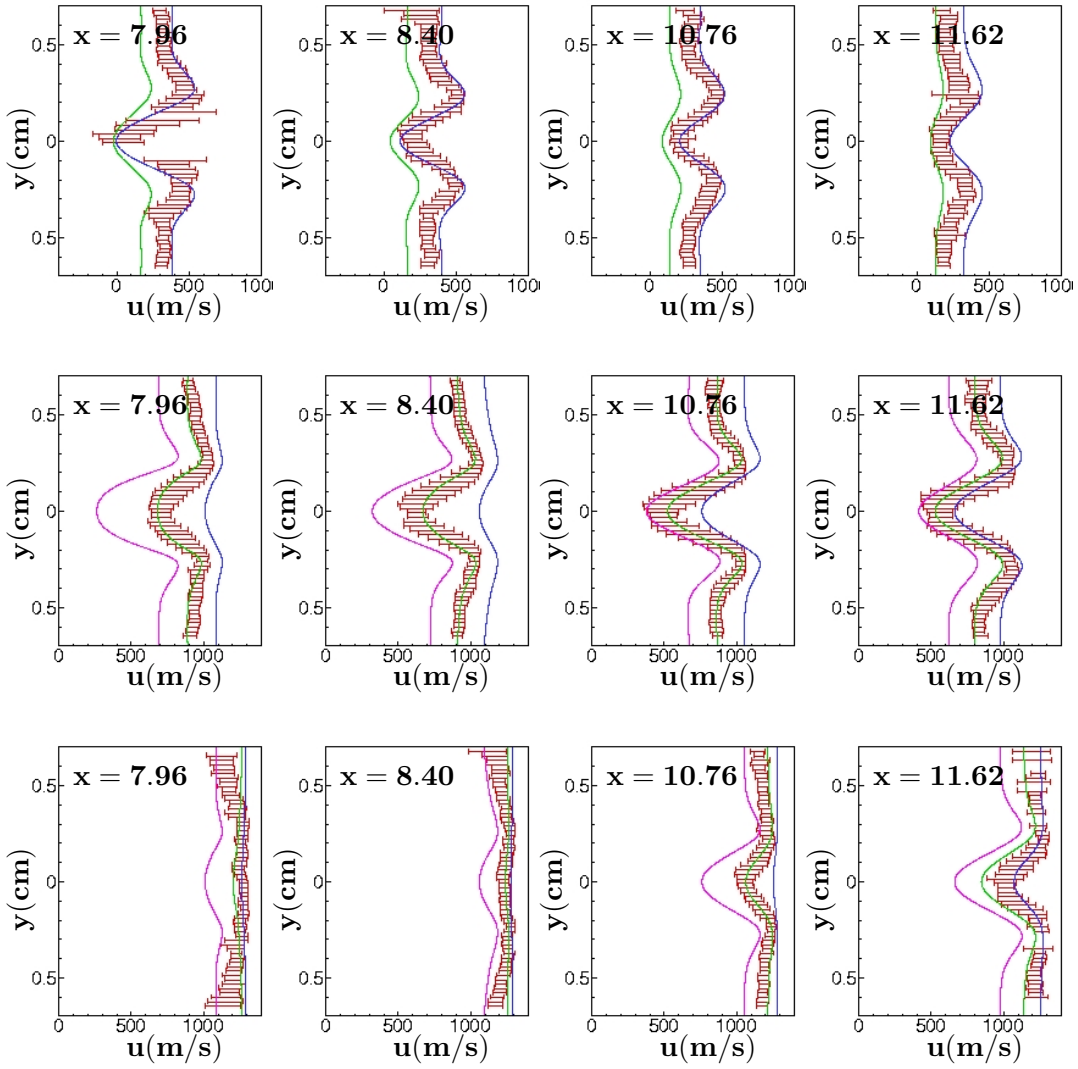

Figure 3.10: Effect of laser sheet position by $+/-0.5$ mm for y =0.3 mm (top), 2.1 mm (center) and 3.1 mm (bottom). Pink line: $y - 0.5mm$, Green line: y, Blue line: $y + 0.5mm$, Symbols: Experiment.

3.3.4 Effect of laser sheet position

To form a laser sheet in the experiment, a collimated 226 nm beam of Nd:YAG laser was passed through a cylindrical lens, which focused and then diverged the beam, expanding it in one direction while leaving it collimated in the other. A 1 m focal length spherical lens then collimated the diverging axis of the beam and focused the other axis into a thin sheet approximately 75 mm wide by 0.5 mm thick (Bathel *et al.* [7]). To account for the thickness in the laser sheet, we plot profiles at $y+/-$ 0.5 mm to see the variation in the velocity profiles.

Figure 3.10 shows the comparison of streamwise velocity profiles at y, $y+$ 0.5 mm and $y-$ 0.5 mm from DNS with those obtained from experiment in the $y = 0.3$, 2.1 and 3.1 mm planes. The stations downstream of the roughness element is reported at $x =$ 7.96, 8.40, 10.76 and 11.62 cm respectively. It can be observed that there is significant difference in the profiles between y, $y+$ 0.5 mm and $y-$ 0.5 mm. While the profiles at $y+$ 0.5 mm agree best with experiment at the $y = 0.3$ and 3.1 mm planes, those at y agree best with experiment at the $y = 2.1$ mm plane. As can be seen in Section 3.4, the injection of NO into the flow causes an increase in the boundary layer thickness downstream of injection, which can contribute to some of the differences between the experiment and DNS profiles in the wall–normal planes.

3.4 Effect of upstream injection for flow past cylinder

The velocity profiles were compared between computation and experiment in Section 3.3. While there was good agreement overall, there were some differences in the regions around the roughness. Since the experimental technique involves injecting NO molecules through a rectangular slot upstream of the roughness as shown in Figure 3.1, we examine the effects of injection under these flow conditions. We use air instead of NO as an approximation since there are no reaction or dissociation effects and since the properties of NO are not too different from that of air.

The temperature, pressure and velocity of the injection is exactly matched with the experiment, except that we use air in the computation instead of NO. The aim is to see by how much the flowfield is affected for the flowrate of NO injected and the regions in the flow that are most sensitive to the injection. The air is injected with a velocity

of 73 m/s, pressure of 400 Pa and density of 0.0048 kg/m3 through a rectangular slot whose dimensions and location match those of the experiment.

3.4.1 Flowfield description

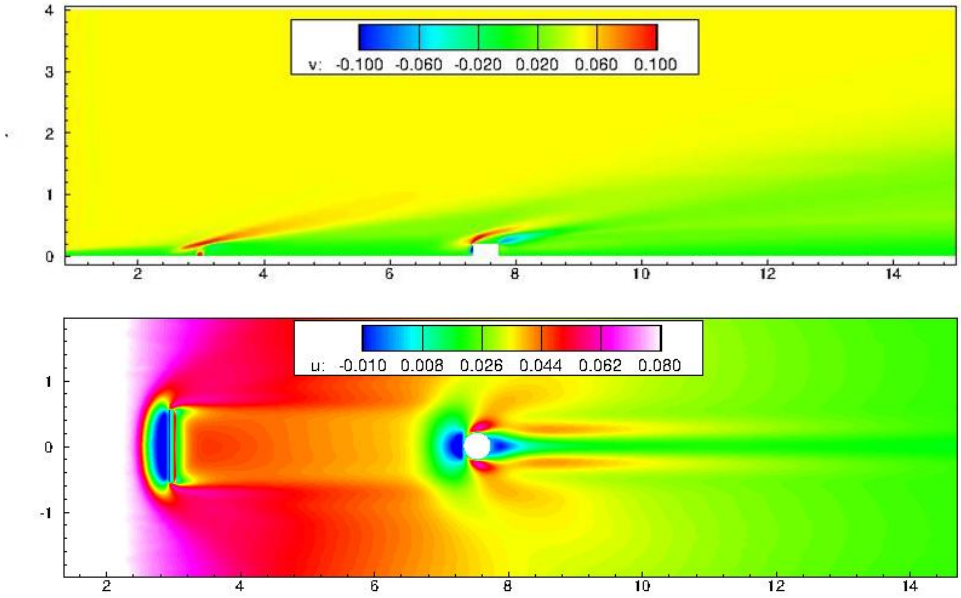

Figure 3.11: Instantaneous vertical (top) and streamwise (bottom) velocity contours in the symmetry plane and a wall–parallel plane respectively. The shock produced due to the injection and roughness is clearly visible in the symmetry plane.

Instantaneous vertical and streamwise velocity contours are shown in the symmetry and wall–parallel planes in Figure 3.11 for the flow past cylindrical roughness element with injection. The cylinder is placed at $x = 7.54\ cm$ in the figure with the rectangular injection slot centered at $x = 2.94\ cm$. A shock produced due to the injection in the symmetry is clearly visible. Also note that there is a slight increase in the boundary layer thickness downstream of the injection due to the vertical momentum of the injected air. Downstream of the injection slot, the flowfield qualitatively appears similar to the flow without injection due to the low velocity with which the air is injected in the slot ($v/u_\infty = 5.6\ \%$).

In the wall–parallel plane, the streamwise velocity in the region of the injection slot

is close to zero with the flow having to go around the slot jet creating a wake downstream of it. The signature of the wake, although small in magnitude (due to the scale at which the velocity is shown in the Figure), is visible until the separation region upstream of the roughness element. Downstream of the roughness element, high–speed streaks are observed as seen in the flow without injection due to the streamwise vortices created by the roughness element which transport higher momentum fluid towards the wall.

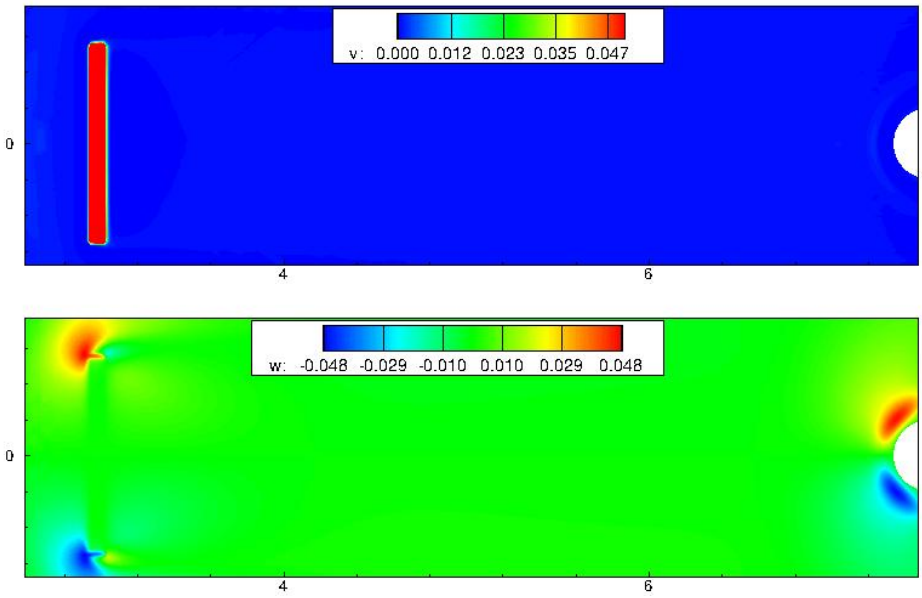

Figure 3.12: Instantaneous vertical (top) and spanwise (bottom) velocity contours in a wall–parallel plane. The injection slot is clearly visible.

Figure 3.12 shows the instantaneous vertical and spanwise velocity contours to clearly depict the injection slot upstream of the roughness. The spanwise velocity contours indicate that there is some three–dimensionality introduced due to the slot injection, whose magnitude is highest at the sideward edges of the slot. Closer to the symmetry plane, the flow appears to be two–dimensional with decreasing effect of the slot as we move downstream of it.

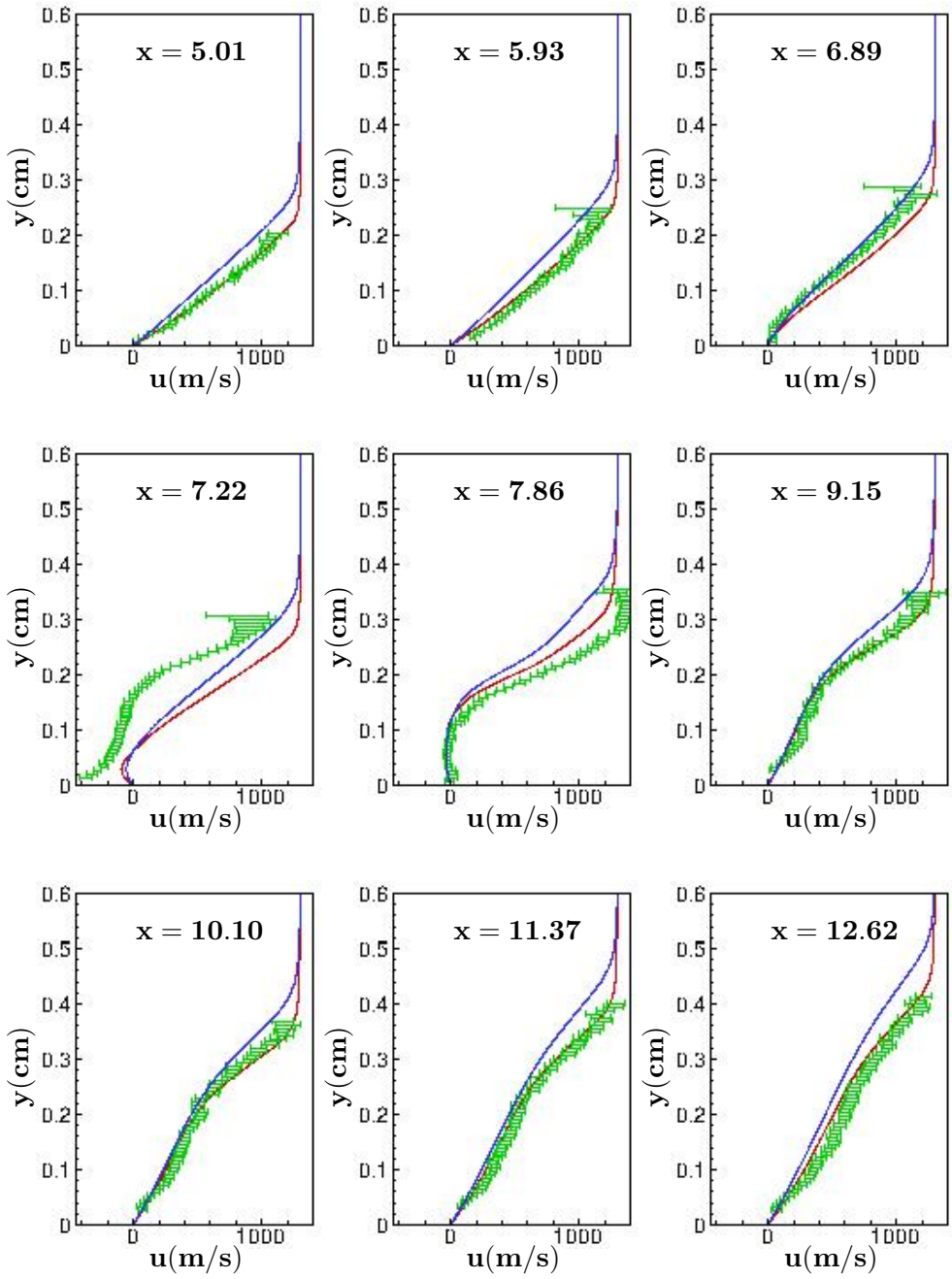

Figure 3.13: Symmetry plane streamwise velocity plane comparisons with and without injection with the experiments of Bathel *et al.* [7]. Red line: DNS without injection, Blue line: DNS with injection, Symbols: Experiment.

3.4.2 Unscaled Velocity profile comparisons

Figure 3.13 compares the streamwise velocity profiles obtained with and without injection along with symbols from the experiment in the symmetry plane at the same streamwise stations as Figure 3.7. Locations upstream, near and downstream of the roughness element is shown. It can be seen that for the flow with upstream injection, the boundary layer thickness increase is significant and hence the profiles with injection do not match well with experiment. At most stations, the flow without injection matches well with experiment but the profiles obtained with injection do not match owing to the increase in the boundary layer thickness. The velocity profiles with injection are very similar in shape to the those without injection with the exception of the boundary layer thickness being different. To check whether the boundary layer thickness prescribed at the inflow of the simulation with injection is consistent with the simulation without injection, we compare the stations upstream of the roughness in the following Section.

3.4.3 Upstream boundary layer thickness comparison

Figure 3.14 shows the comparison of streamwise velocity profiles with and without injection in the symmetry plane. Two profiles upstream, and two downstream of the roughness are shown. It can be seen that the upstream injection causes a significant increase in the boundary layer thickness as can be observed from all the locations in Figure 3.13. To confirm that the laminar boundary layer thickness at the inflow of the computational domain was prescribed correctly, we compare the velocity profiles at z =4 cm for the injection case (which is far away from the injection slot) with the symmetry plane profiles for the no injection case in Figure 3.14.

At x =5.01 cm and 5.93 cm which is upstream of the roughness element, we see that the profiles with and without injection match well indicating that the laminar boundary layer thickness at the inflow of the computational domain was prescribed correctly. It should be noted that the injection is prescribed as a steady boundary condition in the simulation which neglects the effects of the boundary layer flow on the injection. Also, viscous effects of the injection slot are are neglected since a constant injection velocity is prescribed over the entire injection slot. These two factors could potentially contribute to some differences in the boundary layer thickness observed with and without injection,

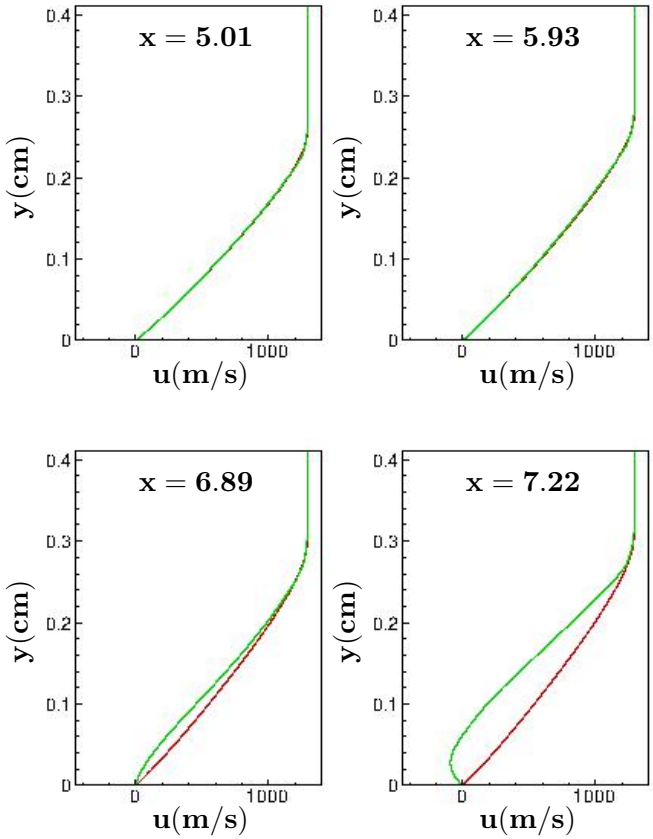

Figure 3.14: Comparison of velocity profiles with upstream injection at z =40 mm (solid red line) to velocity profiles without upstream injection (solid green line) along the symmetry plane.

although it is reasonable to expect that the boundary layer thickness would increase due to the injection.

3.4.4 Scaled velocity profile comparisons

Since Figure 3.13 showed that the upstream injection causes a significant increase in the boundary layer thickness of the flow, we compare the velocity profiles with the wall–normal co-ordinate (y) scaled with the local boundary layer thickness (δ, computed at the location where $u = 99\%$ of the free–stream value) in Figure 3.15. Overall, we observe that the match between the profiles with and without injection is excellent, indicating that the effect of upstream injection on the flow-field is negligible when the wall-normal

co-ordinate is scaled with the boundary layer thickness .

Therefore, comparison of velocity profiles with experiments would be more meaningful if the wall-normal co-ordinate is scaled with the boundary layer thickness. This could also be a factor in the mismatch of the velocity profiles in the wall-parallel planes at some locations between the experiment and simulation in Figure 3.8, especially at $x = 6.46\ cm$ and $x = 7.09\ cm$.

3.5 Conclusions

A DNS of a Mach 8.12 boundary layer flow past a cylindrical roughness element was performed matching the conditions of Bathel *et al.* [7]. The flow remained laminar and did not transition. The steady streamwise velocity profiles were compared to the experiments of Bathel *et al.* [7] in the symmetry and wall–normal planes, and overall, good agreement was observed. However, in the regions just upstream and downstream of the roughness, some mismatch between DNS and experiments were observed. The DNS was used to quantify possible uncertainties associated with the NO-PLIF Molecular Tagging Velocimetry (MTV) technique. The effect of time delay between two snapshots in the experiment, laser sheet thickness and upstream injection was quantified. It was seen that the effect of time delay was significant in the wall–normal plane but not in the symmetry plane. The laser sheet position had a significant effect on the wall–normal plane profiles. A separate simulation with upstream injection with air under the same conditions as the NO injection was carried out to quantify its effects. It was found that the upstream injection causes an increase in the boundary layer thickness and thus, if the profiles were scaled with the local boundary layer thickness at each station, the effect of the injection was negligible.

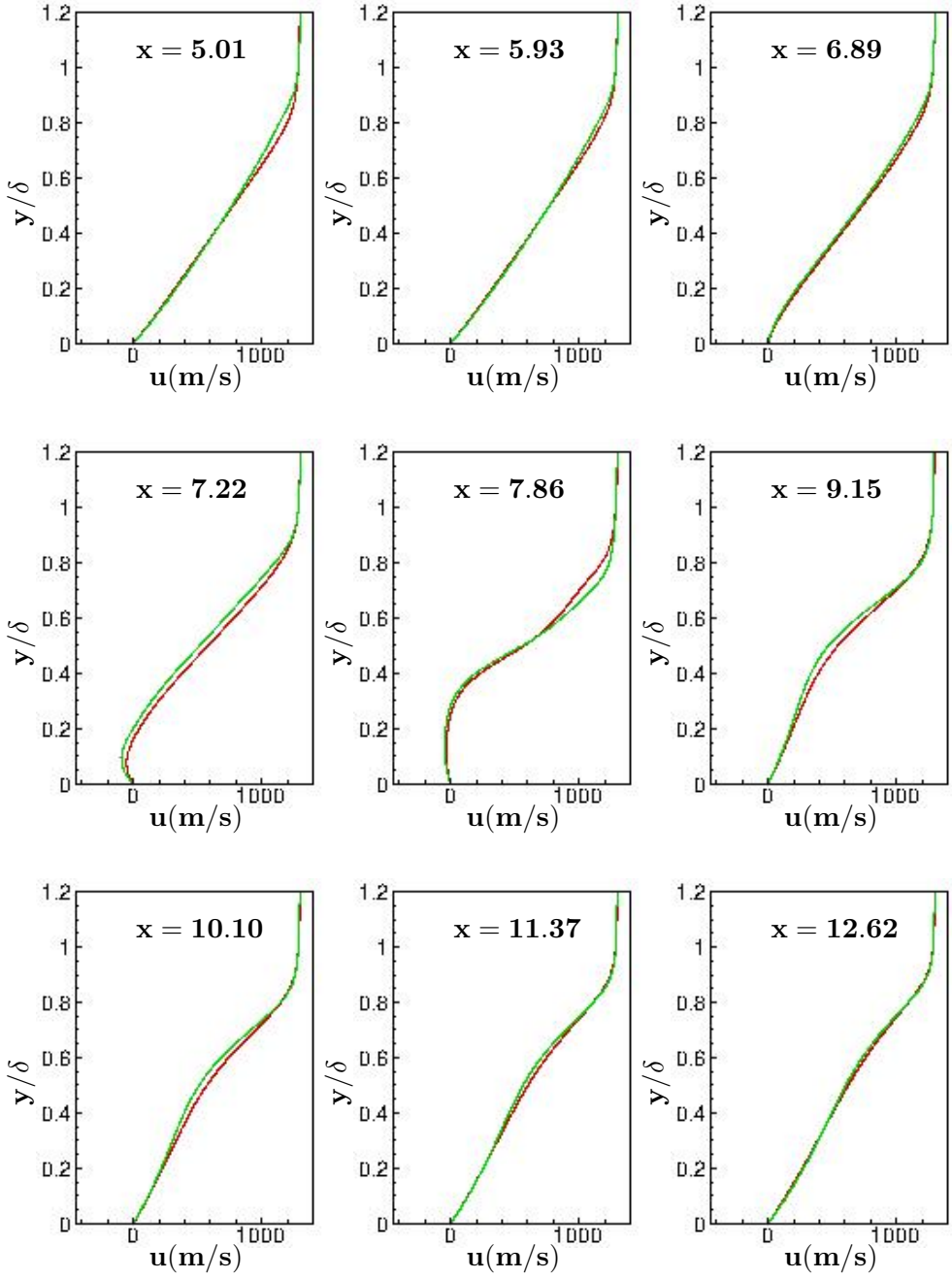

Figure 3.15: Symmetry plane streamwise velocity profiles with (solid red lines) and without (solid green lines) upstream air injection. Profiles are scaled by the local boundary layer thickness (δ) at the respective streamwise x-locations.

Chapter 4

Flow past a hemispherical roughness element

4.1 Problem Description

Flow past a hemispherical bump placed on a flat plate is simulated at conditions that match the experiments of Danehy et al. (2009). The experimental setup consists of a wedge placed at different angles to an incoming Mach 10 flow at 51.32K with unit Reynolds number Re=6 million/m. A hemispherical roughness element of 4 mm diameter (denoted by D) is placed on the top surface of the wedge at a distance of 75.4 mm (18.85D) from the leading edge of the wedge. The top surface of the wedge is 157.2 mm (39.3D) long and 127 mm (31.75D) wide. A shock wave forms at the leading edge of the wedge and post-shock conditions yield the free–stream conditions for the top surface of the wedge (and the roughness element).

The wedge was placed at different angles to the Mach 10 flow to yield different free–stream conditions. Three such conditions are simulated and are listed in Table 4.1. In addition to free–stream density, velocity and temperature, Table 4.1 also lists the free–stream Mach number, k/δ and roughness Reynolds number ($Re_k = u_\infty k/\nu_\infty$) computed based on free–stream properties and the height of the roughness ($k = D/2 = 2$ mm). Here δ is the boundary layer thickness at the location of the roughness if it were absent. The wall is maintained at a constant temperature of 300K, and T_w/T_{aw} is roughly constant for all cases at 0.3 since the wall temperature and the stagnation temperature

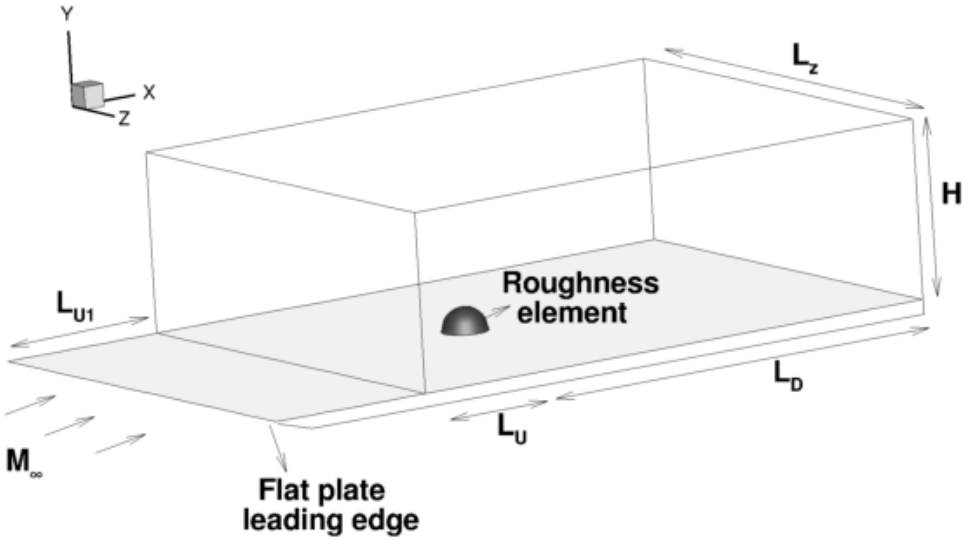

Figure 4.1: Schematic of the problem showing the different roughness elements used in this study. The box depicts the computational domain where a compressible similarity solution is prescribed at the inflow.

of the wind tunnel facility is maintained constant for all cases. Here T_{aw} is the adiabatic wall temperature computed using the following relation: $T_{aw} = T_\infty(1+0.5r(\gamma-1)M_\infty^2)$ where r is the recovery factor taken to be 0.85.

The simulations model the post-shock flow over the top surface of the wedge as flow over a flat plate. The flow conditions upstream of the wedge were obtained from Danehy et al. (2009), and post-shock conditions obtained from the Rankine–Hugoniot equations were specified as free-stream conditions for the flat plate. The compressible Navier–Stokes equations are solved in non–dimensional form as follows:

$$\rho = \rho^*/\rho^*_\infty \quad u = u^*/u^*_\infty \quad T = T^*/T^*_\infty \quad p = p^*/\rho^*_\infty u^{*2}_\infty \quad x_i = x^*_i/D \quad t = t^* u_\infty/D, \tag{4.1}$$

where the superscript (*) denotes dimensional values.

A schematic of the computational domain is shown in Figure 4.1. The inflow of the computational domain is at a distance of 8.85D from the leading edge of the flat plate. A compressible boundary layer similarity solution is prescribed at the inflow domain to yield the experimental boundary layer thickness at the location of the roughness if it were absent. Distances L_U, L_D, L_z and

H are defined shown in Figure 4. Three grids were used for this study which are described in Section 4.2. L_U=10D for all the cases, and L_D=40D. The height of the domain (H) is 10D for the coarser grids and 6D for the fine grid while L_z=40D for the coarser grids and 20D for the fine grid.

M_∞	$u_\infty(m/s)$	$\rho_\infty(Kg/m^3)$	$T_\infty(K)$	k/δ	Re_k	Re_θ
3.37	1217.57	0.0786	340.48	2.54	9121	375.59
5.26	1344.85	0.0647	162.90	2.08	14190	447.80
8.23	1409.86	0.0328	73.12	1.19	16831	493.42

Table 4.1: Table listing the simulation parameters for flow past a hemispherical roughness element.

Figure 4.2 illustrates the instantaneous flow features for the Mach 3.37 flow. Density gradient contours are shown in the symmetry and streamwise planes to depict the shock while streamwise vorticity (ω_x) is shown in the plane parallel to the flat plate. Far upstream the flow is laminar while unsteady flow features can be observed downstream of the roughness. The unsteady region spreads in the span with increasing downstream distance from the roughness. Note the system of shocks produced due to the roughness. The separation shock is produced when the supersonic inflow comes in contact with the separated low-speed fluid. The roughness element produces a shock which is strongest of the system of shocks formed followed by the reattachment shock formed due to the compression of the fluid reattaching the flat plate downstream of the roughness. The three-dimensional nature of the shock is visible in the streamwise plane closest to the roughness. Far downstream, the small scale vortical structures are indicative of a turbulent flow.

4.2 Grid parameters

Three different grids were used in this study which are referred to as 'coarse', 'medium' and 'fine' in this section. The coarse and medium grids were refined in the vicinity of the bump with increasing Δx spacing towards the outflow. In the finest grid, Δx spacing was maintained constant throughout the region downstream of the roughness

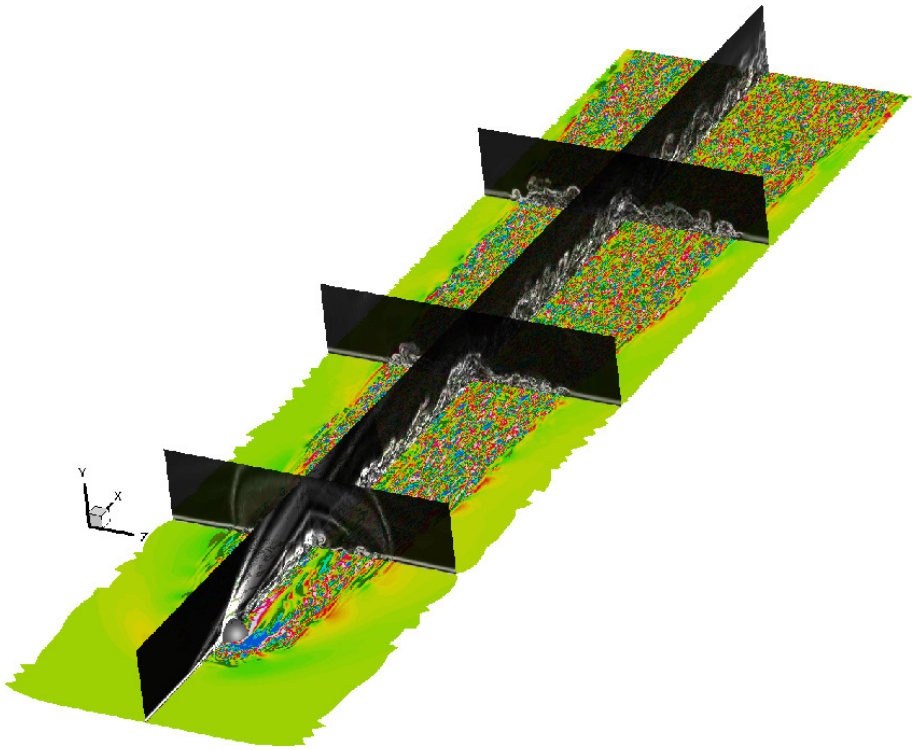

Figure 4.2: An instantaneous snapshot of the flow for Mach 3.37. Density gradient contours are shown in the symmetry and streamwise planes to show the shocks and vortices. Streamwise vorticity contours are shown in the y =0.05 plane showing small scale features of the flow far downstream.

to capture the turbulent region. Since the Mach 8.23 boundary layer did not undergo transition, a relatively coarse grid of 16 million was used. For the Mach 3.37 and 5.26 simulations, the mesh spacings were chosen based on the coarse grid results so as to maintain Δx^+ =15, Δy^+_{min} =0.6 (Δy^+_{cv} =0.3) and Δz^+ =10 for the finest grid in the region downstream of the roughness. The viscous spacings of Δx^+ =15 and Δz^+ =10 corresponds to Δx =0.02 and Δz =0.0133 for M_∞ =3.37 and Δx =0.04 and Δz =0.0266 for M_∞ =5.26 respectively. The grid is finer in the vicinity of the roughness with more than 240 points on the surface of the roughness in the y =0 plane for all the three grids used.

The symmetry and wall-parallel planes of the grid in the vicinity of the roughness are shown in Figures 4.3 and 4.4. Note that the region near the roughness element

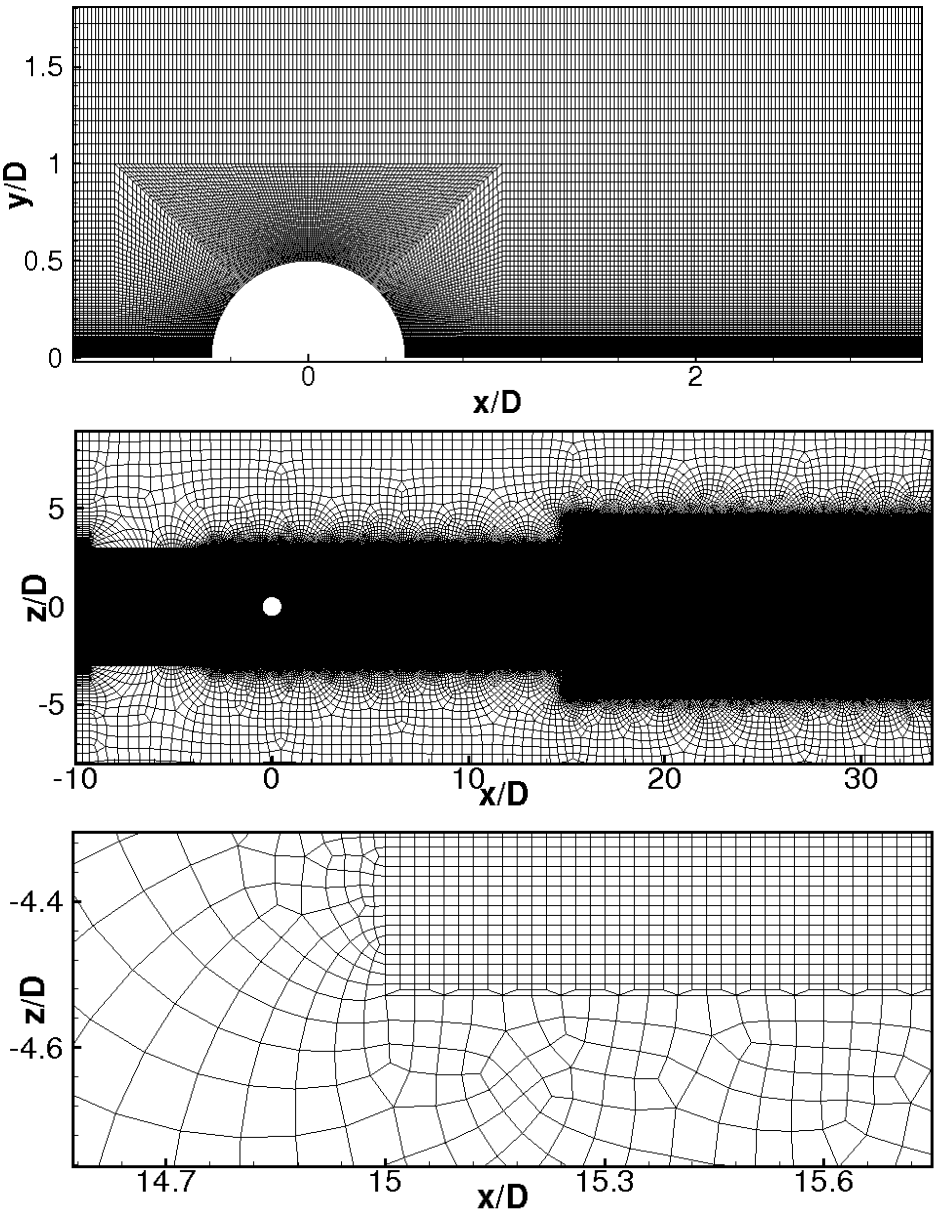

Figure 4.3: Symmetry and wall-parallel planes showing grid used in hemispherical bump simulation. Note that the grid is refined in the region where the flow is transitional and is coarse where the flow remains laminar.

is much finer than the surrounding regions. Since the transitional/turbulent region generated due to the roughness is confined within a certain span, Δz quickly coarsens outside the wake of the roughness (Figure 4.3). The finest grid for Mach 3.37 contained approximately 154 million elements and the same for Mach 5.26 contained 40 million elements. The number of grid points in the y-direction for M_∞ =3.37 is shown in Figure 4.5. Note that the fine grid contains 70 points within the height of the roughness.

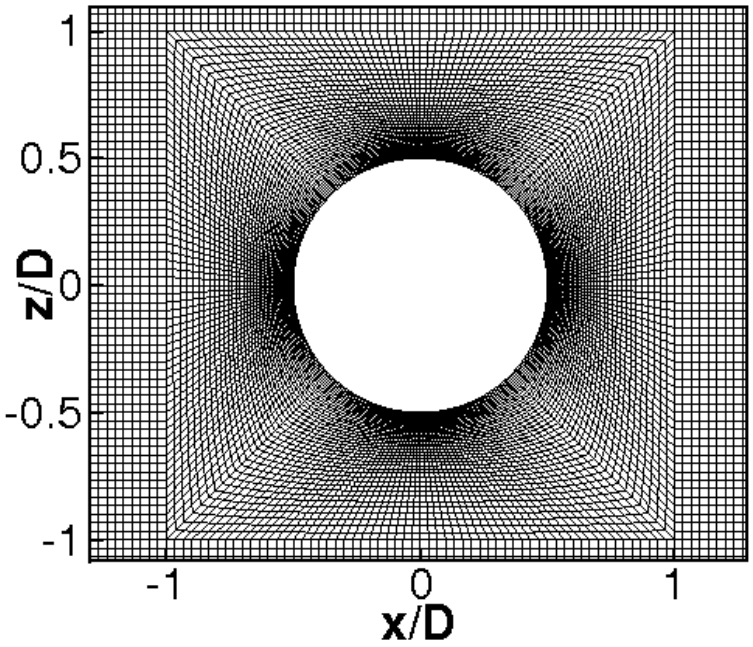

Figure 4.4: Figure showing the number of grid points in the y-direction for the three grids used for M_∞ =3.37.

4.3 Grid convergence study

All the mean statistics reported in this paper have been checked for statistical convergence using over 20000 samples spanning more than 160 D/u_∞ time units (where one domain flow through time is 50 D/u_∞). We first describe the grid spacings for M_∞ = 3.37 in the region downstream of the roughness to show how the fine grid resolution was arrived at. Δz was 0.0133, 0.033 and 0.066 and Δy_{min} was 0.0008, 0.001 and 0.01 for the fine, medium and coarse grids respectively. At $x = 5$, Δx was 0.02, 0.049 and

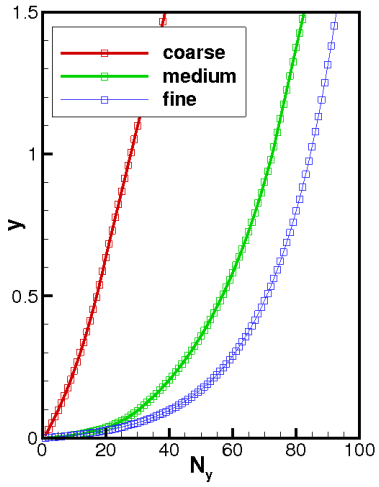

Figure 4.5: Figure showing the number of grid points in the y-direction for the three grids used for M_∞ =3.37.

0.07 for the fine, medium and coarse grids while at $x = 15$, it was 0.02, 0.09 and 0.11 respectively. We have attached the effect of grid resolution at x =5, 15 and 25 and $z = 0$ and 1 in Figures 4.6–4.7. The results indicate that the variation of the solution with the different grids is small indicating grid convergence. The differences between the grids is more prominent in the $TKE = \overline{u_i' u_i'}$ profiles when compared to u and ρ.

Figure 4.8 shows the streamwise velocity contours for the three grids in the $y = 0.05$ plane to depict the small scales captured by the grids. Note that the difference in length scales captured by the medium to coarse grids is more prominent when compared to that captured by the fine to medium grids. The difference between the grids is more prominent in the Van-driest transformed velocity (defined in Section 4.5) in Figure 4.9 where the coarse grid is clearly inadequate owing to its coarse Δy^+_{min} resolution while the the agreement between the finer grids is good.

4.4 Qualitative comparison to experiment

Figure 4.10 shows the experimental PLIF images from Danehy *et al.* [19] and instantaneous vorticity magnitude contours in the symmetry plane from the computations. Note that the lower Mach number boundary layers undergo transition, while the Mach 8.23

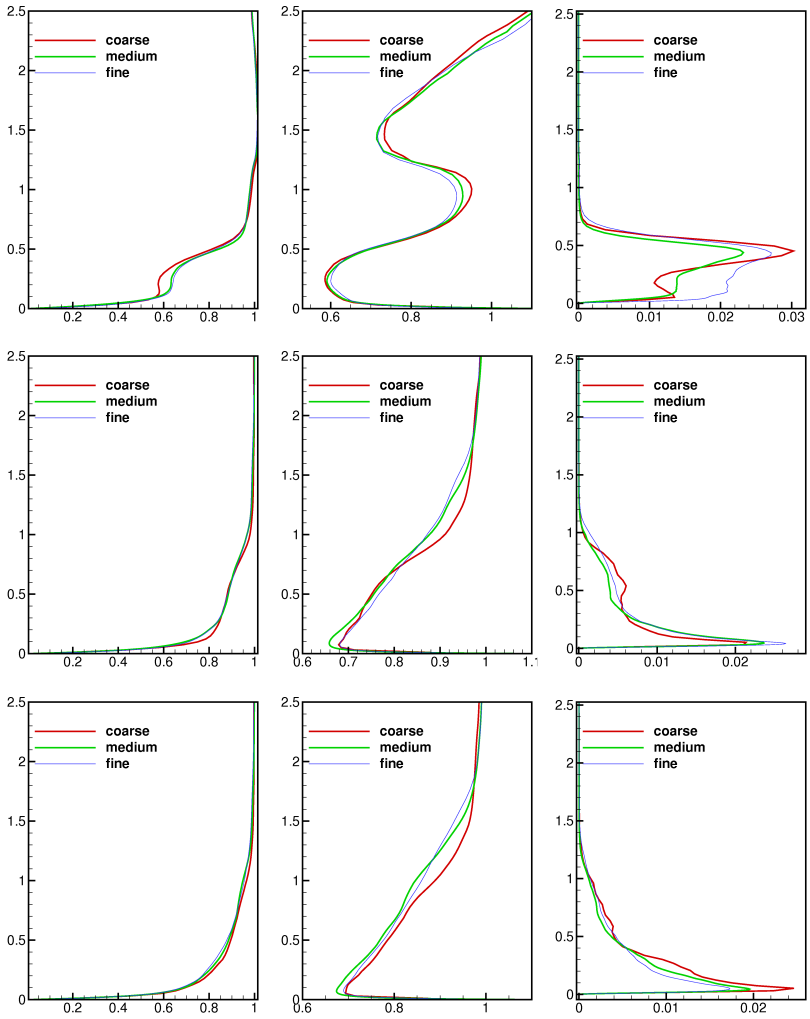

Figure 4.6: Profiles of mean streamwise velocity ($\overline{u}$), density ($\overline{\rho}$) and turbulent kinetic energy ($TKE = \overline{u_i' u_i'}$) with y at three streamwise stations: x =5 (top row), x =15 (middle row) and x =25 (bottom row) in the symmetry plane (z =0) are shown for M_∞ =3.37.

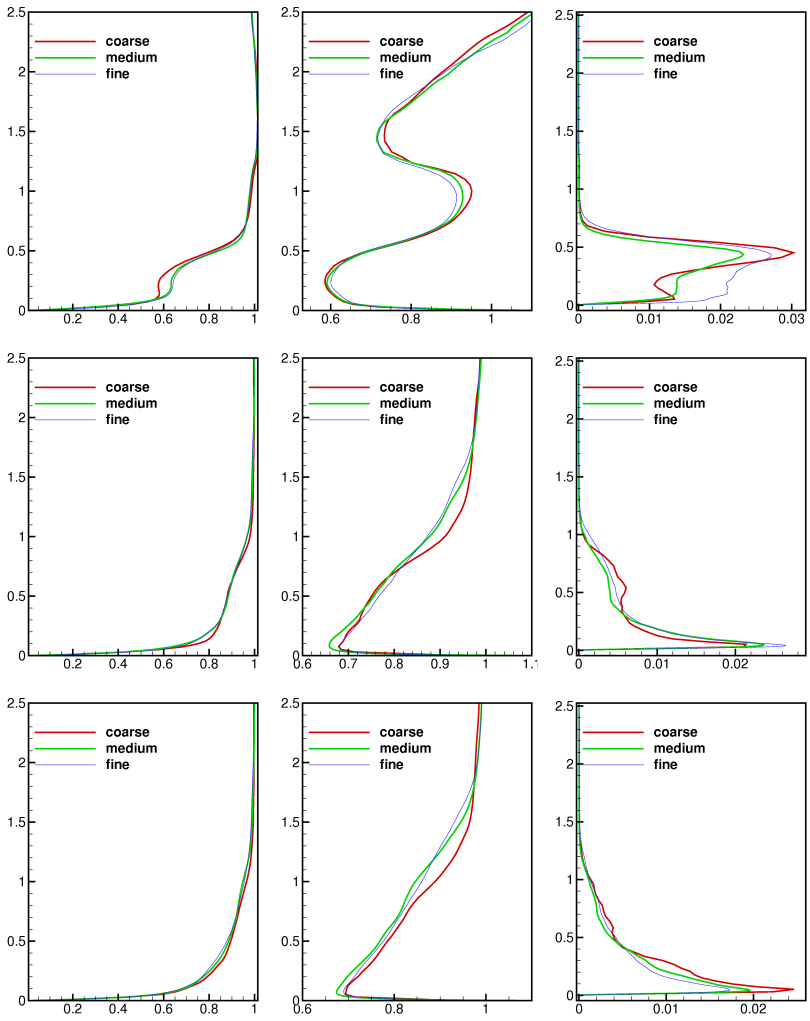

Figure 4.7: Results from grid convergence study. Profiles of mean streamwise velocity ($\overline{u}$), density ($\overline{\rho}$) and turbulent kinetic energy ($TKE = \overline{u_i' u_i'}$) with y at three streamwise stations: x =5 (top row), x =15 (middle row) and x =25 (bottom row) in the z =1 plane are shown for M_∞ =3.37.

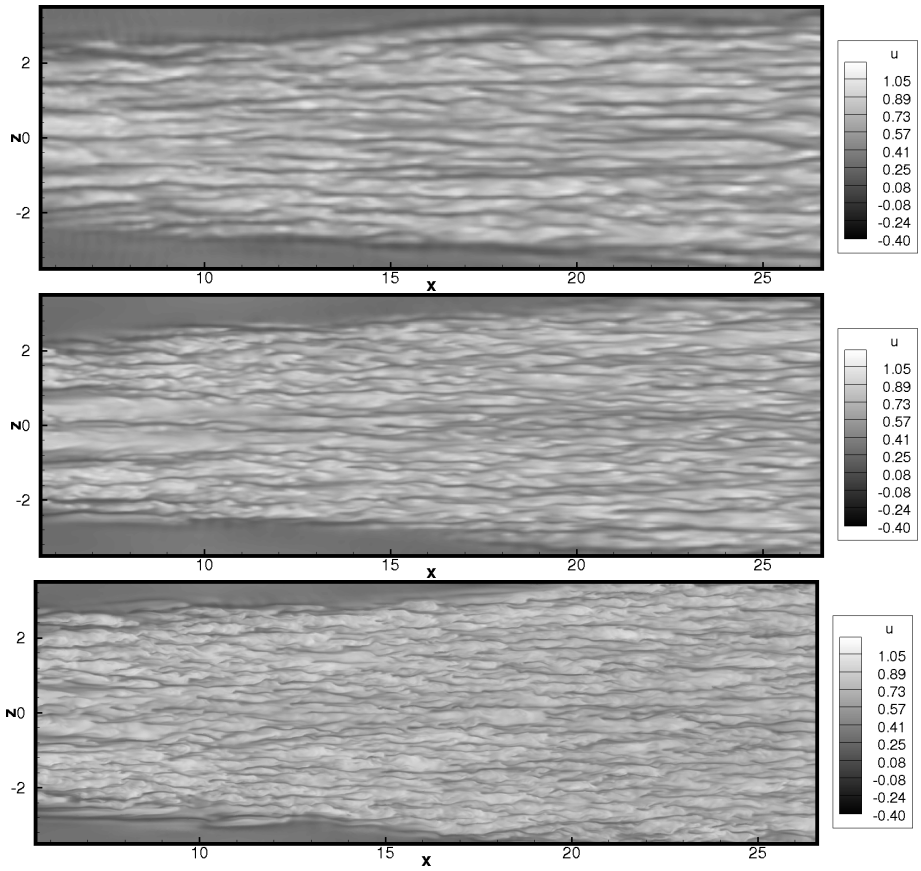

Figure 4.8: Streamwise velocity contours at $y = 0.05$ showing the effect of grid resolution for the coarse (top), medium (center) and fine (bottom) grids.

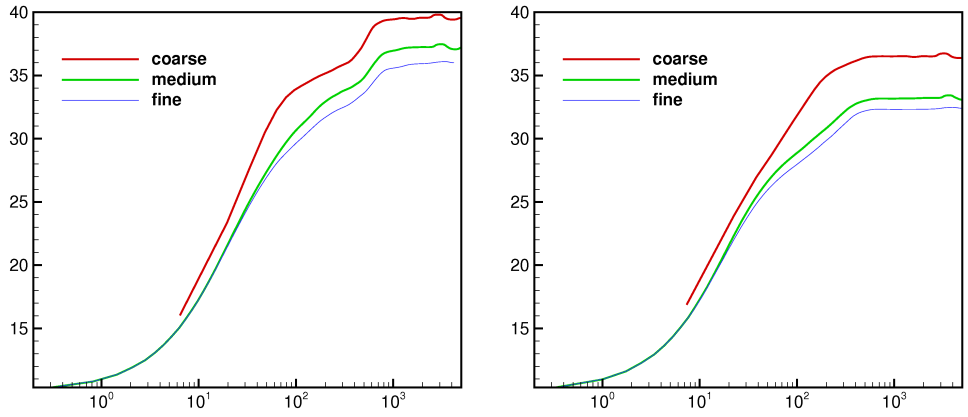

Figure 4.9: Effect of grid resolution on Van-driest transformed velocity at $x = 15$ and $z = 0$ (left) and 1 (right) for $M_\infty = 3.37$.

flow remains laminar downstream of the roughness. Also the Mach 3.37 flow undergoes transition closer to the bump when compared to Mach 5.23. This trend is consistent between the experiment and our computation thereby serving as a qualitative validation of the nature of flowfield downstream of the roughness. Note that the experimental and simulation figures are not exactly to scale although the downstream distance of the two are matched. The upstream boundary layer is thinnest for the lowest Mach number and hence if the boundary layer thickness is taken as the relevant length scale, the bump is tallest for Mach 3.37. It is known in incompressible flows (Tani [61]) that a larger roughness height (Re_k) moves the transition location closer to roughness and the observations made here are consistent for Mach 3.37 and 5.26. It has been observed that in general, higher Mach numbers stabilize the flow as seen by Danehy *et al.*[19, 20] and Chang & Choudhari [12], and this trend is consistent with the present observations.

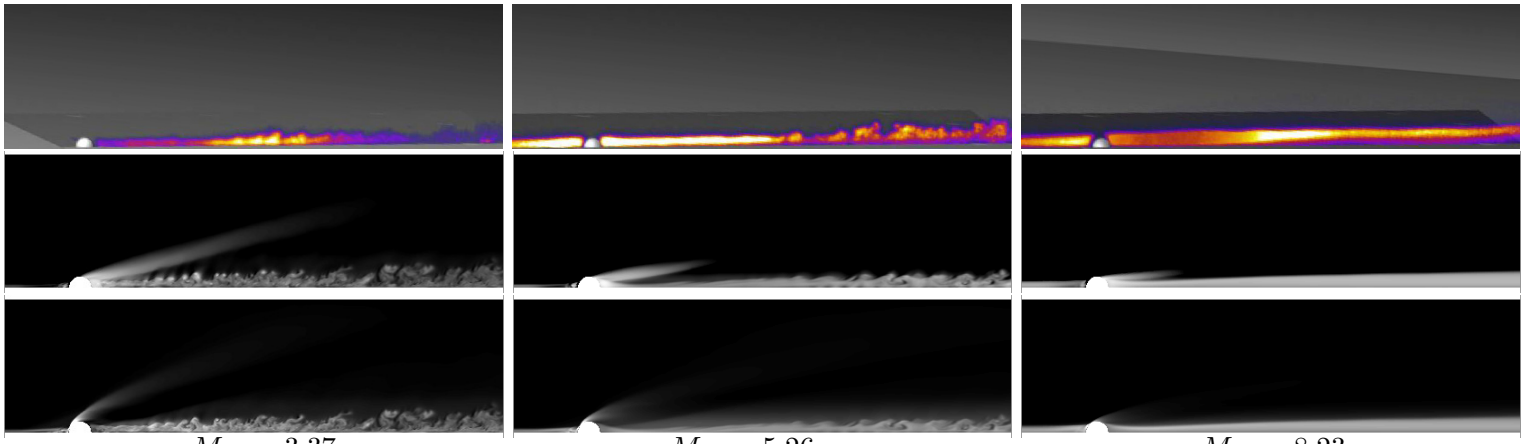

$M_\infty = 3.37$ $M_\infty = 5.26$ $M_\infty = 8.23$

Figure 4.10: Experimental NO-PLIF images from Danehy *et al.* [19] (top) with instantaneous density (center) and temperature (bottom) contours from simulation for M_∞ =3.37, 5.26 and 8.23 respectively.

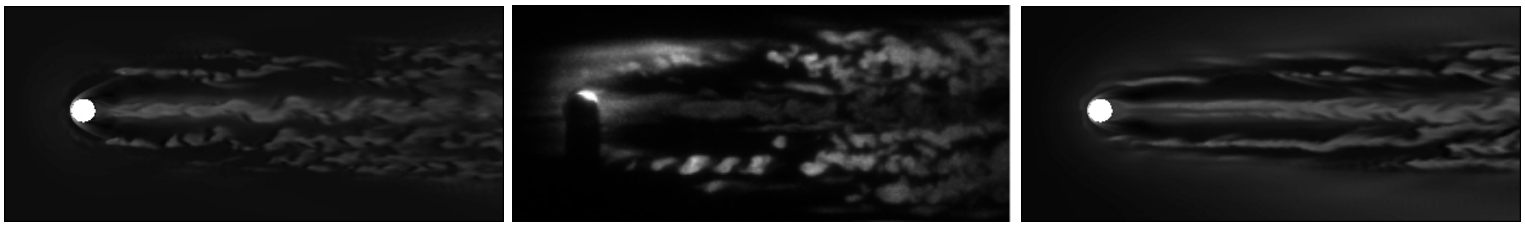

$M_\infty = 3.37$, DNS $M_\infty = 4.23$, PLIF $M_\infty = 5.26$, DNS

Figure 4.11: Instantaneous temperature contours from simulation for Mach 3.37 (left) and Mach 5.26 (right) compared with PLIF image for Mach 4.23 from Danehy *et al.* [19] for qualitative purposes.

4.5 Results

The results of the hemispherical bump simulations are discussed. Section 4.5.1 discusses the nature of the upstream separation induced by the roughness. Section 4.5.2 considers the formation of counter-rotating streamwise vortices downstream of the roughness; their perturbation of the separation shear layer is discussed in Section 4.5.3. The various sources of unsteadiness that might induce transition are identified in Section 4.5.4. Section 4.5.5 illustrates the formation of hairpin vortices behind the roughness. The dominant frequencies in the flow for Mach 3.37 are discussed in Section 4.5.6 and the mean flow is quantified in Section 4.5.7. Finally, a local Reynolds number indicative of the trend of transition is computed in Section 4.5.8.

4.5.1 Upstream separation

A laminar boundary layer undergoes three-dimensional separation upstream of a roughness element in its path. This separation results in the concentration of vorticity from the boundary layer into discrete spanwise vortices. This phenomenon has been observed by various researchers including Baker [3] and Simpson [59]. The number of vortices depends on the Mach number, Reynolds number and the height of the roughness. For incompressible flow past a cylinder placed on a flat plate, Baker [3] presents a chart showing the effect of D/δ^* (where δ^* is the displacement thickness) and Re_D on the number of vortices formed upstream. Higher values of Re_D and D/δ^* were likely to produce an unsteady six-vortex system while lower values were likely to produce steady six, four or two-vortex systems respectively.

M_∞	$Re_D = \frac{u_\infty D}{\nu_\infty}$	D/δ^*	No. of vortices
3.37	18241	11.51	6 (highly unsteady)
5.26	28378	6.44	6
8.23	33662	2.92	4

Table 4.2: Table showing parameters describing upstream separation.

Table 4.2 lists the flow parameters and number of vortices observed in our simulations. Figure 4.12 shows the vortex system upstream of the roughness. A six-vortex

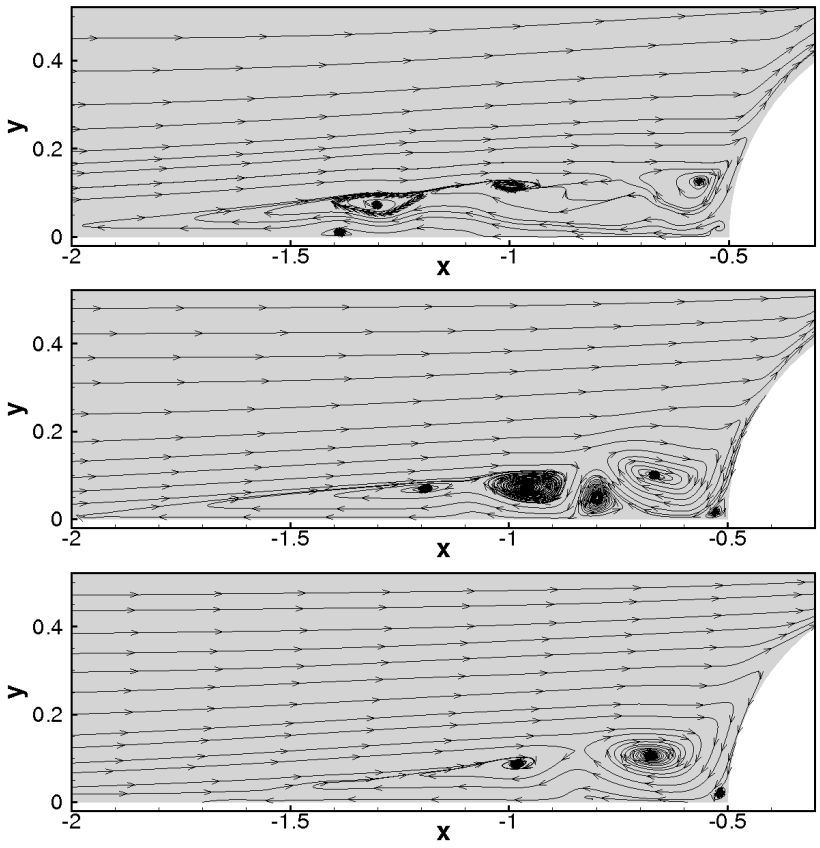

Figure 4.12: Figure showing instantaneous streamlines for Mach 3.37 (top-left), Mach 5.26 (top-right) and Mach 8.23 (bottom) indicating the number of vortices formed upstream.

system is produced for the Mach 3.37 and 5.26 flows, while a four-vortex system is produced for the Mach 8.23 flow. Since the vortices are highly unsteady for the Mach 3.37 flow, the number of vortices observed at a particular time instant may vary which is indeed the case in Figure 4.12. The six-vortex system can be seen clearly in Figure 4.13.

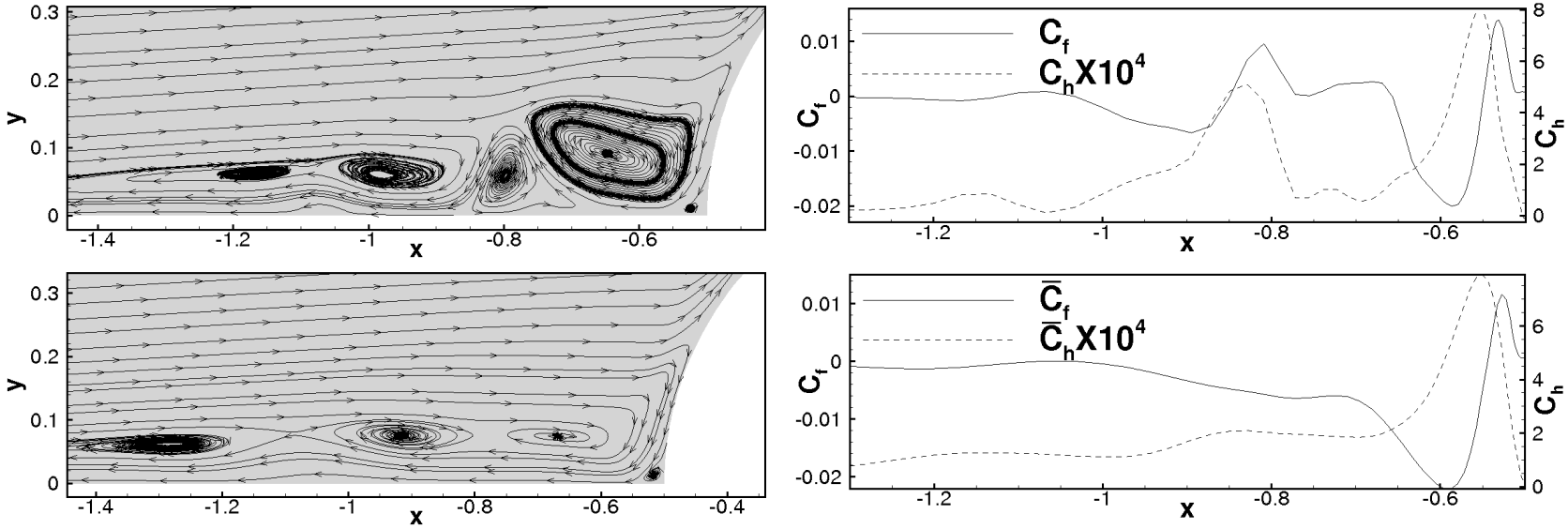

Figure 4.13: Figure depicting streamlines (left) and C_f and C_h variation (right) for Mach 3.37 with instantaneous (top) and mean (bottom) plots indicating the highly unsteady nature of the flow.

The six-vortex system is highly unsteady for the Mach 3.37 flow. Figure 4.13 shows the vortices formed upstream of the bump in the symmetry plane for the Mach 3.37 flow where both instantaneous and mean streamlines are shown to depict the vortices. Note that the number of vortices differ in the instantaneous and mean, indicating the unsteady nature of the separation. To quantify the effect of separation, the skin friction coefficient ($C_f = \tau_{wall}/0.5\rho_\infty u_\infty^2$) and Stanton number ($C_h = k\frac{\partial T}{\partial y}|_{wall}/\rho_\infty u_\infty C_p|T_w - T_\infty|$) are shown for the Mach 3.37 flow in the symmetry plane in Figure 4.13.

Both instantaneous and mean values are plotted. The effect of counter-rotating vortices can be seen observed in the change in sign in C_f in the instantaneous curve. The vortices closest to the roughness appear to be strongest and cause a significantly higher C_f and C_h than the laminar values in its vicinity. The vortex present at $x = -15.8$ is unsteady and does not appear in the mean. Note that regions of high C_f occur close to the center of the vortices while regions of high C_h occur in regions between two vortices.

4.5.2 Counter-rotating streamwise vortices

The spanwise vortices formed upstream wrap around the roughness to give rise to streamwise vortices downstream of the roughness. Figure 4.14 shows a schematic of the streamwise vortices observed in a streamwise plane at the center of the roughness. Very close to the roughness, there is a vortex (SP) which with increasing downstream distance would move closer to the symmetry plane due to the induced velocity by the image vortex and the low pressure region created behind the roughness. Therefore, one vortex from both sides of the roughness moves closer to the symmetry plane giving rise to a counter-rotating vortex pair. These are referred to as the Symmetry plane vortices (SP). Away from the symmetry plane, counter-rotating vortex pair(s) are formed which are the continuation of the vortex tubes from upstream. These are referred to as the Off-Symmetry plane vortices (OSP). Thus, downstream of the roughness, there exist counter-rotating SP and OSP vortices.

The counter-rotating vortices may be oriented so as to have an upwash or downwash between them. This depends on the flow conditions and the relative strength of the vortices upstream. When the vortices have an upwash, the effect of the mirror vortices is to induce them to move towards each other thus strengthening the magnitude of the vertical velocity between them. On the other hand, for vortices with a central downwash,

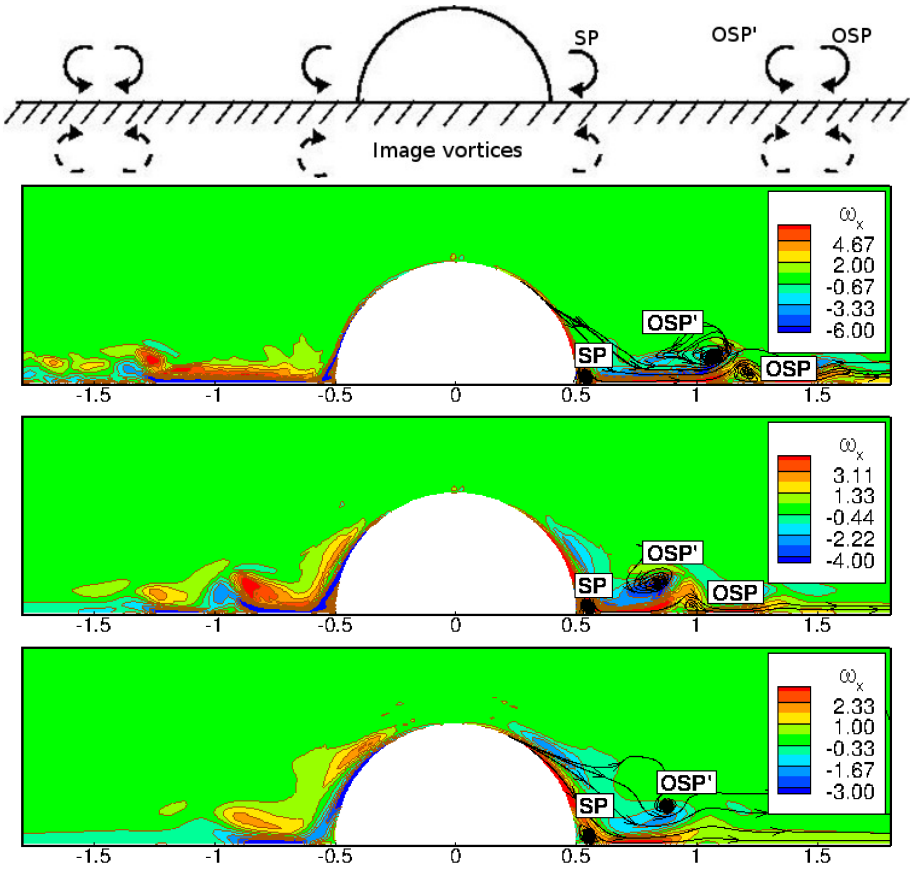

Figure 4.14: Figure showing contours of instantaneous ω_x along with contour lines (brown), and instantaneous streamlines (black) for Mach 3.37 (top), 5.26 (centre) and 8.23 (bottom) respectively depicting the streamwise vortices at x =0 in the $y-z$ plane.

the effect of the mirror vortices is to move the vortices away from each other; in effect weakening the velocity induced between them. Based on this reasoning, counter-rotating vortices with a central upwash close to the wall are more likely to induce transition as compared to those with a central downwash.

M_∞	$\omega_{x,SP}$	$\omega_{x,OSP}$	$\omega_{x,OSP'}$	$\omega_{z,max}$
3.37	9.6	-5.4	3.6	-4.5
5.26	5.9	-5.1	1.7	-3.0
8.23	1.7	-1.1	-	-1.5

Table 4.3: Table showing the strength of the streamwise vortices at x =0 depicted in Figure 4.14.

Figure 4.14 shows the instantaneous ω_x contours and streamlines at a streamwise plane in the center of the roughness to illustrate the nature of the streamwise vortices . The number of vortices is higher for Mach 3.37 and 5.26 due to the higher number of upstream vortices. Also, the spanwise location of the OSP vortices for Mach 3.37 oscillates with time due to the highly unsteady upstream vortices. Transient growth theory predicts that streamwise vortices are optimal disturbances for boundary layers. The streamwise vortices predicted by transient growth are counter-rotating and equal in strength. However, the OSP vortices created by the roughness element differ in the following respects: (i) Vortices with positive ω_x have their center located closer to the wall as compared to the vortices with negative ω_x and thus the line joining the center of the vortices is at an angle to the wall. (ii) the size and strength of the counter-rotating vortices is noticeably different. (iii) they are not periodic in the span.

Table 4.3 lists the magnitude of the streamwise vorticity at the center of the respective vortices whose nomenclature is based on the schematic in Figure 4.14. The maximum ω_z listed is for an unperturbed boundary layer at the location of the roughness. From Table 4.3, the strength of the streamwise vortices is higher for a higher spanwise vorticity from the unperturbed boundary layer and thus is highest for Mach 3.37 and least for Mach 8.23. Note that the strength of the vortices decreases with increasing distance from the roughness element. The SP vortices are the strongest of the vortices, hence implying a higher likelihood of the flow breaking down in the symmetry plane.

4.5.3 Perturbation of shear layer

The boundary layer separates on either side and downstream of the roughness element creating a separated shear layer which is shown in Figure 4.15 for Mach 3.37. Far upstream, it can be seen that the boundary layer is attached and two-dimensional. The spanwise extent of the shear layer depends on the upstream separation length. At the center of the roughness (x=-15), the smaller SP vortex forms away from the shear layer while the larger OSP vortices are in contact with the shear layer. Downstream of the roughness, this shear layer in the symmetry plane is close to the SP vortices.

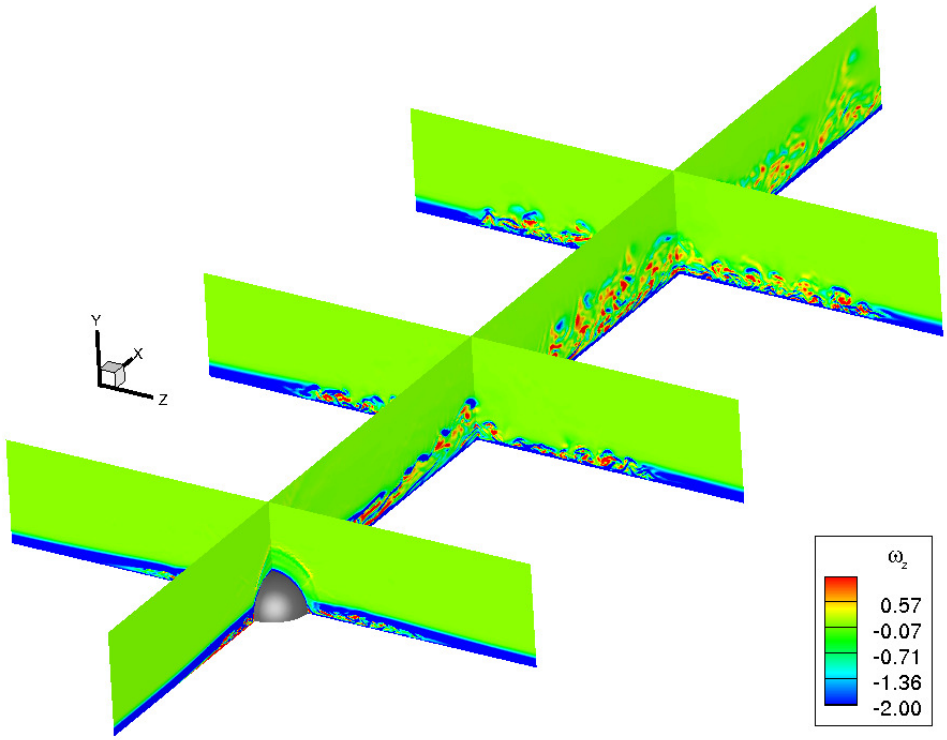

Figure 4.15: Figure showing the separation shear layer formed due to the roughness using contours of spanwise vorticity for Mach 3.37 flow.

The counter-rotating SP and OSP vortices perturb the shear layer in their vicinity. The size, strength and magnitude of unsteadiness of the vortices determines the nature

of the perturbation to the shear layer; the receptivity and stability characteristics of the shear layer determines whether or not the flow undergoes transition. Note that these perturbations are inhomogeneous in the span and therefore Bi-global stability theory (Choudhari *et al.* [15], Groskopf, Kloker & Marxen [27]) could lead to a better understanding of the instability mechanisms associated with such flows. From Figure 4.15, it can be seen that the flow breaks down downstream of the roughness both at and away from the symmetry plane.

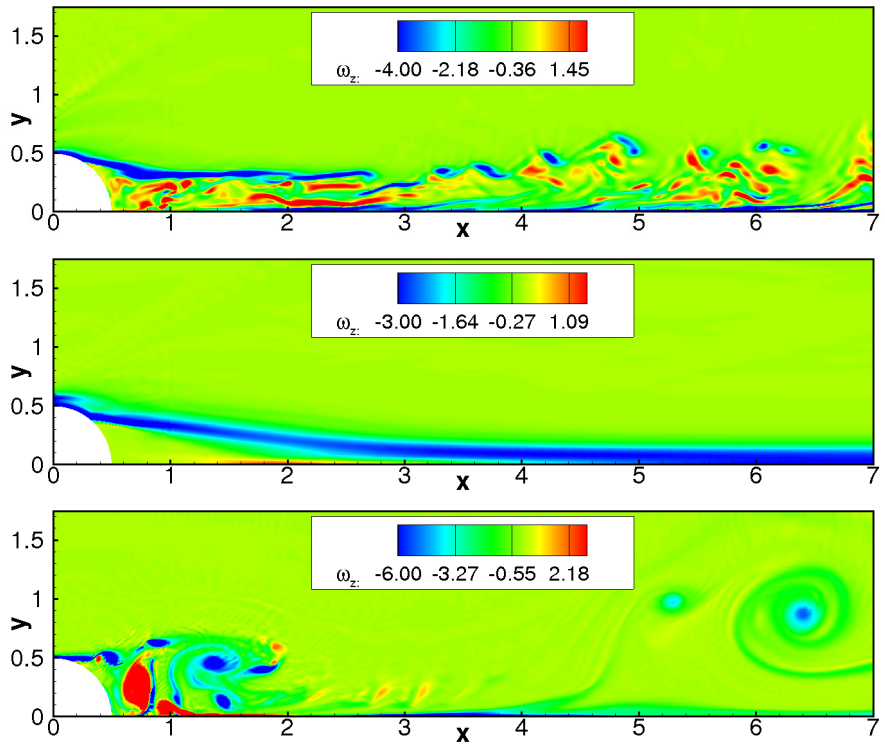

Figure 4.16: Figure showing contours of instantaneous ω_z for symmetry plane three-dimensional simulation (top), Mach 3.37 two-dimensional simulation (center) and incompressible two-dimensional simulation (bottom).

It is known at low-speeds that a uniform shear flow past a sphere sheds hairpin shaped vortices (Sakamoto & Haniu [51]). Also, Acarlar & Smith [1] observed that hairpin vortices form behind a teardrop shaped obstacle placed on a flat plate at incompressible speeds even though the horseshoe vortices around the obstacle are absent. To assess whether such shedding takes place in the current simulations, we perform a

two-dimensional simulation past a semi-circular hump with identical free-stream and wall conditions of the Mach 3.37 boundary layer. We also perform a two-dimensional incompressible simulation with the same Re_D as Mach 3.37 to assess any effect of compressibility. The shear layer downstream of the roughness for the two-dimensional cases is shown along with the symmetry plane shear layer from the three-dimensional simulation in Figure 4.16.

Although some unsteadiness was observed in the two-dimensional Mach 3.37 flow downstream, the shear layer re-attaches with the flat plate without breaking down, in contrast to the three-dimensional case, where the shear layer breaks down due to the SP vortices. The incompressible two-dimensional simulation revealed that vortex shedding occurred downstream of the roughness similar to the shedding behind a bluff body. This indicates that the breakdown of the shear layer downstream of the bump in the three-dimensional flow is due to its perturbation by the streamwise vortices below it. The absence of vortex shedding at supersonic speeds was also observed by Chang & Choudhari [12] who performed a parametric study of the effect of two-dimensional roughness on a flat plate at subsonic and supersonic speeds and subcritical Reynolds numbers. They conclude that the absolute vortex shedding process was weak at supersonic speeds and hence convective instabilities might become more dominant at high speeds.

4.5.4 Sources of unsteadiness

When a laminar supersonic boundary layer interacts with a roughness element, possible sources of unsteadiness are due to the unsteady vortex system upstream, shock-induced unsteadiness and shear layer instability. In Section 4.5.1, it was seen that the Mach 3.37 flow was highly unsteady upstream. The unsteadiness is also observed in incompressible flows (see e.g. Baker [3]) and depends on Reynolds number. The upstream separation region with discrete counter-rotating vortices becomes unstable beyond a critical Re and becomes unsteady. When the supersonic boundary layer comes in contact with the roughness element, a shock wave is produced at the wall normal location corresponding to the sonic line. This shock which is inherently unsteady, could potentially perturb the flow in the vicinity of the roughness element thereby causing the flow to become unstable. As described in Section 4.5.3, a three-dimensional separation shear layer is formed. Streamwise vortices exist below both the shear layers and act as a perturbation.

Also, the shear layer contains inflexion points in its mean profile and is susceptible to the inviscid Kelvin-Helmholtz instability. Depending on the Mach number and Reynolds number, the shear layer could become unstable.

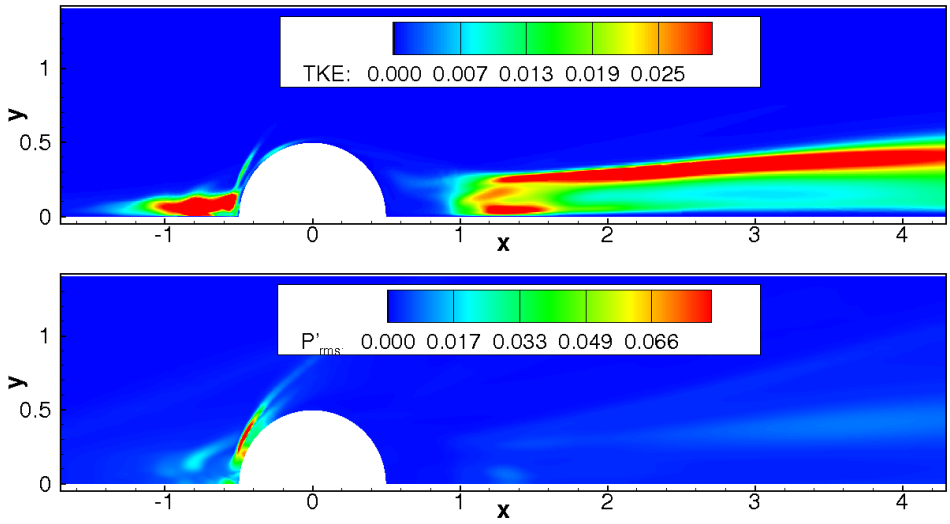

Figure 4.17: Figure showing sources of unsteadiness for Mach 3.37. $p'_{rms}/\bar{p}$ contours are shown to depict shock-induced unsteadiness (top). TKE contours are shown in the symmetry plane (bottom) to depict the unsteadiness due to the vortices and shear layer.

One or more of the above factors can cause the flow to break down and undergo transition. Figure 4.17 illustrates the above sources of unsteadiness for the Mach 3.37 flow. Note the p'_{rms} is highest at the shock location upstream while the turbulent kinetic energy ($TKE = \overline{u'_i u'_i}/u^2_\infty$) is highest in the vortex system upstream and the shear layer downstream. The p'_{rms} contour suggests that the secondary shocks formed downstream of the roughness are relatively weak and thus are less likely to contribute to transition of the flow.

Figure 4.18 shows the wall-normal variation of TKE in the symmetry plane for the three flows. Three upstream and downstream locations are selected whose distance from the roughness is indicated in the figure. Upstream of the roughness, the Mach 3.37 flow is highly unsteady, while the higher Mach number flows are nearly steady. The maximum unsteadiness for Mach 3.37 occurs 1D upstream of the bump indicating that it is due to the unsteady spanwise vortices. The maximum unsteadiness occurs closest to the

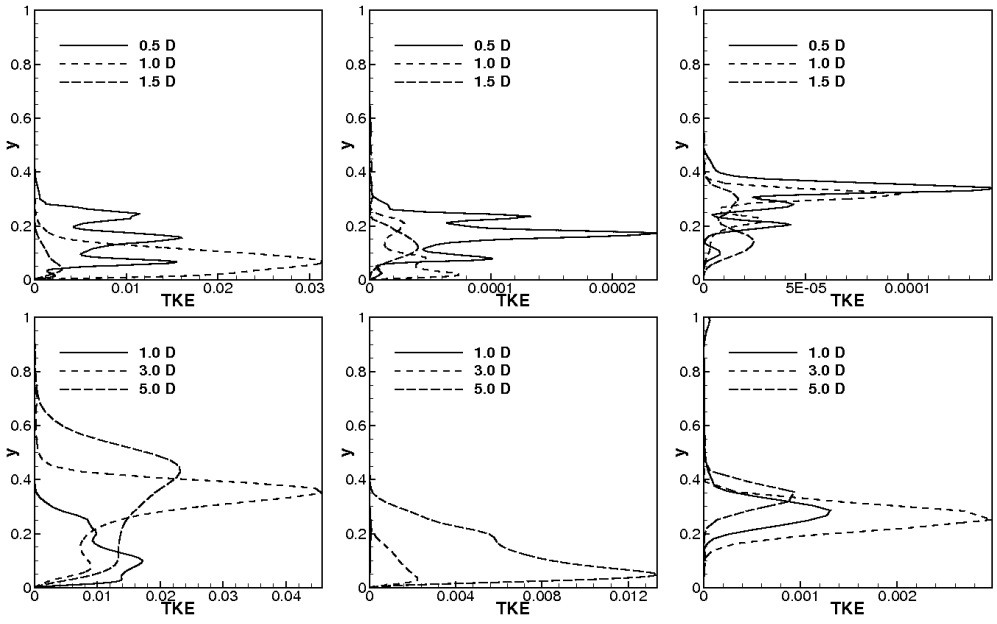

Figure 4.18: Figure showing wall-normal variation of turbulent kinetic energy (TKE) upstream (top) and downstream (bottom) of the bump for Mach 3.37 (left), 5.26 (center) and 8.23 (right) in the symmetry plane. Distance from the center of the roughness is indicated in the figures.

bump for Mach 5.26 and 8.23 away from the wall suggesting that it is due to the shock produced by the roughness. Thus, we see that the shock-induced unsteadiness is weak for the cases considered whereas the unsteadiness from the vortex system is strong for Mach 3.37. Downstream of the roughness, the unsteadiness is stronger than upstream for Mach 5.26 and 8.23 due to the perturbation of the shear layer by the streamwise vortices. For Mach 3.37 and 5.26, note that the unsteadiness increases with distance from the bump indicating the likelihood of transition further downstream. For Mach 8.23, the unsteadiness is an order of magnitude lower than the corresponding values for Mach 3.37 and 5.26 and decreases between 3D and 5D downstream indicating that the flow is stable to the perturbation of the shear layer . Thus, the unsteadiness due to the shear layer is strong for Mach 3.37 and 5.26 and weak for Mach 8.23.

M_∞	Unsteadiness in Vortex System	Shock-induced Unsteadiness	Shear layer Unsteadiness
3.37	**strong**	weak	**strong**
5.26	weak	weak	**strong**
8.23	weak	weak	weak

Table 4.4: Table indicating the strength of unsteadiness based on the magnitude of TKE due to the different possible sources.

Based on the observations from Figure 4.18, we classify the unsteadiness from the three possible sources based on the magnitude of TKE in Table 4.4. The shock-induced unsteadiness appears to be weak for all the three cases. For Mach 3.37, where the flow transitions closest to the roughness, the unsteadiness in both the upstream vortex system and the shear layer downstream are strong. In contrast, for Mach 5.26, the upstream vortices are nearly steady while the shear layer appears to be unstable, leading to larger levels of unsteadiness downstream. For Mach 8.23, the unsteadiness is weak both in the upstream separation region and in the shear layer downstream.

4.5.5 Hairpin-shaped vortices

Transition is characterized by the prominent presence of hairpin vortices. Recall that the SP and OSP vortices perturb the separation shear layer, and for Mach 3.37 and 5.26, the shear layers are unstable and break down. The shear layer can be visualized as lines of vorticity. The counter-rotating streamwise vortices have an upwash or downwash at their center depending on their direction of rotation, and can be visualized using the Q-criterion (Hunt, Wray & Moin [29]):

$$Q = -0.5 \frac{\partial u_i}{\partial x_j} \frac{\partial u_j}{\partial x_i} \tag{4.2}$$

Figure 4.19 visualizes the streamwise vortices and shear layer for all three Mach numbers. Note that the vortex lines are perturbed at spanwise locations corresponding to the streamwise vortices. For Mach 3.37 and 5.26, the counter-rotating vortices have an upwash causing the vortex lines to form hairpin-shaped loops. For Mach 3.37, one such loop is formed at the symmetry plane and one on either side due to the OSP vortices. For Mach 5.26, two such loops are formed close to the symmetry plane with one on either side. For Mach 8.23, two pairs of counter-rotating vortices are formed close to the symmetry plane which have a downwash at each of their centers respectively. As a result, inverted hairpin loops form on either side of the symmetry plane.

When the strength of the streamwise vortices is large enough, the hairpin loops break-away to form coherent hairpin vortices. Figures 4.20-4.22 show iso-contours of Q colored by instantaneous streamwise velocity for Mach 3.37 and 5.26 respectively. Note the vortical fine scale structures created by the roughness and spreading of the turbulent wake. Even close to the outflow, coherent hairpin vortices are observed in what appears to be a visibly turbulent flow. Note that close to the outflow, the spanwise extent of the turbulent region is higher for Mach 3.37 as compared to Mach 5.26. The appearance of hairpin vortices is striking for both cases. Initially trains of hairpins are seen but with increasing downstream distance, they spread in the span giving rise to more such vortices and far downstream, the entire span is populated by such hairpins. Note that for Mach 5.26, the presence of hairpin vortices occurs farther away from the roughness when compared to Mach 3.37 and this is consistent with the experimental observations discussed in Section 4.4. Such hairpin vortices have also been observed at incompressible speeds behind a hemispherical protuberance by Acarlar & Smith [1] and

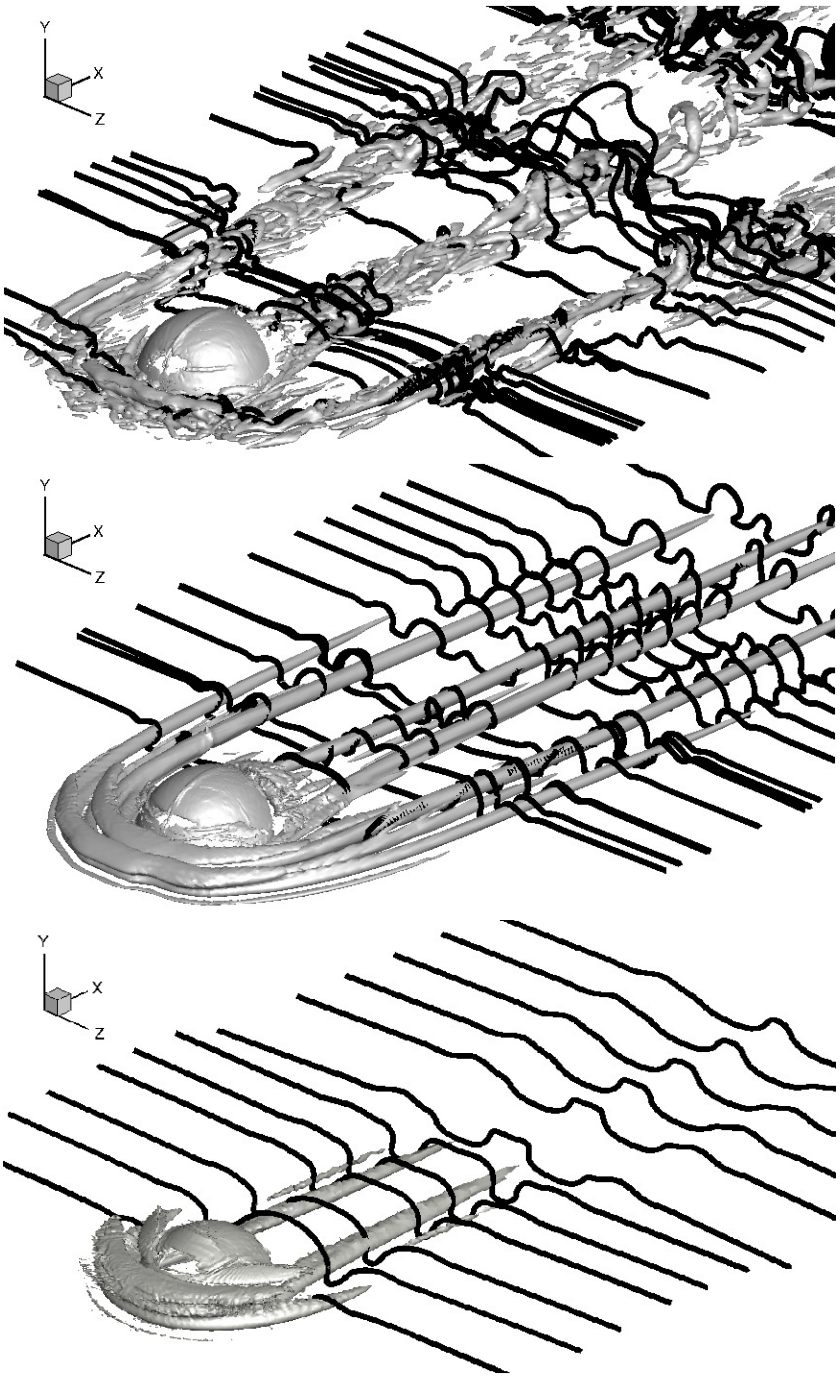

Figure 4.19: Isocontours of Q-criterion with instantaneous vortex lines for Mach 3.37 (top), 5.26 (center) and 8.23 (bottom).

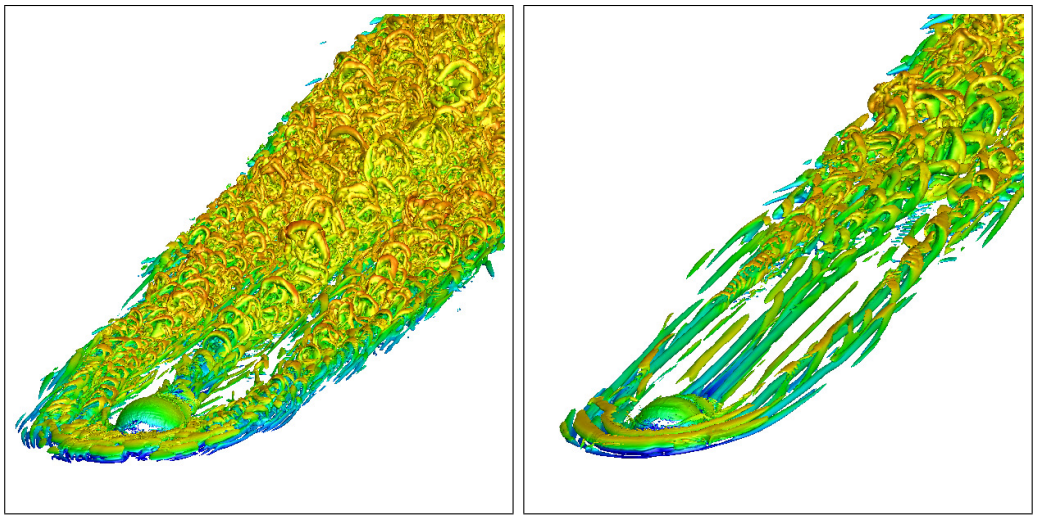

Figure 4.20: Q=0.25 and 0.1 isocontours coloured by streamwise velocity for Mach 3.37 (left) and 5.26 (right) depicting hairpin-shaped vortices.

Klebanoff, Cleveland & Tidstrom [30]. They also observe that with increasing downstream distance from the roughness, secondary vortices are formed and far downstream the flow resembles a turbulent boundary layer. The mean velocity profiles also closely match a canonical turbulent boundary layer profile indicating that the hairpin vortices caused the flow to transition to turbulence.

Note that the Mach 8.23 flow does not undergo transition, and the hairpin vortices are conspicuously absent. As in Section 4.5.2, a downwash between the counter-rotating vortices implies a weakening of their effect due to their moving away from each other. Closer to the outflow for Mach 8.23, one vortex from either side of the symmetry plane moves closer to each other as to create an upwash between them. Although their strength has considerably decreased with increasing distance, it is therefore possible that the Mach 8.23 boundary layer might undergo transition at even larger distances downstream.

4.5.6 Temporal Spectra for Mach 3.37

Data were collected at locations both upstream and downstream of the roughness for Mach 3.37 to obtain the dominant frequencies in the flow. The data were collected over four domain flow through times, corresponding to an interval of 200 D/u_∞. The

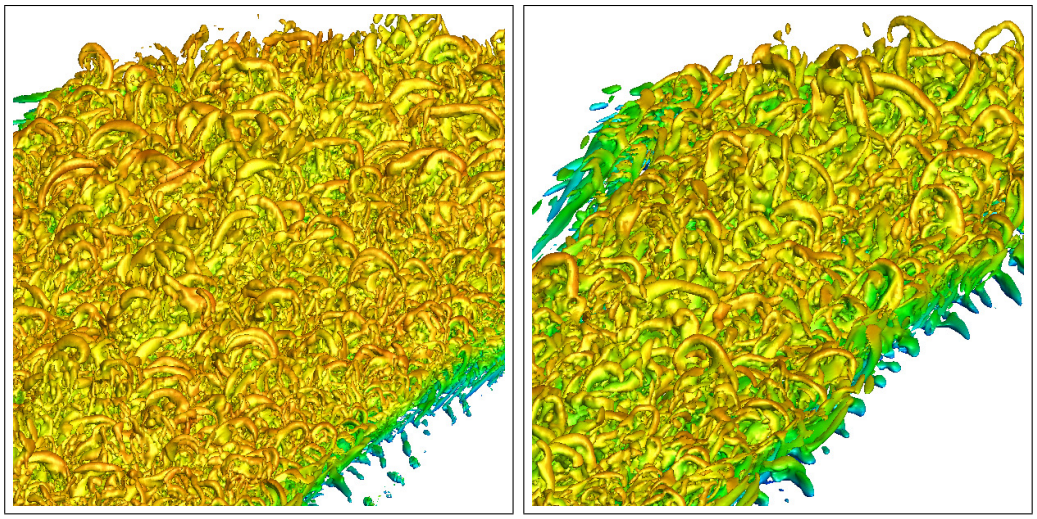

Figure 4.21: Hairpin vortices far downstream for Mach 3.37 (left) and Mach 5.26 (right). Q=0.25 (left) and Q=0.1 (right) colored by streamwise velocity contours.

spectra are reported at the points close to the wall except otherwise specified in the figures. The pressure signals 2-3 D upstream of the roughness (Figure 4.23) indicate a dominant Strouhal number ($St = fD/u_\infty$) of St =0.023 corresponding to a dimensional frequency of $f = 8$ KHz based on $u_\infty = 1400\ m/s$ from the experiment. The St =0.023 is prominent even 0.4D away from the symmetry plane. The streamwise location and the amplitude of the fluctuations suggest that this frequency is related to the first separation point of the boundary layer. The v velocity spectra (Figure 4.23) showed that St =0.2 is dominant 1 and 2D upstream of the roughness. This frequency is likely related to the unsteady vortex seen around x =-16 in Figure 4.13. Note that closer to the roughness at x =-16, the spectra appear more broadband compared to that at x =-17.

Wall pressure spectra are reported at different distances upstream of the roughness in the symmetry plane in Figure 4.24. Also plotted are lines of slope -1 and -5 which have been observed in fully turbulent boundary layers by Choi & Moin [14] in the incompressible regime and by Pirozzoli & Grasso [44] and Beresh *et al.* [9] in the supersonic regime. Note that the spectra appear broadband closer to the roughness indicating the highly unsteady nature of the upstream vortices. The maximum spectral content occurs at $St < 0.2$ which showed up as a dominant peak in the v velocity spectra. Also shown in Figure 4.24 are the wall pressure spectra at points away from

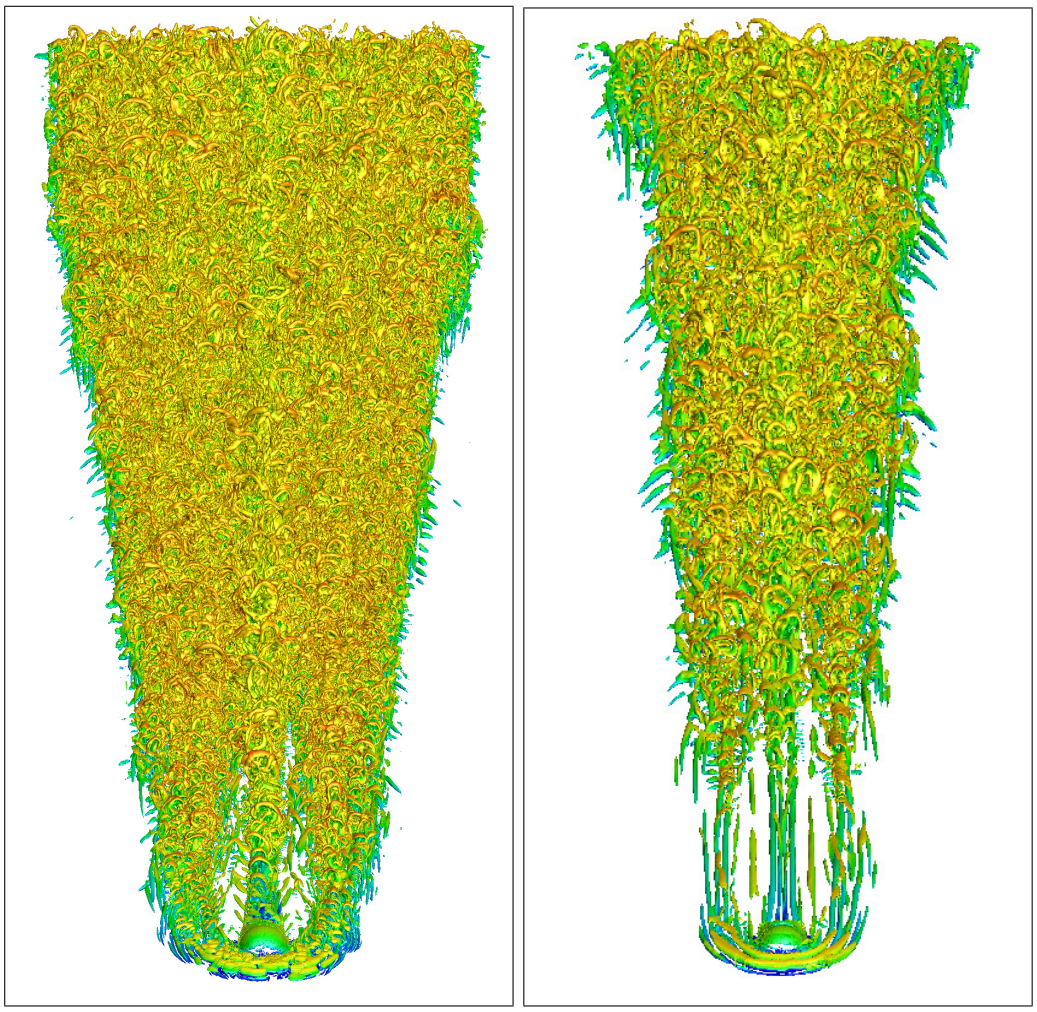

Figure 4.22: Top view of hairpin vortices for Mach 3.37 (left) and Mach 5.26 (right).

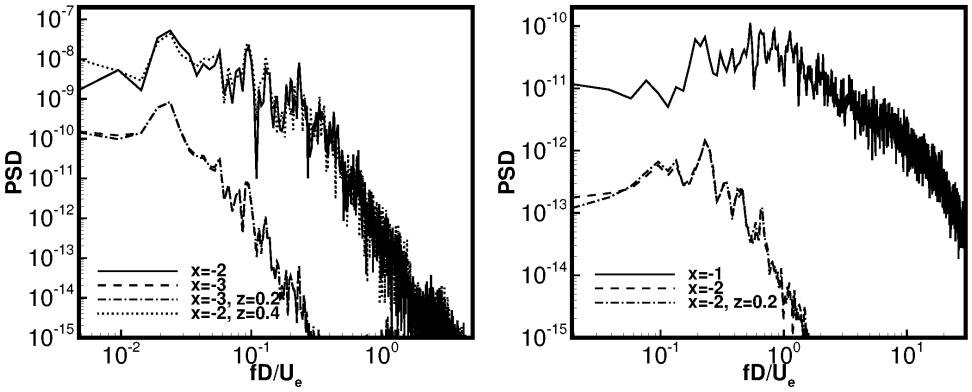

Figure 4.23: Temporal wall pressure spectra (left) and v velocity spectra (right) for Mach 3.37.

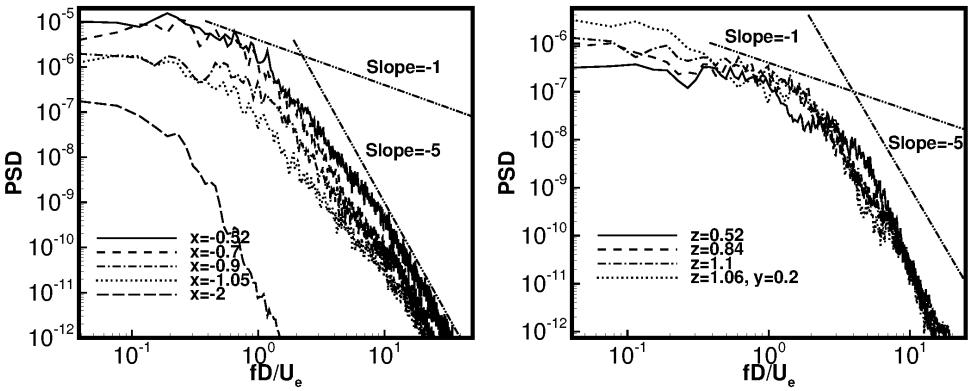

Figure 4.24: Temporal wall pressure spectra showing variation with distance from the roughness in the symmetry plane (left) and in the streamwise plane at the center of the roughness (right) for Mach 3.37.

the symmetry plane at the center of the roughness. The spectra again appear broadband as observed upstream but note that now the maximum spectral content occurs over a broader range of frequencies with $St < 1$.

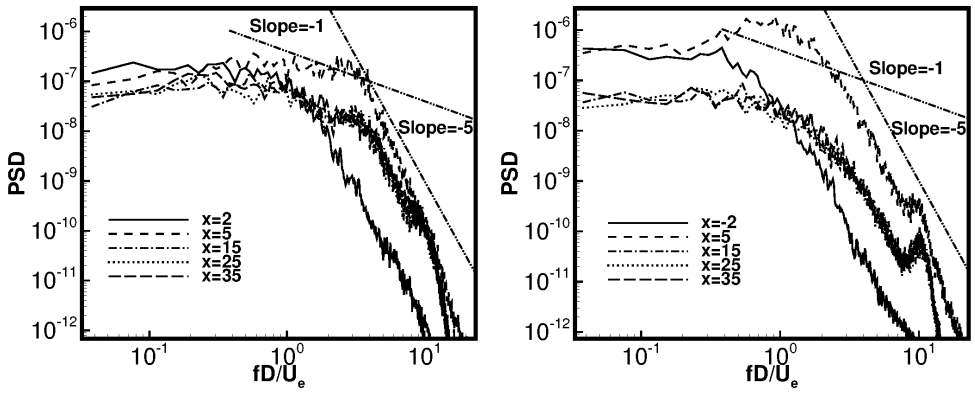

Figure 4.25: Temporal pressure spectra showing downstream evolution at the wall (left) and at y =0.5 (right) for Mach 3.37.

The downstream evolution of the pressure spectra at the wall and at 0.5D from the wall is shown in Figure 4.25. Note that beyond x =0, the curves collapse onto a single curve at both wall normal locations. The wall pressure spectra far downstream indicates a distinct region with a slope of -1 and the curve flattens out for lower frequencies. This behavior is also observed in Beresh *et al.* [9] for fully turbulent boundary layers for higher Re_θ and suggests that the flow is turbulent with characteristics of a canonical turbulent boundary layer.

4.5.7 Mean flow characteristics

Mean streamwise velocity and total kinetic energy (TKE) with streamlines is shown in Figure 4.26. The symmetry plane, wall–parallel plane ($y = 0.05\ D$) and a streamwise plane ($x = 5\ D$) is shown. TKE is shown in the symmetry and streamwise plane, while mean streamwise velocity is shown in the wall–parallel plane. The upstream separation region is clearly visible in the symmetry plane followed by a large recirculation vortex downstream of the roughness. In the wall–parallel plane, the flow separates similar to the flow behind a two–dimensional cylinder. Downstream of the roughness, two high–speed streaks are seen which are due to the SP and OSP streamwise vortices respectively.

The SP vortex is clearly visible in the streamwise plane.

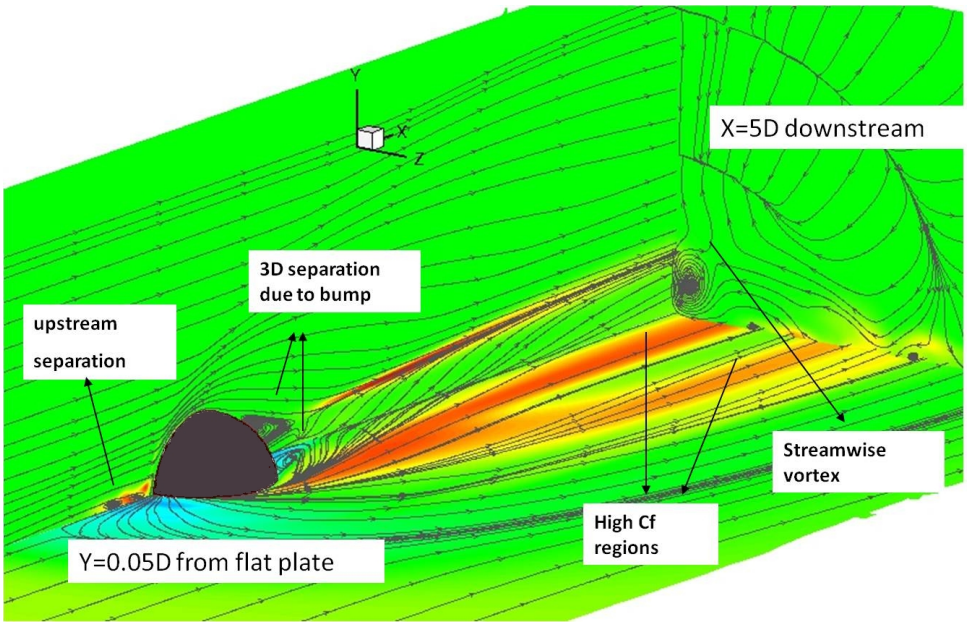

Figure 4.26: Figure showing mean flow feature for Mach 3.37 flow.

Mean Stanton number (C_h) contours are shown at the wall for all the 3 Mach numbers in Figure 4.27. As expected, transition causes higher C_h due to a larger temperature gradient at the wall. Immediately downstream of the roughness, streaks of higher C_h are observed for all 3 Mach numbers at locations corresponding to the streamwise vortices. The streamwise vortices transport higher temperature fluid towards the wall and lower temperature fluid away from the wall causing this increase in C_h. Note that since T_{wall}/T_{aw} <1, the maximum temperature in the laminar boundary layer occurs away from the wall. For Mach 3.37, the hairpin vortices cause increased spanwise mixing of the flow which yields a larger region of high C_h beyond x =-10. With increasing downstream distance, it can be seen that the flow becomes more uniform in the span. Similar behavior is observed for Mach 5.26. For Mach 8.23, a pair of high C_h streaks are formed whose strength decreases with increasing downstream distance consistent with the flow not transitioning.

Figure 4.28 shows the streamwise variation of mean C_f at $z = 0$, 0.5 and 1.0 from the symmetry plane for the three Mach number flows. Also plotted is the laminar C_f curve if

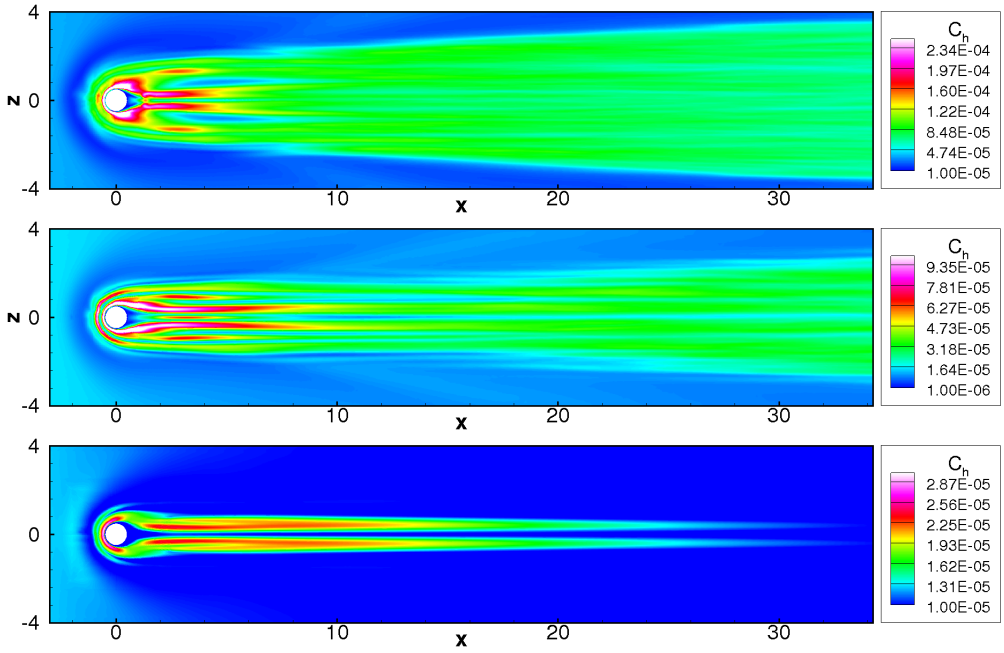

Figure 4.27: Stanton number (C_h) contours for Mach 3.37 (top), 5.26 (center) and 8.23 (bottom).

the roughness were absent (obtained from a similarity solution) and a turbulent C_f curve if the boundary layer were turbulent from the leading edge of the flat plate. Upstream of the bump, the C_f matches the laminar value as expected. Close to the bump, the effect of upstream separation is seen where the C_f is negative. Immediately downstream of the bump, there is a significant rise in C_f for all the three flows, which is attributed to both the presence of streamwise vortices which transport higher momentum fluid from above to the near-wall region and the acceleration of the mean flow as it moves towards the low-pressure region created downstream of the bump. Beyond the low-pressure region, the C_f decreases as expected.

For Mach 3.37, the C_f rises significantly above the laminar value and remains high indicating that the flow has transitioned. This location corresponds to the break-up of the hairpins causing the flow to undergo transition. At x =-10, there is a significant spanwise variation in C_f but closer to the outflow, the C_f appear to converge to a single value. Note that Re_θ ranges from 1000-2400 and is significantly higher in the symmetry plane compared to other locations. This can be attributed to the upward

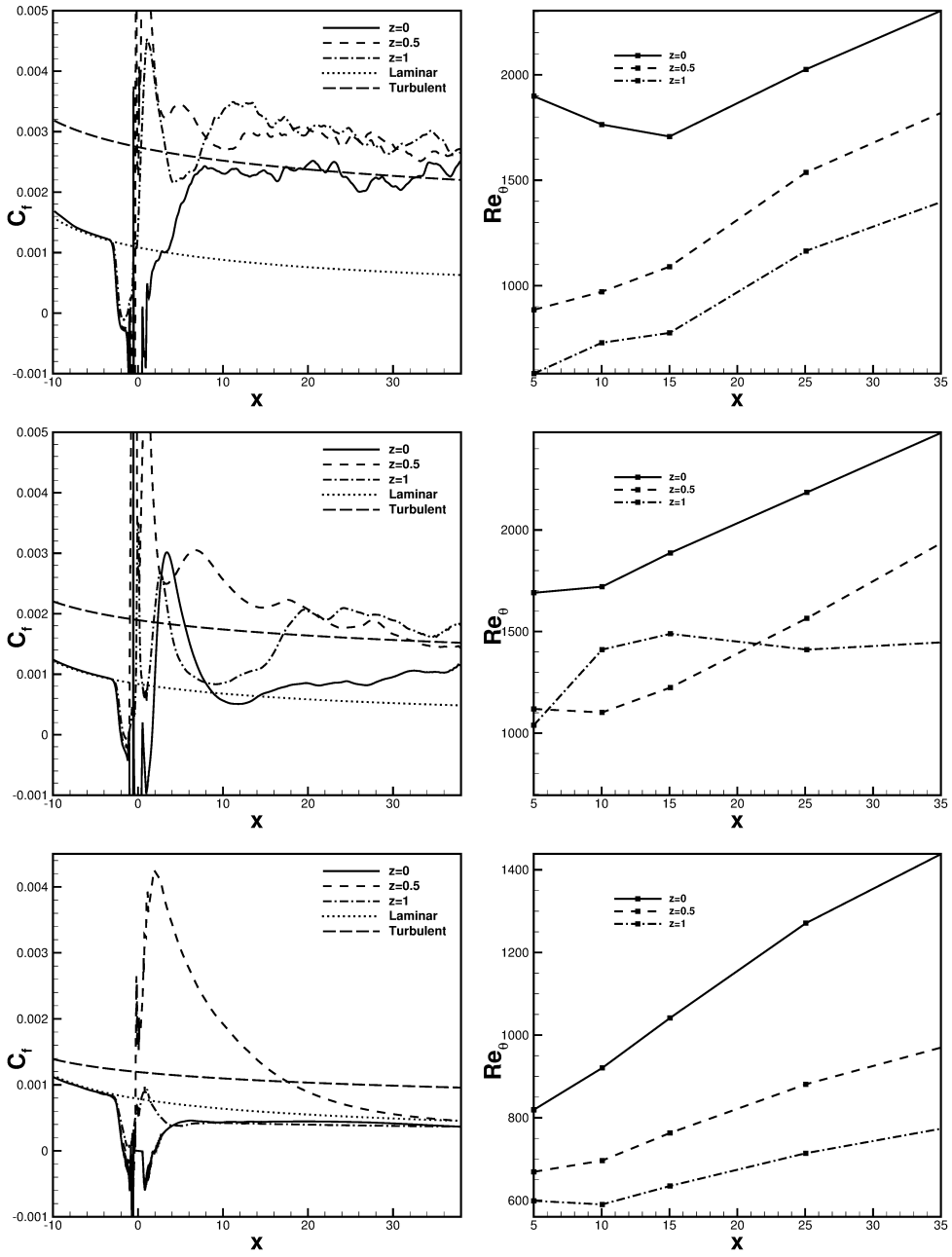

Figure 4.28: Mean skin friction coefficient and Re_θ variation with x at z=0, 0.5 and 1.0 for Mach 3.37, 5.26 and 8.23 respectively.

deflection of the flow by the roughness element resulting in a higher boundary layer thickness. For Mach 5.26, the flow begins to undergo transition beyond $x = 0$ at z =0 and 1, indicated by the rise in C_f. As for Mach 3.37, towards the outflow, the C_f curves appear to converge towards a single value indicating a turbulent flow. The variation of Re_θ is similar to the Mach 3.37 flow. For Mach 8.23, except at the location of the streamwise vortices, the C_f remains below the laminar value and approaches it with increasing downstream distance. At $z = 0.5$, the C_f increases sharply to about 4 times the laminar value and decreases with downstream distance approaching the laminar value. It is interesting that even for a flow that does not undergo transition, the effect of the roughness element is to cause a significant rise in C_f and C_h (Figure 4.27) for a reasonable distance downstream.

Authors	M_∞	Re_θ	T_w/T_∞
Coleman, Kim & Moser [16]	3	4880*	1
Duan, Beekman & Martin [23]	4.97	1279.1	1
Spalart [60]	–	1410	–

Table 4.5: Table showing flow conditions for studies being compared to in Figures 4.29 and 4.30. (* defined based on channel half width and wall viscosity)

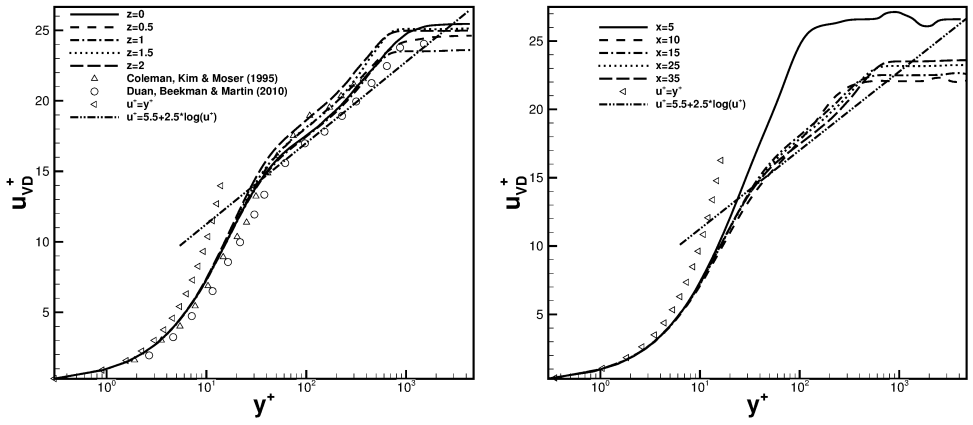

Figure 4.29: Van-Driest transformed velocity profiles at $x = 35$ (left) and $z = 1$ (right) for Mach 3.37.

Figure 4.29 shows profiles of the Van-Driest transformed velocity (u^+_{VD}) downstream of the roughness for Mach 3.37. The Van-driest transformation is defined as:

$$u^+_{VD} = \int \sqrt{\frac{\rho}{\rho_w}} du^+ \tag{4.3}$$

Also plotted are data from Coleman, Kim & Moser [16] and Duan, Beekman & Martin [23] (Table 4.5). Since the Mach 3.37 flow corresponds to a cold-wall (T_w/T_{aw} =0.3), the Van-driest transformed velocity is compared to past studies with a similar wall condition. The shape of the curves resemble a fully developed turbulent boundary layer profile. Note that the velocity profiles deviates from the linear law at around $y^+ = 2$ which appears to be typical of cold-wall turbulent boundary layers. Also, note that although the slope of the log-law matches well with the expected value, the intercept is slightly higher than the incompressible value. This again appears to be in line with expectations of a cold-wall flow as observed by Coleman, Kim & Moser [16]. Note that the flow is still three-dimensional close to the outflow with small spanwise variations in the velocity profile. Also shown is the downstream evolution of the Van-Driest transformed profile at $z = 1$. Note that at x =5, the profile resembles that of a laminar flow while with increasing distance downstream, the profile approaches that of a fully developed turbulent boundary layer.

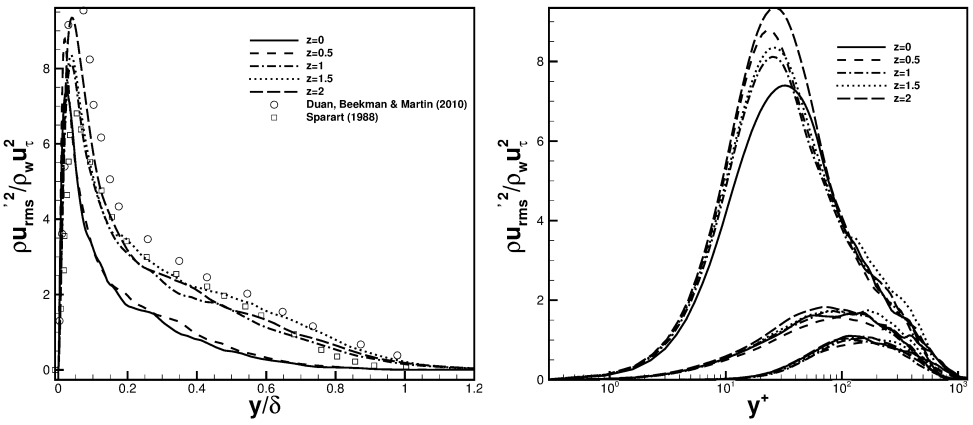

Figure 4.30: Reynolds stresses at z=0, 0.5, 1, 1.5 and 2 and $x = 35$ for Mach 3.37.

Figure 4.30 shows the variation of $\rho u'^2_{rms}/\rho_w u^2_\tau$ with y/δ and y^+ at z =0, 0.5, 1, 1.5 and 2 and 35D from the roughness for Mach 3.37. δ was computed based on the

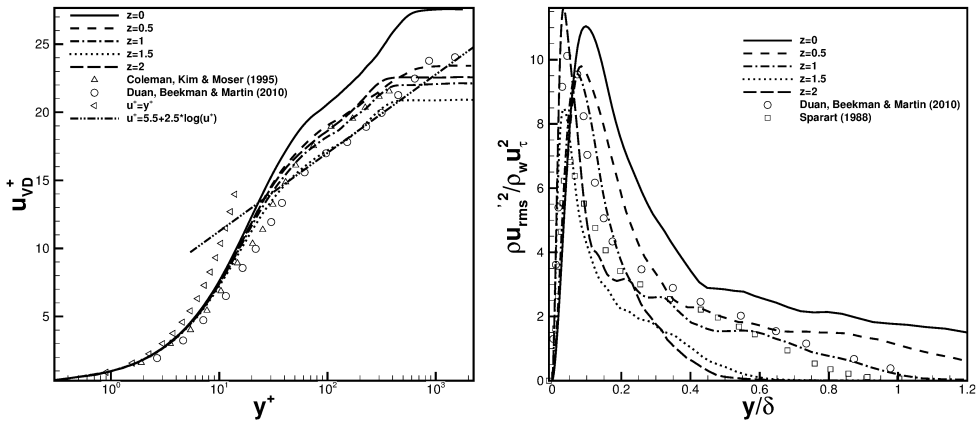

Figure 4.31: Van-Driest transformed velocity and Reynolds stress profiles at z=0, 0.5, 1, 1.5 and 2 and $x = 35$ for Mach 5.26.

location at which $u = 0.99u_\infty$. Also plotted are results from Duan, Beekman & Martin [23] and Spalart [60] for comparison. Good agreement is observed indicating that the flow is turbulent. Figure 4.31 shows the Van-Driest transformed velocity and Reynolds stress profiles at x =35 for Mach 5.26. Note that the variation in z is greater for Mach 5.26 as compared to Mach 3.37.

4.5.8 Local Reynolds number correlating transition

From the above discussions, the flow downstream of the hemispherical roughness element appears to undergo transition for Mach 3.37 and 5.26 and remains laminar for Mach 8.23. A combination of factors could be responsible for this behavior at different flow conditions. Table 4.6 lists the free-stream Reynolds number for the three cases considered. It is known from stability theory that compressibility stabilizes the flow and our results are consistent with this with the least Mach number flow being most unstable and therefore undergoing transition to turbulence. It is also known in incompressible flows that a higher boundary layer thickness moves the transition point away from the roughness element due to the reduction in Re_k computed based on conditions at the roughness height and our results are consistent with this behavior with the lowest boundary layer thickness case (Mach 3.37) transitioning closest to the bump. The free-stream Reynolds number based on roughness diameter (Re_k) is highest for Mach 8.23

which remains laminar. To account for the effect of boundary layer thickness and wall temperature, we compute a local Reynolds number based on free-stream velocity, wall kinematic viscosity and diameter of roughness ($Re_{k,wall} = \frac{u_\infty k}{\nu_w}$) and we see that this parameter is indicative of the trend observed for transition for the three cases. Mach 8.23 flow has the least $Re_{k,wall}$ while Mach 3.37 flow has the highest $Re_{k,wall}$.

We also quantify the potential for transient growth to examine whether it correlates with the behavior of transition observed. From [49], we know that transition occurs when E_{tr} reaches a specific value. E_{tr} is defined as follows:

$$(E_{tr})^{0.5} = (G^{0.5}/Re_\theta)Re_\theta(k/\theta)(T_e/T_w)^{0.5} \tag{4.4}$$

$G^{0.5}/Re_\theta$ is obtained from Figure 1 of Reshotko & Tumin [49]. The values of $E_{tr}^{0.5}$ from Table 4.6 indicates that it correlates well with the observed trend of transition from the current DNS. Mach 3.37 flow undergoes transition closest to the roughness and has the highest value of E_{tr} and the 8.23 flow has the least E_{tr} and does not undergo transition.

M_∞	Re_k	$Re_{k,wall}$	$E_{tr}^{0.5}$
3.37	9121	11364	614
5.26	14190	4629	573
8.23	16831	1104	415

Table 4.6: Table showing Re_k, $Re_{k,wall} = \frac{u_\infty k}{\nu_w}$ and transient growth energy ($E_{tr}^{0.5}$) for the cases simulated.

4.6 Conclusions

The effects of an isolated hemispherical roughness element on a laminar high-speed boundary layer have been simulated for three Mach numbers wherein the highest Mach number flow remains laminar downstream and the lower Mach number flows undergo transition. Qualitative and quantitative comparison with experiments show good agreement. A qualitative mechanism for transition is proposed. The three dimensional separation of the boundary layer due to the presence of the roughness produces a shear

layer and a system of vortices upstream and downstream of the bump. The unsteady counter-rotating streamwise vortices perturb the shear layer which break down further downstream to yield hairpin-shaped vortices. Hairpin-shaped structures are observed for the flows that transitioned. It was seen that for the Mach 8.23 flow, which did not transition, the counter-rotating vortices had a downwash between them which effectively reduced their strength with increasing downstream distance. The significant jump in skin friction coefficient and wall heat transfer rates from the laminar value were used to confirm the transitional behavior of the flow downstream of the bump. It was also seen that even for the flow that remained laminar downstream, the skin friction coefficient and heat transfer rates could be significantly higher immediately downstream of the bump for a reasonable distance downstream before it approaches the laminar value. The transfer of momentum and heat by the streamwise vortices is responsible for the significant rise in C_f and q_{wall} immediately downstream. Some spanwise variation in the flow close to the outflow was observed in the mean indicating the three-dimensional nature of the flow. The Van-Driest transformed velocity and Reynolds stresses indicated that the Mach 3.37 and Mach 5.26 flows behaved similar to a canonical turbulent boundary layer. Temporal wall pressure spectra for Mach 3.37 flow showed that $St = 0.023$ was dominant upstream of the roughness, while downstream, the flow was highly unsteady and broadband with the nature of the curve far downstream resembling that of a canonical turbulent boundary layer. A local Reynolds number based on the wall properties appeared to correlate the tendency to transition when compared to the Reynolds number based on free-stream properties.

Chapter 5

Effect of boundary layer thickness: Hemispherical roughness

5.1 Problem Description

In Chapter 4, the mechanism of transition for a large roughness element was discussed. It was seen that the boundary layer separates upstream of the roughness, giving rise to a system of spanwise vortices. The upstream system of spanwise vortices wrapped around the roughness and downstream of the roughness formed pairs of counter–rotating streamwise vortices referred to as the Symmetry Plane (SP) and Off–Symmetry Plane (OSP) vortices. Since the roughness height was larger for both the Mach 3.37 and 5.26 flows which transition, we study the effect of boundary layer thickness in this Chapter to understand how the roughness affects the flow when its height is smaller than the boundary layer thickness of the incoming boundary layer.

The effect of boundary layer thickness is studied for a Mach 3.37 boundary layer flow. The flow conditions are identical to the Mach 3.37 flow in Chapter 4, except that the free–stream Reynolds number ($Re_k = u_\infty k/\nu_\infty$) is halved. We choose $Re_k = u_\infty k/\nu_\infty$=4560 with the wall maintained at a constant temperature of $300K$ and with a free–stream temperature $T_\infty = 340.4819$ K. The free-stream velocity and density are

$u_\infty = 1217.57\ m/s$ and $\rho_\infty = 0.0786\ km/m^3$ respectively, same as the Mach 3.37 flow in Chapter 4 and the experiments of Danehy *et al.* [19]. The reduction in Re_k by a factor of 2 is equivalent to having the diameter (D) of the roughness element to be 2 mm as opposed to 4 mm.

The schematic of the problem is shown in Figure 4.1 in Chapter 4. All variables are non–dimensionalized with their free–stream values and all lengths with the diameter of the roughness (D). The domain extends $50D$ in the streamwise direction (x), 40 D in the spanwise direction (z) and 20 D in the wall normal direction (y). The bump is located at x=15 D from the inflow plane. A compressible similarity solution is prescribed at the inflow. Zero gradient conditions are used at the outflow, top wall and side walls. A non–reflecting boundary condition is used on all boundaries (excluding the flat plate) to remove any acoustic reflections.

The computational mesh is unstructured and consists of 16 million elements. The grid used for this problem is the same as the coarsest grid used in Chapter 4. Since it was found in the grid convergence study in Section 4.3 that the solution is not too sensitive between the coarsest and fine grids, and since the Re_k used in this study is lower by a factor of 2, the coarse grid was used in this study. A minimum wall spacing (Δy_{min}) of 0.01 and a spanwise spacing of $\Delta z = 0.066$ was used in the vicinity of the roughness element. The streamwise spacing was finer closer to the roughness with a $\Delta x = 0.07$ and 0.11 at $x = 5$ and 15 D downstream respectively.

k/δ	Re_x	Re_θ	Re_k
2.54	91207.7	193.08	4560
1.0	5.472×10^5	473.94	4560
0.25	8.738×10^6	1894.38	4560
0.125	34.883×10^6	3786.03	4560

Table 5.1: Parameters for flow past discrete hemispherical bump at Mach 3.37 with varying inflow boundary layer thickness.

To study the effect of boundary layer thickness on the transition mechanism for a laminar Mach 3.37 boundary layer, four values of k/δ (Table 5.1) are considered, where k is the roughness height and δ is the boundary layer thickness of the laminar boundary

layer at the location of the roughness if it were absent. Inflow boundary layer conditions are prescribed from the compressible similarity solution such that the corresponding k/δ is obtained at the location of the roughness. The corresponding Re_x and Re_θ for the laminar boundary layer at the location of the roughness are specified in Table 5.1 where x is the distance from the leading edge of the flat plate. Note that for the $k/\delta = 0.125$ flow, where the $Re_\theta = 3786.03$, it is possible that natural transition could have set in. We, however, assume that the boundary layer is laminar at the inflow of the domain to isolate the effect of boundary layer thickness, keeping all other flow parameters constant.

Instantaneous density contours for the four cases in the symmetry plane are shown in Figure 5.1. Note that all four cases appear transitional downstream of the roughness. Upstream of the bump, the difference in boundary layer thickness is clearly seen in the figure for the four cases. The shock produced due to the roughness is visible for all the flows, with the $k/\delta = 2.54$ flow having the strongest shock due to higher local Mach number at the height of the roughness. For the higher k/δ cases, the entire boundary layer appears transitional at the farthest streamwise station in the figure, whereas for the lower k/δ cases, it appears that the disturbance has not fully reached the boundary layer edge.

5.2 Results

5.2.1 Upstream separation

The laminar boundary layer separates upstream of the bump giving rise to a system of spanwise vortices as shown in Figure 5.2. Instantaneous streamlines are plotted in the symmetry plane. It can be seen that with decreasing k/δ, the separation length decreases. This can be understood by a simple scaling argument. Consider a point close to the flat plate upstream of the bump. Since the wall condition is same for all four cases, the density at the chosen point would also roughly be the same. Its momentum would scale with the local u velocity while the pressure difference would roughly scale with $u\partial u/\partial x$. Since the local u is lower for a larger δ, the pressure difference relative to the momentum is going to be lower for the larger δ case thereby allowing the flow to separate later.

From the Figure, note that the number of vortices upstream is different for the four

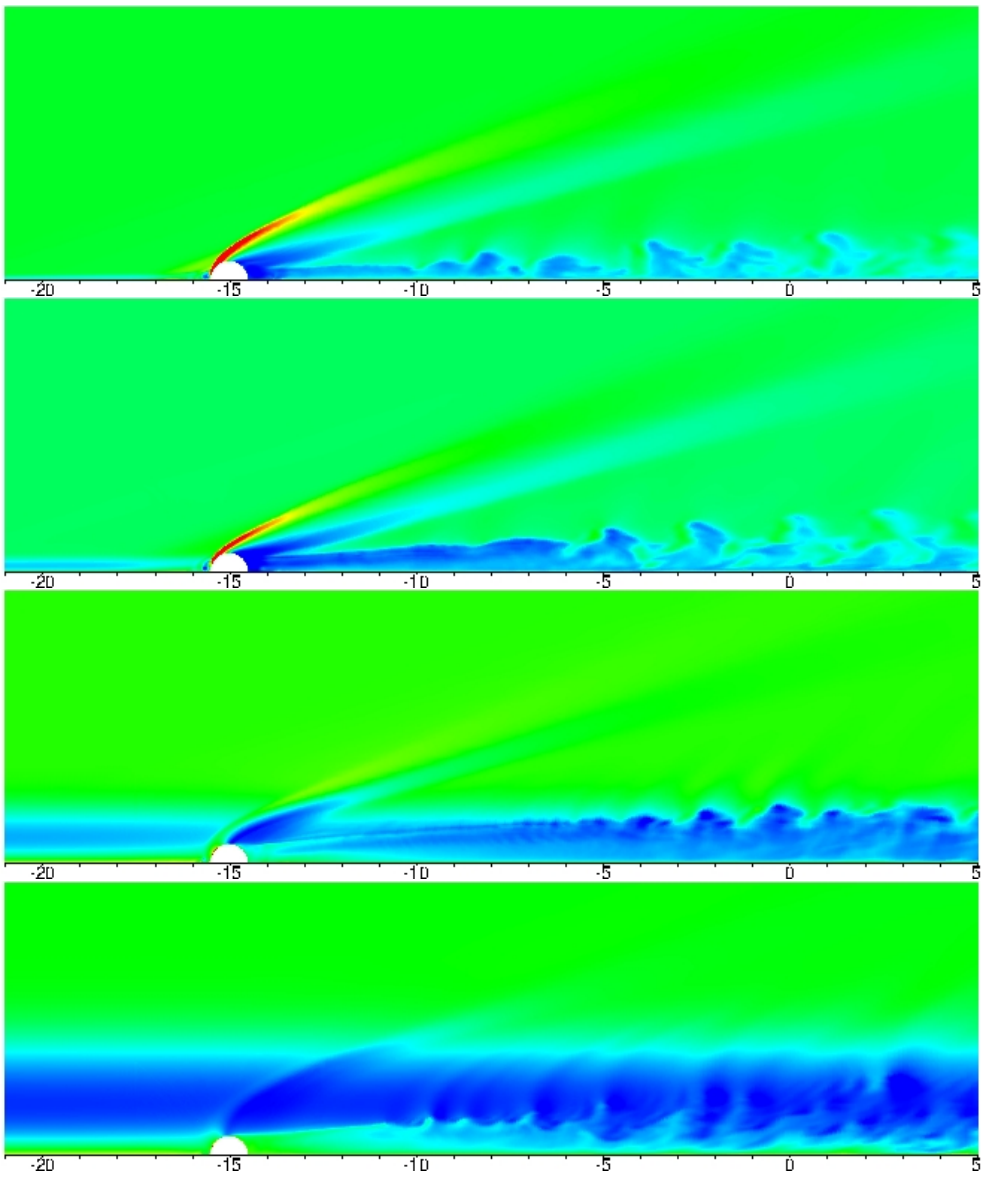

Figure 5.1: Instantaneous density contours in the z =0 symmetry plane for $k/\delta = 2.54$, 1.0, 0.25 and 0.125 from top to bottom.

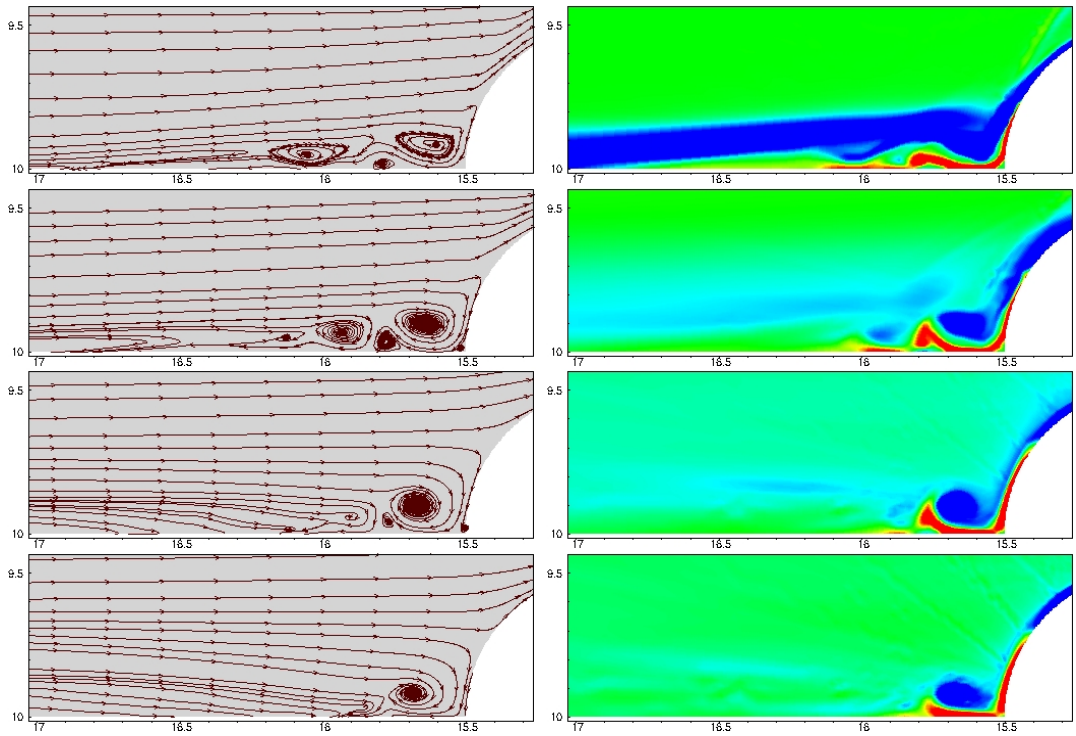

Figure 5.2: Instantaneous streamlines (left) and ω_z contours (right) in the z =0 symmetry plane upstream of the bump for k/δ =2.54,1.0,0.25 and 0.125 (top to bottom).

cases with the larger k/δ cases having more vortices. This is in qualitative agreement with the result of Baker [3], who studied the flow past a cylindrical protuberance at incompressible speeds and found that at a fixed Re_k, a higher k/δ gives rise to more separation vortices upstream. From the figure, we see that the length scale of the primary vortex (largest vortex) is roughly the same for all four cases i.e. the approximate location on the bump at which streamlines separate is roughly the same. Thus, it appears that the length scale of the upstream vortices is more a function of the shape of the roughness element.

Also shown in Figure 5.2 are the instantaneous spanwise vorticity (ω_z) contours to indicate the strength of the vortices. Note that the color scheme used is different for all cases and that the strength of the vortices decreases with decreasing k/δ. Note that the strength of the spanwise vorticity of the vortex closest to the bump upstream is comparable to the boundary layer for $k/\delta = 2.54$ but is increasingly higher than the

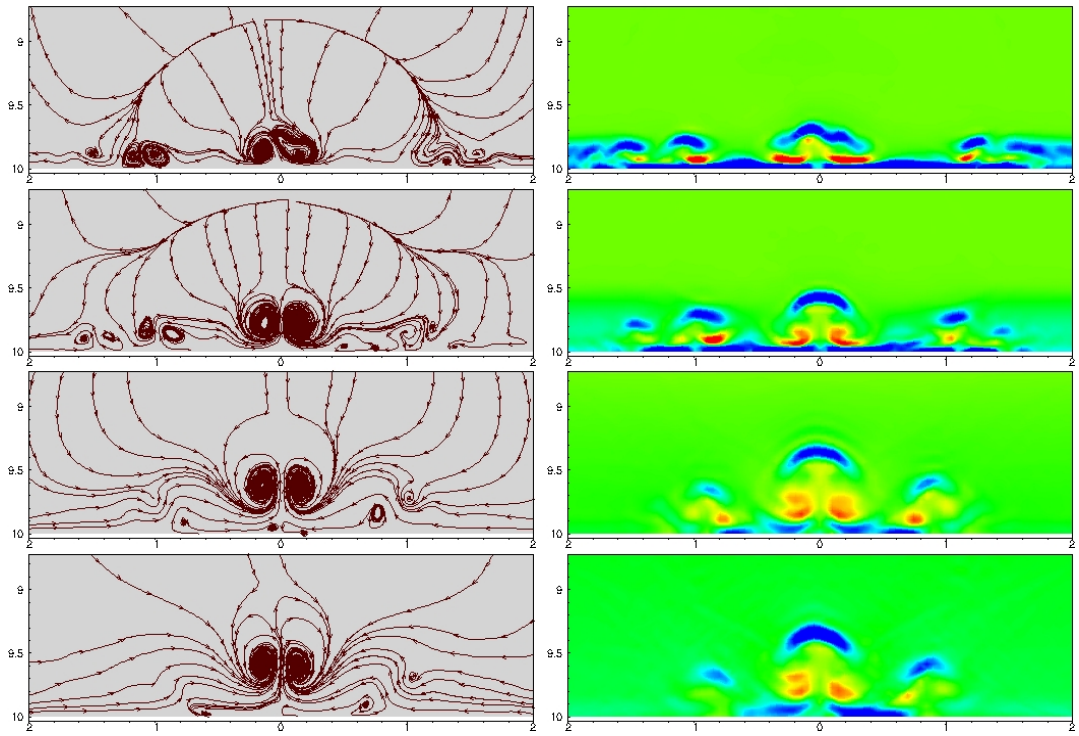

Figure 5.3: Instantaneous streamlines (left) and ω_x contours (right) at x =2D downstream of the bump for k/δ =2.54,1.0,0.25 and 0.125 (top to bottom).

boundary layer vorticity for the lower k/δ flows. The spanwise vortices wrap around the bump producing a system of counter-rotating streamwise vortices downstream of the bump.

5.2.2 Perturbation of the shear layer by streamwise vortices

Figure 5.3 shows instantaneous streamlines and ω_x contours at a plane 2D downstream of the center of the bump. Counter-rotating streamwise vortices are formed close to the symmetry plane (SP vortices) and away from the symmetry plane on either side (OSP vortices). Depending on their strength and sense of rotation, the streamwise vortices move closer or away from the symmetry plane due to the induced velocity from the mirror vortices below the flat plate. The counter-rotating vortices can have a net upwash or downwash depending on their sense of rotation. From Figure 5.3, it can be seen that both the SP and OSP counter-rotating vortex pairs have a net upwash i.e.

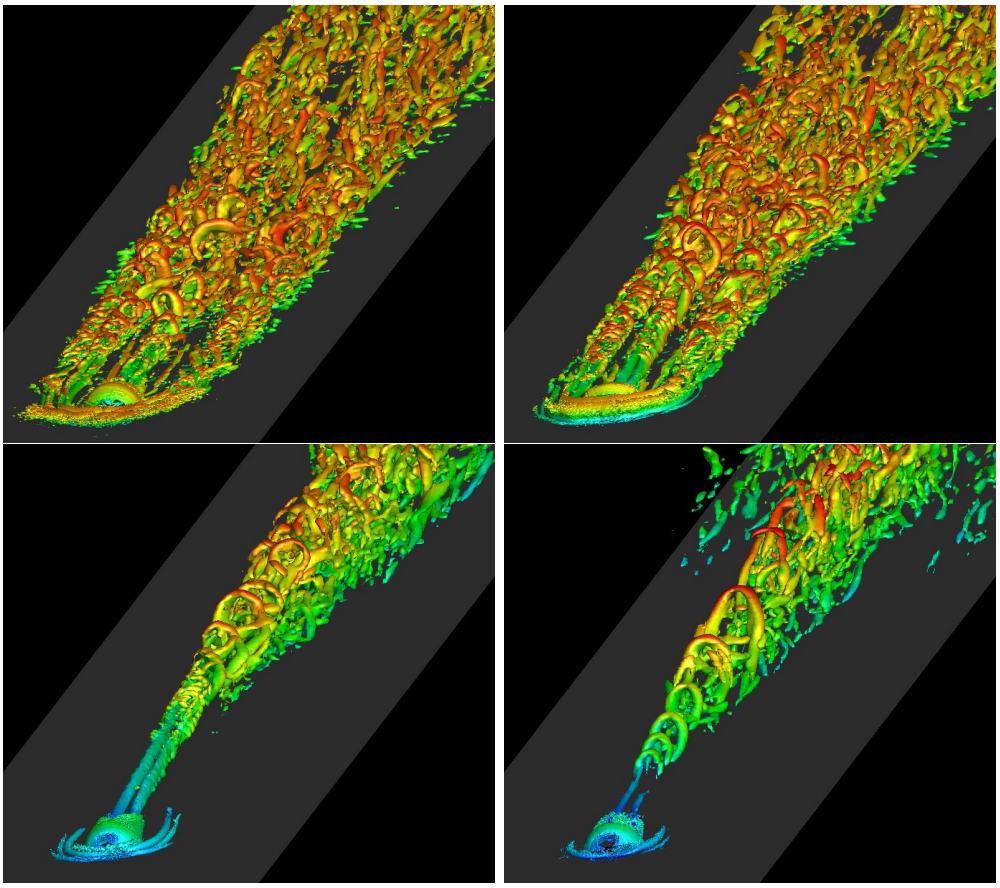

Figure 5.4: Iso-contour of Q criterion plots colored by streamwise velocity showing hairpin vortices for $k/\delta = 2.54$ (top-left), 1.0 (top-right), 0.25 (bottom-left) and 0.125 (bottom-right). The hairpin vortices are clearly seen in all cases. With decreasing k/δ, only a single train of hairpin vortices are observed behind the roughness element.

they perturb the shear layer above them. The center of the symmetry plane vortices moves away from the flat plate with decreasing k/δ. This could be due to the fact that the induced velocity by the counter rotating vortex relative to the streamwise velocity at that downstream location is higher for the lower k/δ cases.

5.2.3 Coherent hairpin shaped vortices

The streamwise vortices perturb the shear layer above it as seen in Figure 5.3 resulting in the shedding of hairpin-shaped vortices. Iso-contours of the Q criterion in Figure 5.4

shows the hairpin-shaped vortices produced downstream of the roughness. Closer to the bump, the location of the hairpin vortices correspond to the location of counter-rotating streamwise vortices. Farther downstream, the trains of hairpin vortices give rise to secondary vortices resulting in the spanwise spreading of the vortices. Note that for k/δ=2.54 and 1.0, three trains of hairpin vortices are observed closer to the roughness while for smaller k/δ cases, a single train of hairpin vortices is observed. This can be attributed to the fact that the secondary spanwise vortex upstream of the bump was weak for the smaller k/δ cases, resulting in weak counter-rotating streamwise vortices away from the symmetry plane, thereby not perturbing the shear layer enough to shed hairpin vortices.

These hairpin vortices cause an increase in the wall skin friction and heat transfer by transporting higher momentum fluid towards the wall and lower momentum fluid away from the wall. For $k/\delta = 0.25, 0.125$, it can be seen that the height of the hairpin vortex is initially of the order of the roughness height, but with increasing distance downstream, it becomes larger and appears to scale with the boundary layer thickness. The rising of the hairpin head with downstream distance could be due to the fact that the central portion of the hairpin has vorticity which induces a net upward velocity similar to the streamwise cut seen in figure 5.3. The hairpin vortices appear more coherent closer to the bump and become less coherent with increasing downstream distance especially for the larger k/δ cases.

5.2.4 Dynamic Mode Decomposition analysis

Dynamic Mode Decomposition of the three-dimensional pressure field, described in Appendix A, was performed for $k/\delta = 1$ and 0.125 respectively. 80 and 160 snapshots were used for $k/\delta = 1$ and 0.125 respectively, with a spacing of $\Delta t D/u_\infty = 0.25$. Figure 5.5 (a) shows the variation of energy with $St = fD/u_\infty$ from DMD for $k/\delta = 1$. It is seen that there is a very low frequency mode that is most dominant for this flow. We however, plot the iso-contours of pressure of the $St = 0.30$ DMD mode for $k/\delta = 1$ in Figure 5.5 (c) which corresponds to the hairpin vortices downstream of the roughness element. At $St = 0.30$, a local peak can been seen from the energy plot in Figure 5.5 (a). It can be seen that hairpin vortices are dominant at both the symmetry plane and off-symmetry plane and oscillate with the same frequency.

Figure 5.5 (b) shows the variation of energy with $St = fD/u_\infty$ from DMD for $k/\delta = 0.125$. It is seen that $St = 0.088$ mode is most dominant for this flow. The frequency matches the observed shedding frequency from the animation of the flowfield. The iso-contours of pressure of the $St = 0.088$ DMD mode for $k/\delta = 0.125$ is shown in Figure 5.5 (d). Coherent hairpin vortices are observed with increasing size with distance away from the roughness element. Thus, DMD can be used to obtain the frequency of shedding of hairpin vortices.

5.2.5 Reynolds number for predicting transition

In Section 4.5.8, it was seen that the Reynolds number based on wall properties correlates transition better when compared to a Reynolds number based on free-stream properties. We evaluate $Re_{k,wall} = u_k k/\nu_{wall}$ for the four k/δ studied in this Chapter. We list the values of the commonly used Re_k and $Re_{k,wall}$ in Table 5.2. Note that the trends for Re_k and $Re_{k,wall}$ are similar for the cases simulated since the wall condition is identical. However, we see that $Re_{k,wall}$ is unable to differentiate the effect of k/δ when the values are greater than or equal to 1. Thus, we now define the Reynolds number based on the wall shear which is characterized by the skin friction velocity at the wall ($u_\tau = \sqrt{\tau_w/\rho_w}$). The wall shear decreases with increasing δ for the same free-stream and wall conditions and and since u_τ is sensitive for all values of k/δ as opposed to u_k which becomes 1 when k/δ is greater than or equal to one, the Reynolds number based on the skin friction velocity and wall properties ($Re_{k,\tau}$) would correlate transition better than $Re_{k,wall}$.

k/δ	$Re_k = u_k k/\nu_\infty$	$Re_{k,wall} = u_k k/\nu_{wall}$	$Re_{k,\tau} = u_\tau k/\nu_{wall}$
2.54	**4560**	**5682**	**175.1**
1.0	**4560**	**5682**	**111.2**
0.25	1915	2386	55.9
0.125	1067	1330	39.3

Table 5.2: Table showing Re_k, $Re_{k,wall} = \frac{u_\infty k}{\nu_w}$ and $Re_{k,\tau} = u_\tau k/\nu_{wall}$ for the cases simulated.

5.3 Conclusions

The effect of boundary layer thickness (δ) of the incoming boundary layer was studied keeping all other parameters constant for Mach 3.37 flow. The differences in the flow features observed due to a larger boundary layer thickness is discussed. Four cases are considered where $k/\delta = 2.54$, 1, 0.25 and 0.125, where k is the height of the roughness and δ is the laminar boundary layer thickness at the location of the roughness. Transition is observed for all the four cases studied. It is seen that when the boundary layer thickness is less than or equal to the roughness height ($k/\delta = 2.54$, 1), stronger upstream separation is observed giving rise to a larger number of upstream vortices. The upstream separation vortices are weaker as the boundary layer thickness is increased. The mechanism of transition is similar for all cases, where the counter–rotating streamwise vortices perturb the shear layer above, giving rise to trains of hairpin vortices. It is seen that a single train of hairpin vortices are observed immediately downstream of the roughness for the larger boundary layer thickness cases ($k/\delta = 0.25$ and 0.125), while multiple trains of hairpin vortices are observed for the smaller boundary layer thickness cases ($k/\delta = 2.54$ and 1). Also, the hairpin vortices formed downstream of the roughness element initially scale with the height of the roughness, and with increasing downstream distance, spread across the entire boundary layer and scale with the boundary layer thickness. DMD of the pressure field for k/δ of 1 and 0.125 showed prominent hairpin vortices and their shedding frequency. A Reynolds number based on the skin friction velocity of the unperturbed boundary and the wall properties was seen to be a better indicator of transition as compared to using the velocity at the height of the roughness as a reference.

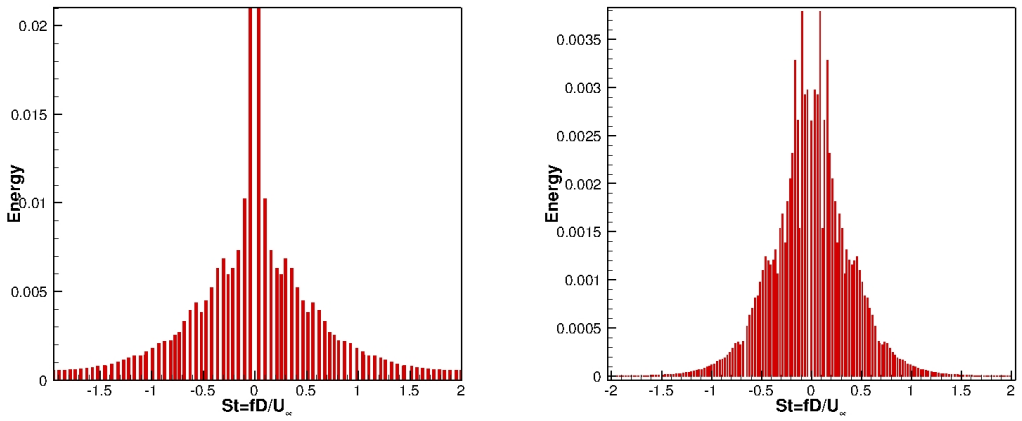

(a) (b)

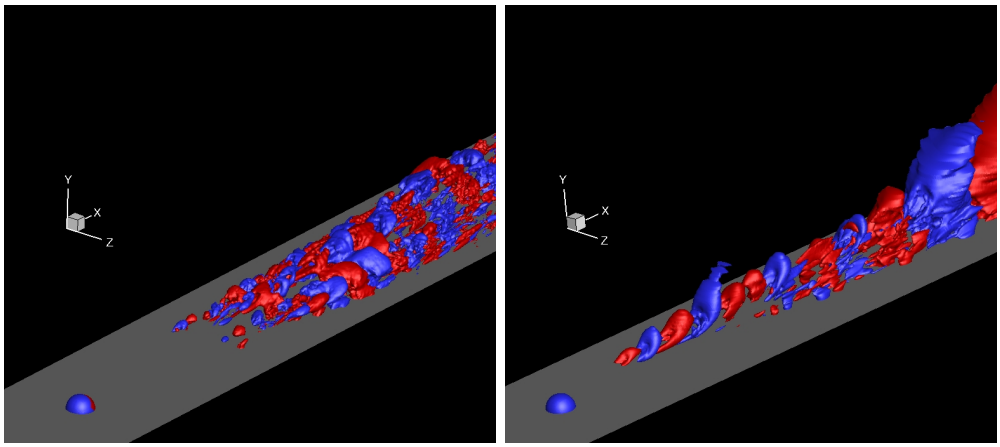

(c) (d)

Figure 5.5: Results from the Dynamic Mode Decomposition of the pressure field for $k/\delta = 1$ and 0.125. The energy from DMD is shown in (a) and (b) for $k/\delta = 1$ and 0.125 respectively. Iso-contours of pressure of the $St = 0.30$ mode for $k/\delta = 1$ is shown in (c) while the same for $St = 0.088$ mode for $k/\delta = 0.125$ is shown in (d).

Chapter 6

Conclusion and Discussion

This dissertation studies the effects of a discrete roughness element on a high–speed laminar boundary layer. Free–stream Mach numbers ranging from 3.37 to 8.23 are studied. It is found that for the range of conditions studied, the lower Mach number flows transition downstream of the roughness while the higher Mach number flows remain laminar. The algorithm was first validated with a linear stability code for a supersonic Couette flow and a supersonic boundary layer to demonstrate its ability to study transition problems. A Mach 8.12 boundary layer flow past a cylindrical roughness element was simulated at conditions matching Bathel *et al.* [7] to validate the algorithm used. While overall, good agreement was obtained with experiment, some differences were found in the vicinity of the roughness. Hence, the effect of time delay, laser sheet position and effect of upstream injection were reported to understand the reasons for the differences between the DNS and experiment at certain locations. Due to the injection of NO in the experiment for the measurement which increases the boundary layer thickness of the flow, it was found to be more appropriate to compare velocity profiles with the wall–normal co–ordinate scaled with the local boundary layer thickness.

The roughness element causes the boundary layer to separate upstream giving rise to a system of spanwise vortices where the number of vortices upstream depends on the flow conditions. The spanwise vortices wrap around the roughness element and form counter–rotating streamwise vortices in the streamwise plane downstream of the roughness. These counter–rotating vortices can be oriented so as to have a net upwash or downwash between them. When they have a net upwash, they move towards each

other due to the induced velocity from the image vortices, thus becoming stronger and perturb the shear layer above it. On the other hand, when they have a net downwash between them, they become weaker with increasing downstream distance and are less likely to cause transition. It was observed that for Mach 3.37 and 5.26 flows that undergo transition, the counter–rotating vortices had a net upwash between them while for the Mach 8.23 flow, they had a net downwash. The perturbation of the shear layer by the counter–rotating vortices gives rise to hairpin shaped vortices which induce three-dimensionality into the flow and with increasing downstream distance cause the flow to become turbulent. Comparison of turbulent statistics for the Mach 3.37 and 5.26 flows with available turbulent boundary layer data showed good agreement indicating that the boundary layer is turbulent. The mechanism of formation of hairpin vortices for the conditions studied in this dissertation is different from those observed in low–speed literature (Acarlar & Smith [1]), where the hairpin vortices were directly shed from the roughness element. Two–dimensional simulations under high and low–speed conditions, keeping all other parameters constant showed that there was no absolute vortex shedding at high–speed while discrete vortices were shed at low–speed, consistent with the observations of Chang & Choudhari [12].

The simulations of a Mach 3.37 boundary layer with varying incoming boundary layer thickness (δ) was studied keeping all other parameters constant. It was seen that coherent hairpin vortices were formed for all the cases simulated. The number of spanwise vortices upstream of the roughness was lower for the larger δ flows due to a smaller separation length. Thus, the counter–rotating vortices downstream of the roughness was weaker away from the symmetry plane. Thus, a single train of hairpin vortices was observed in the symmetry plane for the larger δ flows while multiple trains of hairpin vortices were formed for lower δ flows. The hairpin vortices initially scaled with the height of the roughness element, but with increasing downstream distance, scaled with the boundary layer thickness. Dynamic Mode Decomposition of the pressure field was used to obtain the frequency of shedding of hairpin vortices and a Reynolds number based on skin friction velocity of the unperturbed boundary layer and wall conditions correlated the trend of transition for Mach 3.37.

References

[1] Acarlar, M. S. & Smith, C. R. 1987 A study of hairpin vortices in a laminar boundary layer. Part 1. Hairpin vortices generated by a hemispherical protuberance. *J. Fluid Mech.* **175**, 1–41.

[2] Adrian, R. J. 2007 Hairpin vortex organization in wall turbulence. *Phys. Fluids* **19**, 041301.

[3] Baker, C. J. 1979 The laminar horseshoe vortex. *J. Fluid Mech.* **95**, 347–367.

[4] Berry, S. A., Horvath, T. J., Cassady, A. M., Kirk, B. S., Wang, K. C. & Hyatt, A. J. 2006 Boundary Layer Transition Results From STS-114. *AIAA Paper* 2006–2922.

[5] Subbareddy, P. K., Bartkowicz, M. D. & Candler, G. V. 2014 Direct numerical simulation of high-speed transition due to an isolated roughness element. *J. Fluid Mech.* **748**, 848–878. i

[6] Bagheri, S. 2013 Koopman–mode decomposition of the cylinder wake. *J. Fluid Mech.* **726**, 596–623.

[7] Bathel, B. F., Danehy, P. M., Inman, J. A., Watkins, A. N., Jones, S. B., Lipford, W. E., Goodman, K. Z., Ivey, C. B. & Goyne, C. P. 2010 Hypersonic Laminar Boundary Layer Velocimetry with Discrete Roughness on a Flat Plate. *AIAA Paper* 2010–4998.

[8] Beresh, S. J., Henfling, J. F., Erven, R. J., & Spillers, R. W. 2005 Penetration of a transverse supersonic jet into a subsonic compressible crossflow. *AIAA J.* **43**(2), 379–389.

[9] Beresh, S. J., Henfling, J. F., Spillers, R. W. & Pruett, B. O. M. 2011 Fluctuating wall pressures measured beneath a supersonic turbulent boundary layer. *Phys. Fluids* **23**,075110.

[10] Butler, K. M. & Farrell, B. F. 1992 Three-dimensional optimal perturbations in viscous shear flow. *Phys. Fluids A* **4**,1637.

[11] Chai, X., & Mahesh, K. 2011 Simulations of High Speed Turbulent Jets in Crossflows. *AIAA Paper* 2011–650.

[12] Chang, C. & Choudhari, M. M. 2009 Hypersonic Viscous Flow over Large Roughness Elements. *AIAA Paper* 2009–0173.

[13] Chen, K. K., Tu, J. K. & Rowley, C. W. 2012 Variants of dynamic mode decomposition: boundary condition, Koopman, and Fourier analyses. *J. Nonlinear Science* **22**, 887–915.

[14] Choi, H. & Moin, P. 1990 On the space-time characteristics of wall-pressure fluctuations. *Phys. Fluids A* **2**,1450.

[15] Choudhari, M. M., Li, F., Wu, M., Chang, C., Edwards, J., Kegerise, M. & King, R. 2010 Laminar-Turbulent Transition behind Discrete Roughness Elements in a High-Speed Boundary Layer. *AIAA Paper* 2010–1575.

[16] Coleman, G. N., Kim, J. & Moser, R. D. 1995 A numerical study of turbulent supersonic isothermal-wall channel flow. *J. Fluid Mech.* **305**,159–183.

[17] Colonius, T. 2009 Modeling artificial boundary conditions for compressible flow. *Ann. Rev. Fluid Mech.* **36**, 315–345.

[18] Danehy, P. M. 2010 Personal Communication.

[19] Danehy, P. M., Bathel, B., Ivey, C., Inman, J. A. & Jones, S. B. 2009 NO PLIF study of hypersonic transition over a discrete hemispherical roughness element.*AIAA Paper* 2009–394.

[20] Danehy, P. M., Garcia, A. P., Borg, S., Dyakonov, A. A., Berry, S. A., Inman, J. A. & Alderfer, D. W. 2007 Fluorescence visualization of hypersonic flow past triangular and rectangular boundary-layer trips. *AIAA Paper* 2007–0536.

[21] Danehy, P. M., Ivey, C. B., Inman, J. A., Bathel, B. F., Jones, S. B., McCrea, A. C., Jiang, N., Webster, M., Lempert, W., Miller, J. & Meyer, T. 2010 High–Speed PLIF Imaging of Hypersonic Transition over Discrete Cylindrical Roughness. *AIAA Paper* 2010–703.

[22] Dryden, H. L. 1953 Review of published data on the effect of roughness on transition from laminar to turbulent flow. *J. Aeronaut. Sci.* **20**, 477–482.

[23] Duan, L., Beekman, I. & Martin, M. P. 2010 Direct numerical simulation of hypersonic turbulent boundary layers. Part 2. Effect of wall temperature. *J. Fluid Mech.* **655**, 419–445.

[24] Dong, H., & Zhong, X. 2002 High-order semi-implicit schemes for unsteady compressible flow simulations. *AIAA J.*, Volume **40** (5), 869–878.

[25] Ergin, F. G. & White, E. B. 2006 Unsteady and Transitional Flows Behind Roughness Elements. *AIAA J.*, Volume **44** (11), 2504–2514.

[26] Gibson, D. M., Spisz, T. S., Taylor, J. C., Zalameda, J. N., Horvath, T. J., Tomek, D. M., Tietjen, A. B., Tack, S. & Bush, B. C. 2010 HYTHIRM Radiance Modeling and Image Analyses in Support of STS-119, STS-125 and STS-128 Space Shuttle Hypersonic Re–entries. *AIAA Paper* 2010–245.

[27] Groskopf, G., Kloker, M. J. & Marxen, O. 2008 Bi-global secondary stability theory for high-speed boundary layer flows. *Proceedings of the Summer Program, Center for Turbulence Research*.

[28] Head, M. R. & Bandyopadhyay, P. 1981 New aspects of turbulent boundary-layer structure. *J. Fluid Mech.* **107**, 297–338.

[29] Hunt, J. C. R., Wray, A. A. & Moin, P. 1988 Eddies, stream, and convergence zones in turbulent flows. *Tech. Rep. CTR-S88., Center for Turbulence Research*.

[30] Klebanoff, P. S., Cleveland, W. G. & Tidstrom, K. D. 1992 On the evolution of a turbulent boundary layer induced by a three-dimensional roughness element. *J. Fluid Mech.* **237**, 101–187.

[31] Lees, L. & Lin, C. C. 1946 Investigation of the Stability of the Laminar Boundary Layer in a Compressible Fluid. *National Advisory Committee for Aeronautics , Washington, D. C*

[32] Mack, L. M. 1984 Boundary-layer linear stability theory. *AGARD Spec. Course on Stability and Transition of Laminar Flow*

[33] Malik, M. R. 1990 Numerical methods for hypersonic boundary layer stability. *J. of Comp. Phys.*, Volume **86** (2), 376–413.

[34] Marxen, O., Iaccarino, G. & Shaqfeh, E. S. G. 2010 Disturbance evolution in a Mach 4.8 boundary layer layer with two-dimensional roughness-induced separation and shock. *J. Fluid Mech.* **648**, 435–469.

[35] Megerian, S., Davitian, J., Alves, L. S. B. & Karagozian, A. R. 2007 Transverse–jet shear–layer instabilities. Part 1. Experimental studies. *J. Fluid Mech.* **593**, 93–129.

[36] Mason, P. J. & Morton, B. R. 1987 Trailing vortices in the wakes of surface-mounted obstacles. *J. Fluid. Mech.* **175**, 247–293.

[37] Moin, P. & Mahesh, K. 1998 Direct numerical simulation: a tool in turbulence research. *Ann. Rev. Fluid Mech.* **30**, 539–578.

[38] Morkovin, M. V., Reshotko, E. & Herbert, T. 1994 Transition in Open Flow Systems: A Reassessment. *Bulletin of the American Physical Society* **39-9**, 1882.

[39] Muppidi, S., & Mahesh, K. 2010 DNS of transition in supersonic boundary layers. *AIAA Paper* 2010–4440.

[40] Muppidi, S., & Mahesh, K. 2011 DNS of unsteady shock boundary layer interaction. *AIAA Paper* 2011–724.

[41] Muppidi, S., & Mahesh, K. 2012 Direct numerical simulations of roughness-induced transition in supersonic boundary layers. *J. Fluid. Mech.* **693**, 28–56.

[42] Mussoni, E., Iyer, P. & Mahesh, K. 2012 DNS of the transition from absolute to convective instability for transverse jets. *65th Annual Meeting of the APS Division of Fluid Dynamics*, San Diego, California, USA.

[43] Park, N. & Mahesh, K. 2007 Numerical and modeling issues in LES of compressible turbulent flows on unstructured grids. *AIAA Paper* 2007–722.

[44] Pirozzoli, S. & Grasso, F. 2006 Direct numerical simulation of impinging shock waveturbulent boundary layer interaction at M = 2.25. *Phys. Fluids* **18**, 065113.

[45] Reda, D. C. 2002 Review and Synthesis of Roughness-Dominated Transition Correlations for Reentry Applications. *J. Spacecraft and Rockets* **39** Issue 2, 161–167.

[46] Redford, J. A., Sandham, N. D. & Roberts, G. T. 2010 Compressibility effects on boundary-layer transition induced by an isolated roughness element. *AIAA J.* **48** (12), 2818–2830.

[47] Reshotko, E. 2001 Transient growth: A factor in bypass transition. *Phys. Fluids* **13**, 1067.

[48] Reshotko, E. 2007 Is Re_θ/M_e a Meaningful Transition Criterion? *AIAA Paper* 2007–943.

[49] Reshotko, E. & Tumin, A. 2004 Role of Transient Growth in Roughness-Induced Transition. *AIAA J.* **42** (4), 766–770.

[50] Rowley, C. W., Mezic, I., Bagheri, S., Schlatter, P. & Henningson, D. S. 2009 Spectral analysis of nonlinear ows. *J. Fluid Mech.* **641**, 115–127.

[51] Sakamoto, H. & Haniu, H. 1995 The formation mechanism and shedding frequency of vortices from a sphere in uniform shear flow. *J. Fluid. Mech.* **287**, 151–171.

[52] Santiago, J. G. & Dutton, J. C. 1997 Velocity measurements of a jet injected into a supersonic crossflow. *Journal of propulsion and power* **13** (2), 264–273.

[53] Saric, W. S. 1994 Gortler Vortices. *Ann. Rev. Fluid Mech.* **26**, 379–409.

[54] Saric, W. S., Reed, H. L. & White, E. B. 2003 Stability and Transition of Three-Dimensional Boundary Layers. *Ann. Rev. Fluid Mech.* **35**, 413–440.

[55] Schmid, P. J. 2010 Dynamic mode decomposition of numerical and experimental data. *J. Fluid Mech.* **656**, 5–28.

[56] Schmid, P. & Sesterhenn, J. 2008 Dynamic mode decomposition of numerical and experimental data. *61st Annual Meeting of the APS Division of Fluid Dynamics*, San Antonio, Texas, USA.

[57] Schneider, S. P. 2008 Effects of Roughness on Hypersonic Boundary-Layer Transition. *J. of Spacecraft and Rockets* **45** (2), 193–209.

[58] Schlichting, H. 1968 Boundary–layer theory.

[59] Simpson, R. L. 2001 Junction Flows. *Ann. Rev. Fluid Mech.*, **33**, 415–443.

[60] Spalart, P. R. 1988 Direct simulation of turbulent boundary layer up to $R_\theta = 1410$. *J. Fluid Mech.* **187**, 61–98.

[61] Tani, I., Komoda, H., Komatsu, Y. & Iuchi, M. 1962 Boundary-Layer Transition by Isolated Roughness. *Aeronautical Research Institute, University of Tokyo* Report No. **375**.

[62] Theofilis, V. 2011 Global Linear Instability. *Ann. Rev. Fluid Mech.* **43**, 319–352.

[63] Tritton, D. J. 1959 Experiments on the flow past a circular cylinder at low Reynolds numbers. *J. Fluid Mech.* **6**, 547–567.

[64] Tumin, A. & Reshotko, E. 2005 Receptivity of a boundary-layer flow to a three-dimensional hump at finite Reynolds numbers. *Phys. Fluids* **17**, 094101.

[65] Wheaton, B. & Schneider, S. P. 2010 Roughness-Induced Instability in a Laminar Boundary Layer at Mach 6. *AIAA Paper* 2010–1574.

[66] Wu, X. &, Moin, P. 2009 Direct numerical simulation of turbulence in a nominally zero-pressure-gradient flat-plate boundary layer. *J. Fluid Mech.* **630**, 5–41.

[67] Yee, H. C., Sandham, N. D., & Djomehri, M. J. 1999 Low-dissipative high-order shock-capturing methods using characteristic-based filters. *J. of Comp. Phys.*, Volume **150** (1), 199–238.

[68] Hou, Y. 2007 A novel algorithm for DNS/LES of compressible turbulent flows. *Doctoral Dissertation, University of Minnesota.*

[69] Zhong, X. 1998 High-order finite-difference schemes for numerical simulation of hypersonic boundary-layer transition. *J. of Comp. Phys.*, Volume **144** (2), 662–709.

[70] Zhong, X. & Wang, X. 2012 Direct Numerical Simulation on the Receptivity, Instability, and Transition of Hypersonic Boundary Layers. *Ann. Rev. Fluid Mech.* **44**, 527–561.

Appendix A

Dynamic Mode Decomposition of complex flows

A.1 Introduction

Dynamic Mode Decomposition (DMD) refers to the frequency based decomposition of a flowfield and was first proposed by Schmid & Sesterhenn[56]. It is analogous to a Fourier transform of the full spatial flowfield. It can be used to extract the flow features oscillating at a particular frequency to better understand the flowfield, instead of placing individual probes at various different locations in the flow to extract the time history of flow variables. Its application has been demonstrated by Schmid[55] for a plane channel flow, flow past a two-dimensional cavity, wake flow behind a flexible membrane and a jet passing between two cylinders. Rowley *et al.*[50] showed that DMD is an approximation of the Koopman operator for a given system and applied it to a three-dimensional jet in crossflow problem, where they observe two dominant frequencies in the flow which correspond to the jet shear layer roll up and a boundary layer mode respectively. The current work applies the DMD algorithm to large unstructured datasets (upto 80 million grid points). This chapter briefly summarizes the algorithm and is validated for the flow past a cylinder at low Reynolds numbers. The algorithm is then tested on three complex problems: low speed jet in crossflow, sonic jet in a supersonic crossflow and a supersonic jet in subsonic crossflow.

A.2 Algorithm

We follow the method of Rowley *et al.*[50] and Schmid[55] to perform Dynamic Mode Decomposition (also referred to as Koopman mode decomposition) of the three–dimensional flow–field. We store $(m+1)$ snapshots of the three velocity components (or pressure) at each spatial location and express the last snapshot as a linear combination of the previous snapshots. The size of each x_i vector is the number of grid points multiplied by the number of velocity components (or any other flow variable used). Note that this method is generic and can be used for any flow variable or combination. Let K represent a matrix of the different snapshots from x_0 to x_{m-1},

$$K = [x_0, x_1, x_2, ...x_{m-1}] \tag{A.1}$$

Since each snapshot (x_i) is obtained from application of the discrete Navier–Stokes operator (represented by the matrix A) to the previous snapshot (x_{i-1}), the matrix K can also be written as:

$$K = [x_0, Ax_0, A^2x_0, ...A^{m-1}x_{m-1}] \tag{A.2}$$

Now, expressing the last snapshot (x_m) as a linear combination of the previous snapshots,

$$x_m = c_0x_0 + c_1x_1 + c_2x_2 + ...c_{m-1}x_{m-1} + r = Kc + r \tag{A.3}$$

In the above equation, r represents the residual of the linear combination. If the matrix A were linear, then the above representation would be exact, thus making the residual zero. Since the Navier–Stokes operator is non–linear, there is a finite residual and the decomposition approximates the eigenvalues of the matrix A. Here, c is given by :

$$c = (c_0, c_1, c_2, ...c_{m-1})^T \tag{A.4}$$

The vector c is obtained by solving the Least-Squares problem in Equation A.3 using Singular Value Decomposition (SVD). Based on the above definitions, we get :

$$AK = KC + re^T, e^T = (0, 0, ...1) \tag{A.5}$$

where C is a companion matrix whose eigenvalues approximate those of the matrix A, which represents the dynamics of the flow. The imaginary part of the eigenvalue gives the frequency while the real part gives the growth rate of the mode. The eigenvector (v) or the spatial variation of the DMD mode is obtained from the eigenvector of the companion matrix (C) and the matrix (K). The energy of each DMD mode is the L2–norm of the eigenvector v. The reader is referred to Rowley *et al.*[50] and Schmid[55] for further theoretical and implementation details.

A.3 Validation for two-dimensional flow over a circular cylinder

$Re = u_\infty d/\nu$	St (DNS)	St (DMD)
60	0.1465	0.1467
100	0.1701	0.1697
200	0.1856	0.1856

Table A.1: Validation of DMD for a 2D cylinder. The St from DNS is obtained from the lift spectra.

We perform dynamic mode decomposition (DMD) for two–dimensional cylinder flow at Reynolds numbers ($Re = u_\infty d/\nu$) of 60, 100 and 200 to validate the method. The computational grid has 1 million elements and the upstream, downstream and spanwise extents (on either side of the center plane) are 20, 40 and 50 respectively when scaled with the cylinder diameter (d). The size of each vector (x_i) for the DMD is 1 million x 2 = 2 million. The Strouhal number ($St = fd/u_\infty$) computed from the time history of lift in the DNS is compared to the St obtained from DMD in Table A.1. Note that the agreement is excellent, thus validating the DMD methodology. Also, the values of St obtained are in agreement with past studies Tritton [63]. Here, 50 snapshots were used in the DMD computation with a $\Delta t u_\infty/d = 0.4$. Figure A.1 shows the energy spectra of the DMD modes for the three cases simulated. As expected, the Karman mode is the most energetic. Also shown are vorticity contours of the 1st and 2nd most energetic modes obtained from DMD. The vorticity contours for $Re = 60$ are qualitatively similar

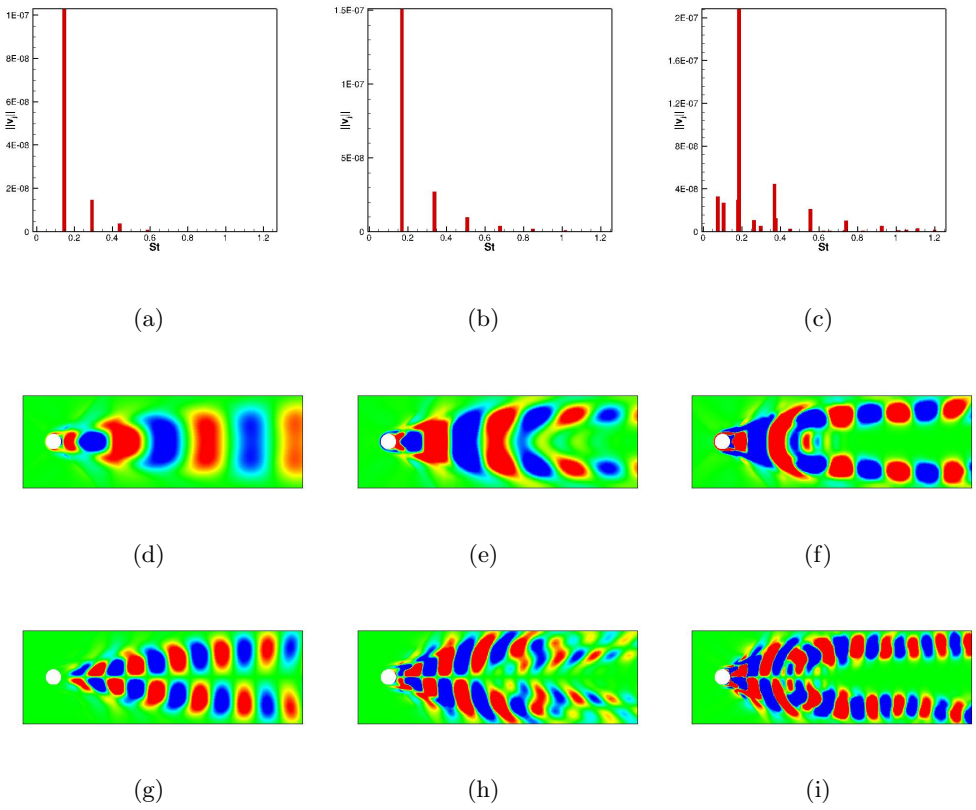

(a) (b) (c)

(d) (e) (f)

(g) (h) (i)

Figure A.1: Spectral energy with Strouhal number obtained from DMD (a, b, c), spatial DMD vorticity contours for the most energetic mode (d, e, f) and the second most energetic mode (g, h, i). The plots correspond to $Re = 60$ (a, d, g), 100 (b, e, h) and 200 (c, f, i) respectively.

to those obtained by Chen, Tu & Rowley[13] at the same Re and the streamfunction contours by Bagheri[6] at $Re = 50$.

A.4 Application of DMD for complex flows

A.4.1 Low-speed jet in a laminar crossflow

Dynamic mode decomposition was performed for the full three–dimensional flowfield for jet to crossflow velocity ratios of $R = 2$ and 4 using all the three velocity components. The flow data was obtained from the DNS of Mussoni, Iyer & Mahesh[42] whose conditions matched the experiments of Megerian *et al.*[35]. The grid contains 80 million points. The snapshots were taken at an interval of $\Delta t v_j/d = 0.333$ units, where v_j and d are the jet exit velocity and diameter respectively. 249 snapshots were used for $R = 2$ while 80 snapshots were used for $R = 4$. For $R = 2$, the residual of the DMD approximation did not vary significantly between 100 , 200 and 249 snapshots. Hence just 80 snapshots were used for $R = 4$. Figure A.2 shows the energy spectra of the DMD modes. Note the prominent peaks at $St = 0.63$ and 1.3 for $R = 2$ and $St = 0.39$ and 0.78 for $R = 4$; they correspond to the same peaks observed along the shear layer from the DNS and experiments. Thus, the shear layer modes are dominant global modes in the flow.

Figure A.2 shows the spatial DMD modes corresponding to the shear layer peaks using iso–contours of Q–criterion coloured with streamwise velocity contours. Coherent three–dimensional shear layer vortices are observed for both $R = 2$ and 4. The spatial modes corresponding to $St = 1.3$ for $R = 2$ and $St = 0.78$ for $R = 4$ display three–dimensional vortices with a smaller length scale suggestive of a sub–harmonic. Note that the scale of the figure is different for $R = 2$ and 4 to clearly depict the spatial mode. It can be seen that the $R = 4$ mode is farther away from the wall which is expected due to the higher momentum of the jet compared to the crossflow. The vortices are coherent until a certain distance downstream, beyond which, smaller scales can be observed indicating the transitional/ turbulent nature of the flow. For the $R = 2$ jet, note that both the $St = 0.63$ and 1.3 modes begin immediately at the flat plate whereas for $R = 4$, while both the modes are located further away from the flat plate, the $St = 0.78$ mode lies closer to the flat plate.

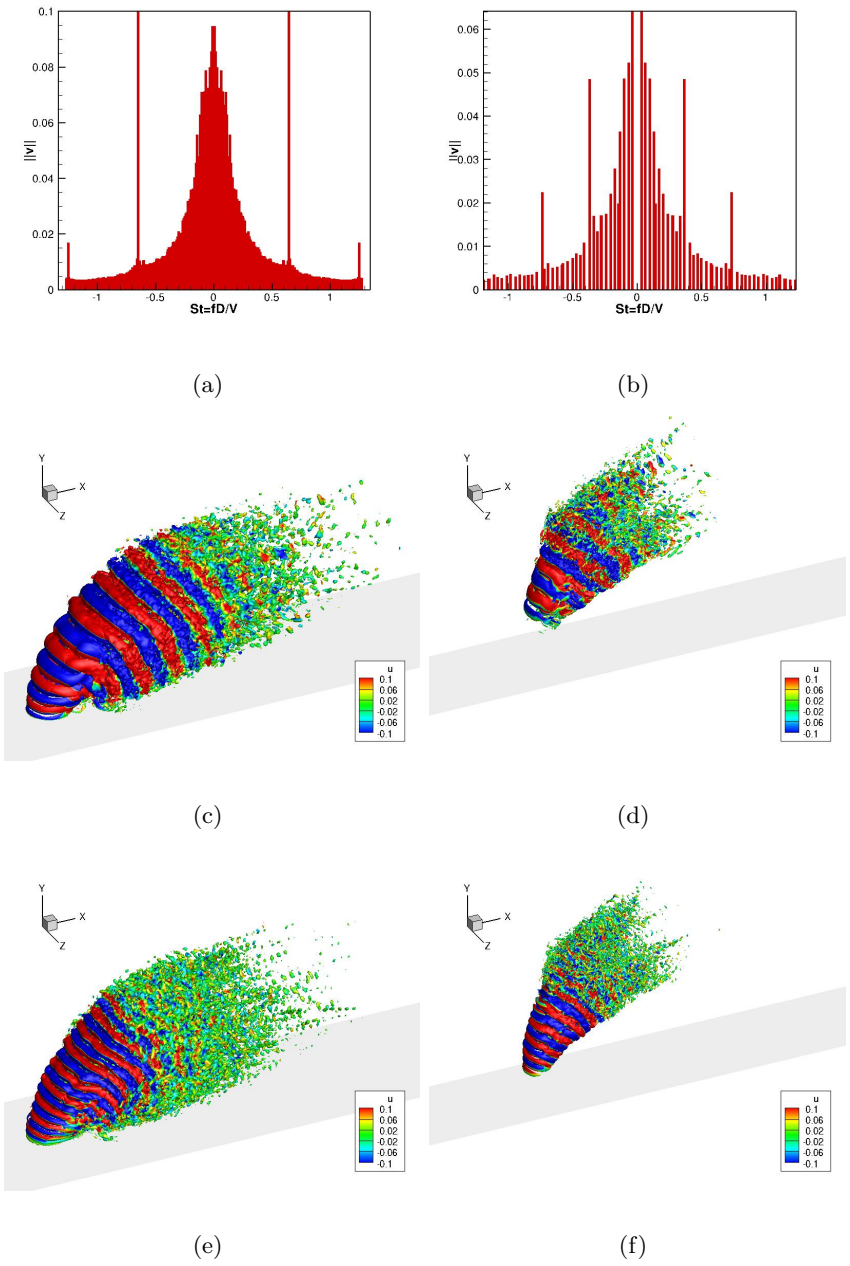

Figure A.2: Spectral energy with Strouhal number obtained from DMD (a, b), iso–contours of Q obtained from DMD for $St = 0.63$ (c), $St = 0.39$ (d), $St = 1.3$ (e) and $St = 0.78$ (f). The plots correspond to $R = 2$ (a, c, e) and $R = 4$ (b, d, f) respectively.

A.4.2 Sonic jet in a supersonic turbulent crossflow

Dynamic Mode Decomposition (DMD) of the full three-dimensional pressure field was performed using 124 snapshots with a temporal spacing of $\Delta t = 0.1\ D/u_\infty$, where D is the jet exit diameter and u_∞ is the crossflow free-stream velocity. The flow data was obtained from the simulations of Chai & Mahesh[11] whose conditions matched the experiments of Santiago & Dutton[52]. The grid contains 75 million points. Figure A.3 (a) shows the variation of energy with St where $St = fD/u_\infty$ is the Strouhal number, and it is observed that $St = 0.3$ mode has the highest energy, thus indicating that the oscillation is global in nature since it is recovered from the DMD of the entire flowfield. This is consistent with the observations of point spectra of pressure from the simulations, where $St = 0.3$ was dominant at various different regions of the flowfield. Iso-contours of pressure of the $St = 0.3$ DMD mode is shown in Figure A.3 (b). Regions of positive and negative pressure is shown. It can be seen that the $St = 0.3$ mode is most dominant is the upstream barrel shock region. To better understand the dominant $St = 0.3$ mode, symmetry plane contours of the pressure field is shown in Figure A.3 (c). The pressure contour shows that the mode extends from the upstream barrel shock region and extends upto the bow shock upstream of the jet. The pressure contour also indicates that it is dominant downstream of the jet where coherent vortices are shed.

Based on the results from the DMD of the pressure field, the velocity field is reconstructed for the $St = 0.3$ mode and the symmetry plane spanwise vorticity contour is plotted in Figure A.3 (d). It can be seen that vortices are shed both upstream and downstream of the jet. The upstream jet shear layer contains vorticity from the jet boundary layer which is shed into discrete vortices due to the unsteady perturbation from the barrel shock. The upstream shedding takes place immediately at the jet exit while the downstream shedding takes place further downstream of the jet. The downstream shear layer of the jet appears to shed at the intersection of the shear layer with the Mach disk. Due to the large scale oscillation of the barrel shock, the Mach disk also oscillates with the same frequency causing the downstream shear layer to shed at the same frequency. This coupling between the oscillation of the shocks with the shear layer shedding makes high-speed jets in crossflow different from low-speed roll up of the shear layer.

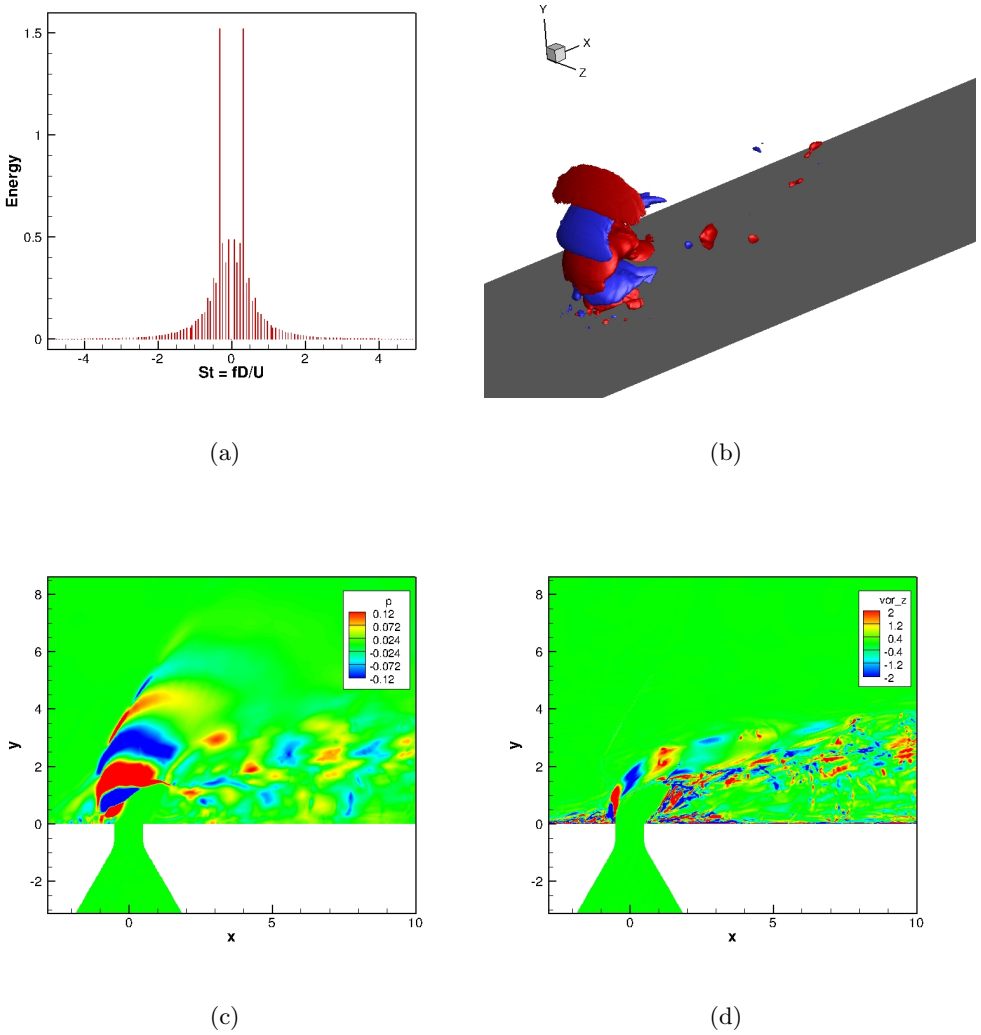

(a) (b)

(c) (d)

Figure A.3: Figure showing results from the Dynamic Mode Decomposition of the pressure field for the sonic jet in supersonic crossflow: (a) Energy variation with Strouhal number ($St = fD/u_\infty$), (b) Iso-contour of pressure of the most dominant mode, (c) and (d) Symmetry plane pressure and spanwise vorticity contour of the most dominant mode.

A.4.3 Supersonic jet in a subsonic turbulent crossflow

Dynamic Mode Decomposition (DMD) of the full three-dimensional pressure field was performed using 150 snapshots with a temporal spacing of $\Delta t = 0.1\ D/u_\infty$. The flow data was obtained from the simulations of Chai & Mahesh[11] whose conditions matched the experiments of Beresh *et al.*[8]. The grid contains 27 million points. Figure A.4 (a) shows the variation of energy with St and it is observed that multiple frequencies are dominant without a single peak as observed for the sonic jet. This is consistent with the observations of point spectra from the simulation where different frequencies were dominant in different regions of the flowfield. Probes placed along the upstream shear layer showed that $St = 1$ mode was dominant. A local peak in the energy in Figure A.4 (a) is also observed at $St = 1$. Iso-contour of pressure of the $St = 1$ DMD mode is shown in Figure A.4 (b). Coherent shear layer roll up is observed similar to a low speed flow. Symmetry plane pressure contours of the $St = 1$ DMD mode is shown in Figure A.4 (c). It can be observed that the pressure unsteadiness occurs in the upstream shear layer and in the wake of the jet. It is interesting to note that the pressure unsteadiness is dominant in the upstream shear layer roll up region and not in the region of shocks indicating that the shocks do not have a significant impact on the shedding for this flow. This is in contrast to the sonic jet flow where the shock-induced unsteadiness affects the shear layer shedding. Spanwise vorticity contours of the $St = 1$ mode in Figure A.4 (d) show that it is dominant in the upstream and downstream shear layers and in the wake of the jet giving rise to trailing vortices.

Figure A.4 (a) showed that multiple frequencies were dominant for this flow. Hence, we also plot $St = 0.43$ mode which has a local peak and higher energy than the $St = 1$ mode. Figure A.4 (e) shows the iso-contour of pressure. This mode appears to be dominant downstream of the jet and further along the jet trajectory when compared to the $St = 1$ mode. Two trains of shear layer vortices are observed. One, due to the roll up of the upstream shear layer and another possibly corresponding to the downstream shear layer. The symmetry plane contours of the $St = 0.43$ mode shows that it is initially dominant in the downstream shear layer and also interacts with the wall vortices. The pressure isocontour in Figure A.4 (f) shows that, closer to the jet, the vortices extend all the way upto the wall.

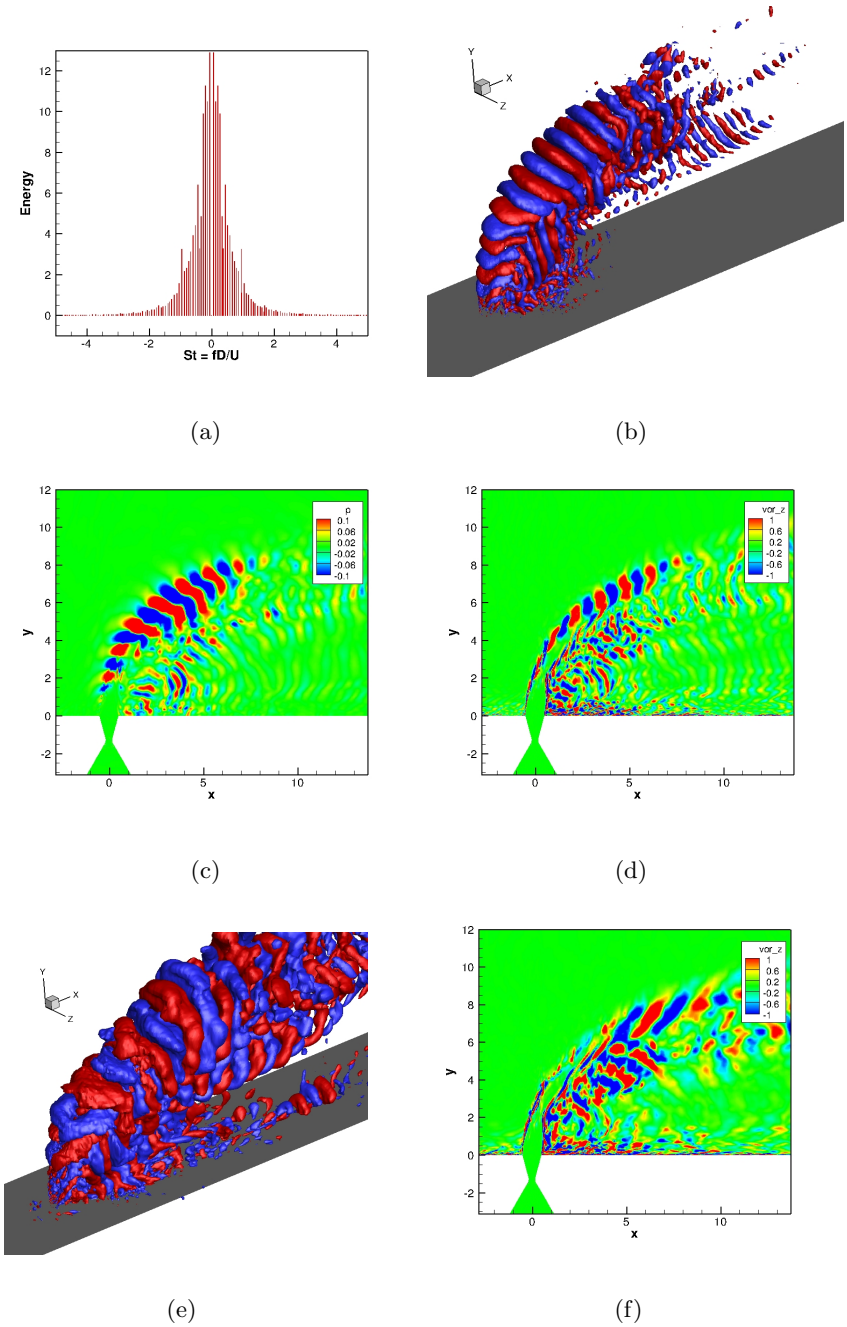

Figure A.4: Figure showing results from the Dynamic Mode Decomposition of the pressure field for the supersonic jet in subsonic crossflow: (a) Energy variation with Strouhal number ($St = fD/u_\infty$), (b) and (e) Iso-contour of pressure of the $St = 1$ and $St = 0.43$ shear layer mode, (c) and (d) Symmetry plane pressure and spanwise vorticity contour of the $St = 1$ shear layer mode. Symmetry plane pressure contours for $St = 0.43$ mode is shown in (f).